An atomic perspective of the photodissociation and geminate recombination of triiodide in condensed phases

The possession of knowledge does not kill
the sense of wonder and mystery.
There is always more mystery.

— Anaïs Nin

Abstract

The thesis presents progress made towards a thorough understanding of the photodissociation and geminate recombination of triiodide anion (I_3^-) in solution and solid state using novel time-resolved spectroscopic and structural methods that have matured in the past decade. An isolated I_3^- has only three degrees of freedom, but in the condensed phase, the case of an open quantum system, its chemistry is transformed because other degrees of freedom from the surroundings (the bath) need to be fully taken into account. This system is a textbook example for understanding dissociation and recombination processes in condensed phases, but unresolved issues about the reaction pathways remain. To probe the issues, firstly, mid-UV pulse shaper-based closed-loop adaptive control as well as open-loop power and chirp control schemes were used in conjunction with single-color pump-probe detection of the yield of the photoproduct diiodide ($I_2^{-\bullet}$) to study the above reaction in ethanol solution. The experiments revealed a strong pump-chirp dependence of the $I_2^{-\bullet}$-yield (as much as 40% change). Subsequently, two possible mechanisms involving additional reaction channels were postulated in order to explain such effect. Secondly, pump-supercontinuum-probe spectroscopy and ultrafast electron diffraction were performed separately on solid state triiodide compound n-$(C_4H_9)_4NI_3$ (TBAT). This system was chosen to provide a well-defined lattice for the bath and to avail atomic resolution of the condensed phase reaction dynamics. In the optical experiment, coherent oscillations were observed within a probe delay of 1 ps that bear strong resemblance to the stretching modes of ground-state I_3^- and $I_2^{-\bullet}$ fragment, which makes it the first to reliably distinguish the two species in a single measurement. In addi-

Abstract

tion, the spectroscopic signature of a novel intermediate, the tetraiodide anion ($I_4^{-\bullet}$), was identified and its origin is attributed to intermolecular interaction of the iodine radical ($I^{\bullet}$) fragment and a neighboring I_3^- chain. Moreover, a number of phonon modes of as low as $\sim 10\ \mathrm{cm}^{-1}$ were extracted from the time series data of both optical and electron diffraction experiments using advanced frequency analysis (short-time Fourier transform and continuous wavelet transform) and deconvolution schemes, some with good agreement in frequency, which helped pin down the reaction-coupled modes. In the optical experiment, it was found that the libration modes exhibit a delayed appearance in comparison to the stretching modes, and their frequencies show measureable temperature dependence. These findings reveal the molecular details of the sizeable impact of the photo-induced reaction on the crystal lattice and bring insights to dissociative reactions in organic molecular solids, which have rarely been studied due mainly to their incomplete reversibility. The results can, therefore, serve as the experimental basis for further theoretical developments in the lattice effects on a chemical reaction (promotion, quenching and alteration). Together, these two case studies demonstrate the potential of a comparative and multimodal approach to exploring the broad parameter space (chirp, fluence, polarization, temperature, physical state, etc.) that affects the course of a reaction. Future studies are conceived to examine the dynamical details using shorter optical pulses in targeted spectral regions derived from present experiments, as well as to better resolve the fast molecular modes and confirm the time delay between internal and external modes using shorter and brighter electron bunches.

Zusammenfassung

In dieser Promotionsarbeit werden die Fortschritte präsentiert, die zu einem umfassenderen Verständnis der Photodissoziation und der paarweisen Rekombination (engl. geminate recombination) von Triiodid-Anionen (I_3^-) in Lösung und in Festkörpern führen. Dafür sind neue zeitaufgelöste spektroskopische und strukturelle Methoden zur Anwendung gekommen, die erst im vorherigen Jahrzehnt ausgereift sind. Ein isoliertes I_3^--Anion hat nur drei Freiheitsgrade, aber in den kondensierten Phasen, stellt es ein offenes Quantensystem dar, und sein Chemie ist verändert, weil die weitere Freiheitsgrade der Umgebung (den Bad) vollständig in Betracht gezogen werden müssen. Dieses Reaktionssystem ist ein Lehrbuchbeispiel für Dissoziations- und Rekombinationsprozesse in kondensierten Phasen. Dennoch bleiben ungelöste Fragen bezüglich der Reaktionspfade bestehen. Um diese Fragen zu untersuchen wurden, erstens, Mid-UV Pulsformer basierte closed-loop-adaptive Kontrollsysteme sowie open-loop Leistungs- und Chirp-Kontrollsysteme verwendet, in Verbindung mit monochromatischer Anregungs-Abfrage-Detektion der Ausbeute der Photoprodukt Diiodid-Anion ($I_2^{-\bullet}$) in Ethanol. Diese Experimente demonstrieren eine starke Abhängigkeit der $I_2^{-\bullet}$-Ausbeute vom Chirp des Anregungspulses (bis zu einer Veränderung von 40 %). Folgend werden zwei mögliche Reaktionsmechanismen, mit zusätzlichen Reaktionspfaden, postuliert, um die beobachteten Effekte zu erklären. Zweitens, Pump-Superkontinuum-Probe-Spektroskopie und ultraschnelle Elektronenbeugung wurde an der festen Triiodid-Verbindung n-$(C_4H_9)_4NI_3$ (TBAT) durchgeführt. Dieses System wurde ausgewählt da es ein exakt definiertes Kristallgitter für das Bad bereitstellt, wodurch Reaktionsdynamiken kondensierter Phasen mit

Zusammenfassung

atomarer Auflösung studiert werden können. Bei den optischen Untersuchungen konnten kohärente Schwingungen innerhalb von 1 ps nach der Photoanregung beobachtet werden, welche starke Ähnlichkeiten zwischen den Streckschwingungen der I_3^--Anionen und der $I_2^{-\bullet}$-Fragmenten in ihren Grundzuständen aufweisen. Dies demonstriert, erstmalig die Unterscheidung zweier molekularer Spezies mittels einer einzelnen Messung. Außerdem wurde die spektroskopische Signatur von einem neuen Zwischenprodukt, das Tetraiodid-Anion ($I_4^{-\bullet}$), identifiziert und sein Ursprung wird auf die intermolekulare Wechselwirkung zwischen dem Iod-Radikal ($I^\bullet$) und einer benachbarten I_3^--Kette zurückgeführt. Mithilfe fortgeschrittener Methoden zur Frequenzanalyse (Kurzzeit-Fourier-Transformation und kontinuierliche Wavelet-Transformation) und zur Globalanalyse konnten Phononenmoden bis hinunter zu 10 cm^{-1} in den Zeitreihendaten des optischen und des Elektronenbeugungsexperiments identifiziert werden. In einigen Fällen stimmen die ermittelten Modenfrequenzen gut überein und sind hilfreich bei der Bestimmung der Moden, welche mit der Reaktionskoordinate gekoppelt sind. Die optischen Experimente zeigen ein zeitverzögertes Auftreten der Liberationsschwingungen im Vergleich zu den Streckschwingungen. Weiterhin zeigen die Frequenzen der Liberationsschwingungen eine Temperaturabhängigkeit. Diese Resultate verdeutlichen große molekulare Auswirkungen der photoinduzierten Reaktion auf das Kristallgitter. Sie erlauben einen Einblick in dissoziative Reaktionsprozesse in organischen molekularen Festkörpern, welche kaum studiert wurden, meist wegen ihrer unvollständigen Reversibilität. Die vorgestellten Ergebnisse können als experimentelle Grundlagen für künftige theoretische Entwicklungen zu "Gitter-Effekten" bei chemischen Reaktionen (z.B. Förderung, Quenching und Veränderung von Reaktionspfaden) dienen. Die beiden Fallstudien verdeutlichen das Potential vergleichender und multimodaler Ansätze um den weiten Parameterraum (z.B. der Chirp, die Fluenz, die Polarisation, die Temperatur, der physikalische Zustand, usw.) zu erforschen, der den Verlauf einer Reaktion beeinflusst. Künftige Studien könnten mit kürzeren optische Pulsen in spezifischen Spektralregionen, sowie mit kürzeren und helleren Elektronenpulsen als Probe durchgeführt werden, um die schnellen

molekularen Moden höher aufzulösen und die Zeitverzögerung zwischen internen und externen Moden weiter zu bestätigen.

Contents

Contents

Contents

Acknowledgements

I'm very grateful of the following people, without whose support and influence the project will not progress swiftly and fruitfully to this day:

I thank **Professor Dwayne Miller** for investing great responsibility in me with such a wonderful yet challenging project, for his immense optimism towards challenges that is contagious to others, and for his timely guidance along the way. I thank **Valentyn Prokhorenko** for his boundless support on various things from sample preparation to optics, from instrumentation to data analysis. His advice on how to save budget and improve eyesight will be long remembered by me. I thank **Professor Leonid Brown** for referring me to Professor Miller when I was seeking a new direction as a wide-eyed young man. He made all of these happen. I thank **Professor Peter Vöhringer** and **Professor Keith Nelson** for helpful discussions on some of the results that were presented at the FEMTO12 conference in Hamburg.

I'm very thankful of **Gastón Corthey** for his invaluable support on instrumentation and programming in the ultrafast electron diffraction and solid state optical pump-probe experiments. Life-saving information can be as short as a few lines of text message we exchanged. His advocation of and insistence on using open-source software and hardware has a lasting influence on me. I thank **Stuart Hayes**, who, along with others, designed and built the electron diffractometer and oversaw the course of the electron diffraction experiment on TBAT and gave crucial advise on sample

2

List of acronyms

AFC   adaptive feedback control

AOM   acousto-optic modulator

AWG   arbitrary waveform generator

CASSCF   complete active space self-consistent field

CTFT   continuous-time Fourier transform

(C)WT   (continuous) wavelet transform

dA   differential absorption (= transient absorption in this thesis)

DAQ   data acquisition

DAS   decay associated spectra

DFT   density functional theory

DSF   differential structure factor

ESA   excited state absorption

FROG   frequency-resolved optical gating

GSB   ground state bleaching

GUI   graphic user interface

HWP   half-wave plate

ISRS   impulsive stimulated Raman scattering

LOESS   local regression

MSPP   minimum-signal pump polarization

4

NOPA	noncollinear optical parametric amplifier
(P)DOS	(partial) density of states
PES	potential energy surface
SE	stimulated emission
S/THG	second/third-harmonic generation
SOI	spin-orbit interaction
STFT	short-time Fourier transform
TA(S)	transient absorption (spectroscopy)
TBAT	tetra-n-butylammonium triiodide
TFR	time-frequency representation
TL	transform-limited
UED	ultrafast electron diffraction
UHV	ultrahigh vacuum

1 Introduction

In this chapter, first, the concept of geminate recombination is introduced, followed by a brief history of the photochemical studies of triiodide in the fs-ps time scale. Then an overview of the concepts, relevant historical developments and theories of the three methodologies applied to investigate the condensed phase triiodie reaction is provided. The chapter concludes with a summary of motivations for the present study.

1.1 Geminate recombination of the triiodide anion

The concept of geminate recombination following photodissociation was proposed [1, 2] and established through comparing experimental recombination rates in gas phase Br_2 [3] and solvated I_2 [4]. The major observation was that recombination happens faster in solution than the gas phase due to frequent collisions between fragments and solvent molecules. Fundamentally, geminate recombination is a finite-environment effect [5–7] and can be achieved after as few as a single collision event between the freshly formed fragments (geminate pair) and the surrounding molecules [5]. The kinetics comprise two parts: the formation of the geminate pairs, a unimolecular dissociation reaction; the recombination of the these pairs, a bimolecular reaction. It has been observed in clusters in gas phase [8], solvent cages in solution [9, 10], interstitial or lattice sites in glassy [11] or ordered solid [12]. Even though diffusion-limited bimolecular reactions in general proceed on a ns-μs timescale, the geminate pairs formed in a confined environment are able to bypass the diffusion limit and

6

recombine on their ground state potential energy surface (PES) on the fs-ps time scale [5].

Originally, I_2 was the model system of geminate recombination, but its fast predissociation dynamics in the excited state has made it hard to discern the true geminate recombination happening on a similar few-hundred femtosecond time scale [5]. An ideal candidate would have a purely dissociative excited state. The triiodide ion (I_3^-) is a potentially perfect candidate in this respect. As a closed-shell stable polyiodide commonly seen in iodine chemistry [13, 14], I_3^- possesses two dissociative excited states accessible via photoexcitation from the ground state X ($^1\Sigma_g^+$) to either its C ($^3\Pi_u$) or D ($^1\Sigma_u$) band[1] (see Fig. 2.1b). The repulsive nature of the excited-state PESs result in completion of the dissociation within very few vibration periods. Depending on the number of distinct fragments, the dissociation process can be broadly categorized into two- and three-body reaction channels as listed below[2],

$$I_3^- \xrightarrow{h\nu} I_2 + I^- \quad \text{(two-body dissociation)} \tag{1.1}$$

$$I_3^- \xrightarrow{h\nu} I_2^{-\bullet} + I^\bullet \quad \text{(two-body dissociation)} \tag{1.2}$$

$$I_3^- \xrightarrow{h\nu} I^- + 2I^\bullet \quad \text{(three-body dissociation)} \tag{1.3}$$
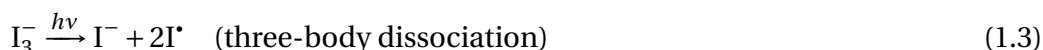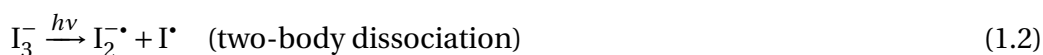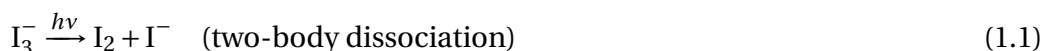
In condensed phases, these photofragments recombine geminately or non-geminately to reform the mother ion at different rates. In this thesis, the photodissociation and recombination of I_3^- is referred to simply as the *triiodide reaction*, if not discussed

---

[1]The excited state assignments of I_3^- have been a point of contention till the 2000s as have been discussed in most of the previously published papers. This all comes from the failure of proper treatment of the strong spin-orbit interaction (SOI) of the iodine atom and the limited basis sets that are computationally manageable. This thesis adopts the notation used in the most recent theoretical exposition of the electronic structure of I_3^- [15]. The assignment was obtained from a relativistic calculation taking full account of the SOI, which endowed both the C and the D bands, now both labelled 0_u^+, with highly mixed singlet-triplet characters, the C band being more singlet-like and the D band more triplet-like. The major difference of this assignment from earlier work is in the C band, which was attributed to another singlet state (see [16]).

[2]Further distinction of the dissociation channels to include the details of the spin states of the fragments is not of immediate interest to condensed phase studies presented in this thesis, therefore their elaboration is omitted here. Details on these can be found in gas phase studies such as [17] or [18].

separately.

Femtosecond studies on I_3^- began in 1992, when a discovery from the Ruhman group [19] revealed that in ethanol (EtOH) solution, photolysis of I_3^- produced vibrationally hot and coherent ground-state $I_2^{-\bullet}$ via reaction channel 1.2. The 115 cm^{-1} oscillations[3] modulate the fast-rising absorption band of $I_2^{-\bullet}$ appearing only a few hundred femtoseconds after time zero. Since then a flurry of studies were conducted on the system in all three phases. In gas phase studies, Neumark's group [20, 21, 17] and Nagata's group [22, 18] distinguished and characterized the complex dissociation pathways of I_3^- using state-of-the-art femtosecond photoelectron spectroscopy and coincidence detection techniques. In the well-studied solution phase, the most exciting discovery since 1992 was the solvent-dependent symmetry breaking [24] of the linear I_3^- geometry inferred from static stimulated Raman measurements [23]. The effort was soon extended to the solid state, where similar vibrational beats and lattice-dependent dephasing and recovery rates were captured by single-shot spectroscopy [25, 26]. The results on previous solution phase and solid state dynamics will be discussed in more detail separately in Chapters 2 and 3. On the theory side, I_3^- has become a benchmark for testing relativistic quantum chemical methods [15] that take full account of the spin-orbit interaction (SOI), which is typical in iodine systems. The calculations showed, among other things, a conical intersection as close as ~ 0.7 Å away from the equilibrium position along the symmetric stretching coordinate of I_3^-, accessible via the C-band transition (see Fig. 2.1b). These studies made I_3^- front and center in the discussion of the distinguishing features between the gas and condensed phases chemical reactions [27]. Nevertheless, a complete story of the triiodide reaction in condensed phases is still missing important information, such as the branching ratio and the recombination pathways, to name just two. The former has only been indirectly measured in solution [16] because the unique photoproduct

---

[3]This number was soon revised down in later publications of the Ruhman group and the reported frequency of the $I_2^{-\bullet}$ stretching mode ranges from 93-115 cm^{-1} in solution phase studies.

from the three-body dissociation channel 1.3, namely I^-, hasn't been directly captured due to its high-energy absorption bands at > 4.77 eV (< 260 nm) [28]. The latter is due to the lack of detailed knowledge of the intercrossing low-lying PESs of I_3^- upon which the recombination reaction proceeds (compare the much better characterized I_2 [29]). New methodologies beyond pump-probe spectroscopy are needed to bring these issues into focus. Indeed, very recently, Ihee's group distinguished the two- and three-body pathways in solution using time-resolved X-ray liquidography aided by molecular structure simulations. They inferred the branching ratio from fitting the species-specific ring diffraction patterns to the experimental data [30, 31]. But the synchrotron source they used (~ 100 ps X-ray pulses) cannot provide sufficient time resolution to access dynamics in the beginning of the reaction. Moran's group used different types of four- and six-wave mixing spectroscopies in the mid-UV to study the dynamical correlation between the stretching modes of I_3^- and $I_2^{-\bullet}$ [32, 33]. It's only a matter of time before more methodologies are applied to re-examine the I_3^- system.

1.2 Multimodal studies of a chemical reaction

The study of chemical kinetics has always been a technique-driven field of research [34, 35]. Even fully understanding a simple chemical reaction in the gas phase[4], where ideally the system-bath interaction can be vanishingly weak, requires a wealth of knowledge about the valence electrons and the nuclei. A non-exhaustive list includes the position, energy, momentum (or the rovibronic state) of the nuclei and the spatial and spin wavefunction of the valence electrons. In the condensed phases, the problem becomes even harder due to the strong influence of the bath (solvent shell or crystal lattice), which alters the PESs and modifies branching ratios, thereby shaping the reaction kinetics. It is next to impossible to find a technique that is capable of recording all relevant parameters of the participants of a reaction, but a combination of methodologies commands a panoramic view of the correlations between structure

---

[4]Here it is also assumed that no external electromagnetic field besides the vacuum field is present.

and dynamics. From a physical point of view, each technique has varying sensitivity to different aspects of the dynamics, so a multimodal approach should be the norm. In the following, I will introduce the basics of the three techniques used in my study of the triiodide reaction in solution and solid state.

1.2.1   Transient absorption spectroscopy

Transient absorption spectroscopy (TAS) is an extension of flash photolysis using ultrafast lasers, in which an intense "pump" pulse is used to excite the sample under study and an usually weaker "probe" pulse is used to interrogate the system at varying time delays with respect to the time zero set by the pump pulse. Here, "ultrafast" refers to laser pulse duration shorter than the primary processes of interest. This timescale is typically on the order of tens to hundreds of femtoseconds. The time resolution of observation is determined by the convolution of the excitation pulse triggering the event and the probe pulse observing the following sequence of events. Typically the pump and the probe pulses are derived from the same laser to eliminate the timing jitter as well as reducing the effects of the slow drift caused by beam pointing instability. The groundbreaking discovery of supercontinuum generation (SCG) in 1970 [36] and its subsequent developments [37] have made it possible to monitor dynamics with a very broad probe spectrum [38]. On the detector side, multichannel detection using low-noise, fast CCDs, which only came about less than a decade ago, greatly improved the speed and sensitivity of TAS. It is now possible to record the entire dispersed probe spectrum in a spectrometer running at the standard repetition rate of a commercial Ti:Sapphire ultrafast laser at 1 kHz.

Formally, a semiclassical model can be applied to understand the signal detected in a two-beam pump-probe experiment. In the model, the two E fields are treated classically, taking the form,

$$E(\mathbf{r}, t) = E_1(t)e^{-i\mathbf{k_1}\cdot\mathbf{r}} + E_2(t - t_{pp})e^{-i\mathbf{k_2}\cdot\mathbf{r}} + c.c., \tag{1.4}$$

where the subscripts 1 and 2 denote quantities associated with the pump and the probe fields, respectively. The symbols $E_1(t)$ and $E_2(t - t_{pp})$ are the temporal envelopes (i.e. Gaussian) of the two fields. The pump-probe time delay t_{pp} can vary arbitrarily.

On the other hand, the system is treated quantum mechanically. The pump pulse traveling along direction $\mathbf{k_1}$ creates a nonequilibrium population, which interacts with the probe pulse traveling along $\mathbf{k_2}$ ($\mathbf{k_2} \neq \mathbf{k_1}$) to be converted into coherences, and they decay through emission in the same direction as the probe. Therefore, the differential absorption, dA, of the probe with and without the pump pulses carries the information about the relative change of the system under study. Detection in such geometry is termed self-heterodyning. The lowest nonlinear interaction order for pump-probe signal generation in isotropic medium is three, that is, two interactions with the pump field (at times t_1 and t_2) and one with the probe field (at time t_3). This casts TAS into the framework of four-wave mixing spectroscopy (FWMS). Macroscopically, the coherences generated after the three-field interaction is directly related to the third-order nonlinear polarization, $P^{(3)}$, of the medium. In the low excitation limit, $P^{(3)}$ is linked to the spectrally-resolved differential absorption, $dA(\omega_2, t_{pp})$, by the relation [39],

$$dA(\omega_2, t_{pp}) = -2\omega_2 \frac{Im[E_2^*(\omega_2)P^{(3)}(\omega_2, t_{pp})]}{|E_2(\omega_2)|^2} \tag{1.5}$$

where $P^{(3)}(\omega_2, t_{pp})$ is the spectrally-resolved $P^{(3)}$ at the pump-probe time delay t_{pp}. Note that ω_2 is the spectrally-dispersed frequency from the corresponding wavevector $\mathbf{k_2}$. The term $P^{(3)}(\omega_2, t_{pp})$ is linked to its k-space representation by a Fourier transform.

$$P^{(3)}(\omega_2, t_{pp}) = \int_{-\infty}^{\infty} P^{(3)}(\mathbf{k_2}, t, t_{pp})e^{-i\omega_2 t}dt \tag{1.6}$$

where $\omega_2 = ck_2$. In this case, $P^{(3)}(\mathbf{k_2}, t, t_{pp})$ can be obtained from perturbation theory,

$$P^{(3)}(\mathbf{k_2}, t, t_{pp}) = \int_0^\infty dt_3 \int_0^\infty dt_2 \int_0^\infty dt_1 R^{(3)}(t_3, t_2, t_1) E_l(\mathbf{r}, t - t_3 - t_2 - t_1, t_{pp}) \cdot$$

$$E_m(\mathbf{r}, t - t_3 - t_2, t_{pp}) E_n(\mathbf{r}, t - t3, t_{pp}) \quad (1.7)$$

where $R^{(3)}(t_3, t_2, t_1)$ is the nonlinear response function with t_1, t_2 and t_3 being the time of interaction mentioned earlier. The three interacting E fields ($E_l E_m E_n$, $l, m, n = 1$ or 2) take on specific meaning of the pump or the probe fields when their temporal ordering is specified. In the regime where the pump and probe overlap temporally, $P^{(3)}$ has contribution from coherent artifacts [40], as a result of the "probe-pump-pump" ($E_2 E_1 E_1$) and "pump-probe-pump" ($E_1 E_2 E_1$) interactions. The genuine pump-probe signal comes from the "pump-pump-probe" ($E_1 E_1 E_2$) interaction, which dominates when the pump precedes the probe pulse. In this formalism, the detected signal lies in the probe direction, $\mathbf{k_2}$, as a consequence of momentum conservation[5].

When only electronic levels are considered, in a two-level molecular system (using the Dirac notations $|0\rangle$ and $|1\rangle$ to label the electronic states), $P^{(3)}$ has contribution from ground state bleaching (GSB) and stimulated emission (SE). In a three-level system (with $|2\rangle$ as the third level), excited state absorption (ESA) may often not be ignored. These processes are illustrated using the double-sided Feynman diagrams shown in Fig. 1.1. Additionally, when vibrational or rotational degrees of freedom are considered and the pulse is shorter than a vibration/rotation period, impulsive stimulated Raman scattering (ISRS) or its resonant version (RISRS) can contribute to the signal in the ground state absorption band of the reactant as well. This process involves a phonon as well as a two-field interaction with the pump pulse [42]. In general, these components of the pump-probe signal are present in the dA spectrum in addition to any existing spectral overlap between the reactant and the photoproduct(s) from

---

[5]Here $\mathbf{k_2} = -\mathbf{k_1} + \mathbf{k_1} + \mathbf{k_2}$, with the right-hand side coming from the momentum conservation of the three-field interaction. The $\mathbf{k}$ vectors of the E fields involved are labeled in Fig. 1.1.
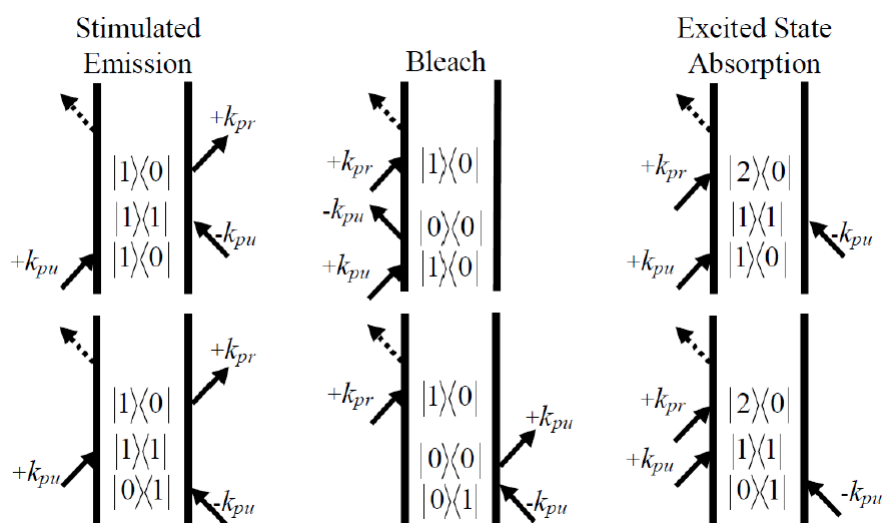
Figure 1.1: Double-sided Feynman diagrams describing the three processes contributing to the signal in the sequential "pump-pump-probe" time ordering. Here $\mathbf{k_{pu} = k_1}$, $\mathbf{k_{pr} = k_2}$, and in every case the system starts from the initial state of the outer product $|0\rangle\langle0|$. The figure is adapted from [41].

static absorption. This means that in general a temporal and a spectral deconvolution scheme (known respectively as global analysis and target analysis [43]) are required to help interpret the dA spectrum obtained from TAS. However, in some cases, sensible conclusions can be drawn from immediate inspection of the spectral regions related to the different species involved in the reaction.

In Chapter 2, TAS in solution phase with single-color pump pulses of various chirp parameters and single-color probe pulses are presented as a detection scheme to gauge the effect of coherent phase control on the production of the $I_2^{-\bullet}$ photofragments. In Chapter 3, results from TAS in the solid state with single-color pump and supercontinuum probe offer a means to interpret similar dynamical changes from ultrafast electron diffraction experiments.

1.2.2 Coherent control

Coherent control exploits quantum interference to guide molecular species along desired reaction pathways using light pulses as a photonic reagent. Big strides have

been made in both theory and experiments in this direction in the past more than two decades [44, 45]. The expected outcome of this line of research is the improvement on the amount of the desired photoproducts or reduction of the unwanted ones. In isolated simple molecular systems (i.e. gas phase diatomic molecules or simple trimers) for which the molecular PESs can be known with excellent precision, a physical approach can be devised and employed [46]. In systems even slightly more complex, an adaptive feedback control (AFC) approach [47–49] is preferred for seeking an effective pulse shape (optimal or anti-optimal). This scheme takes the form in which the chemical system under control is embedded in a closed learning loop that is characterized by the following three key elements:

(1) **Control objective**: For the purpose of encouraging a certain reaction pathway and discouraging the competing ones, the control objective can be determined by, e.g. maximizing the production of certain chemical species unique to the desired pathway, using the difference between or the ratio of the desired product and the undesired ones. Alternatively, a minimization process of the reverse objective(s) can also be chosen.

(2) **Control mechanism**: The control mechanism effects changes on a single parameter or multiple parameters of the optical pulses [50, 51]. Various parameters can function as control paramters, e.g. excitation wavelength and intensity, pump-dump time delay, and the different amount and order of the chirp in the pulse [52]. For phase and amplitude control, the most advanced realization is a pulse shaper. Within the intrument precision and response range, it is able to imprint arbitrary chirp, pulse shape and polarization onto the excitation or probe pulses [53, 54].

(3) **Detection method**: The detection method is chosen depending on the control objective to best represent the effects of control. For example, in a dissociation reaction, the method can be photoelectron imaging [55] or spectroscopic detection of the photofragments [56].
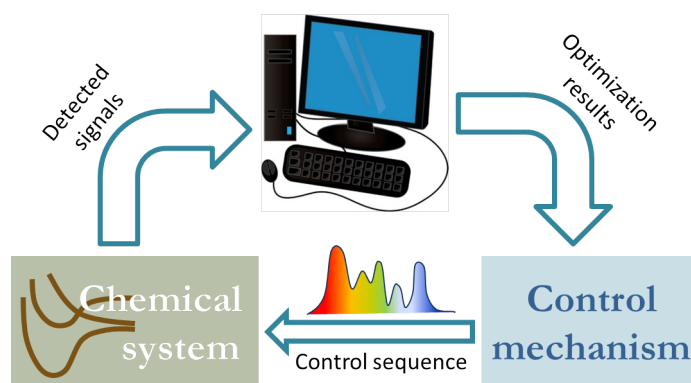
Figure 1.2: A typical adaptive feedback control loop starts with the generation of an initial control sequence (i.e. shaped pulse) by a control mechanism (i.e. pulse shaper), which is sent into the chemical system to initiate a reaction. The detection method attuned to the photoproduct then registers a signal via interaction with the chemical system. The signal is picked up and analyzed by the computer using an optimization scheme. The computer then sends the results to the control mechanism to initiate a new round of optimization.

These three components of an AFC loop are on display in Fig. 1.2. Despite the efficiency of such a black-box-type approach, the underlying physical mechanism from the complex pulse shapes obtained can often be nontrivial to decipher, if not interpreted mistakenly. This motivates the use of single-parameter, open-loop control in addition to closed-loop control, to shed light on the underlying physical mechanism. In Chapter 2, the triiodide reaction in solution phase is investigated using such a combined control scheme.

1.2.3 Ultrafast transmission electron diffraction

Transmission electron diffraction with up to 60 keV electrons (Thomson-Reid experiment [57]) was demonstrated at around the same time as electron diffraction in the reflection geometry (Davisson-Germer experiment [58, 59]) in 1927-28. It was soon applied to the determination of crystal structures [60, 61] and has since proven more successful than the technical spin-off of the Davisson-Germer experiment—LEED[6]. This is because the high electron energy and the transmission geometry make the

---

[6]LEED stands for low energy electron diffraction.

results convenient to interpret based on the kinematic scattering theory in which the sample is well-approximated as a weak phase object [62, 63]. The structure factor $F(hkl)$ is directly related to atomic coordinates within the unit cell and scaled by the atomic form factor f_a and the Debye-Waller factor B [64],

$$F(hkl) = \sum_{j}^{n} f_j e^{2\pi i (hx_j + ky_j + lz_j)} \tag{1.8}$$

$$f_j = f_a(2\theta) e^{-B(\frac{sin\theta}{\lambda})^2} \tag{1.9}$$

where for a given Miller index triplet (hkl), the summation runs over all n atoms that reside in the unit cell. The term 2θ, by convention, is the scattering angle, i.e., the angle between the outgoing and the incoming electron beams.

$$I(hkl) \propto |F(hkl)|^2 = \left| \sum_{j}^{n} f_j e^{2\pi i (hx_j + ky_j + lz_j)} \right|^2 \tag{1.10}$$

An ultrafast electron diffraction (UED) experiment in the transmission geometry is conceptually different from TAS only by the probe pulse, which in this case is the short electron bunch generated by photoemission from a photocathode with a short-pulse laser. In the early 1980s, picosecond lasers were combined with static electron diffraction to investigate simple physical transformations such as the melting of amorphous aluminium [65, 66]. With their $\sim$ 20 ps electron pulse limited by the photoemission laser pulse, Williamson & Mourou was able to trace the decrease of the melting onset time delay as a function of rising excitation fluence from $\sim$ 7 to $\sim$ 13 mJ/cm^2, where the resolution limit was reached since the melting happened within the time duration of the electron probe [66]. What followed this early effort was a the string of exciting developments in the two decades afterwards in ultrashort-pulse laser systems, as well as the compact electron gun design, which finally made time-resolved diffraction experiments with sub-picosecond resolution possible. These progresses culminated in the celebrated Siwick-Miller experiment in 2003 [67], when the melting of Al was initiated with 70 mJ/cm^2 excitation pulses and probed with 600 fs-long electron bunches

(accelerated through a mere 30 keV). In this setting, the diminishing of long-range order that defines melting was captured in real time from the time-resolved changes of pair correlation function and radial density function.

Electron diffraction is a superior technique to study thin samples (around 100 nm or less) in condensed phases due to the $\sim 10^6$ times larger scattering cross section of electrons compared with X-ray photons [68]. The past decade has seen intensive efforts directed to studying structural changes that occur during phase transitions in the solid state [69, 70]. Very recently, the whole phase diagram of 1T-TaS$_2$ was mapped out using UED [71] and it has been demonstrated that structural inversion is a feasible route to extracting atomic motions in real space in a complex organic compound with a protein-sized unit cell [72]. Success stories like these hold promise for extending UED to studying chemically relevant condensed phase materials. These systems are usually organic molecular crystals with poor vacuum stability and a low melting point (< 100 °C), and are, in addition, prone to optical damage. The damage results in structural disorder of the single-crystal sample and render stroboscopic measurements impossible. The reversibility challenge is unique to the solid state studies since in gas or solution phase, rapid replenishment of flowing samples makes the effect negligible[7]. To move towards handling labile samples with strictly irreversible reactions, crystallographic chips [73] and streak cameras [74] were developed to enable single-shot experiments. For systems with a slow recovery rate, temperature stabilization and photoreversion [75] had proven to greatly improve the reversibility in certain cases. Only when the reversibility challenge is met and the sample degradation issue taken into account, can the time-resolved dynamics be studied and analyzed appropriately.

In the time domain, chemical reactions take place at the speed of the changes of bond lengths. In solid state, the changes are contained in the Bragg peak intensities

---

[7]But other issues come up for the other two phases. In solution, the effect of solvent heating creates huge spurious background change, which needs to be calibrated by an auxiliary measurement. In gas phase, the signal is mainly limited by the low sample density.

and positions (including the emergence of new peaks). The *intensity change* can happen immediately after photoexcitation due to an impulse response of nuclei from electronic excitation, while the *position change* reflects modification of unit cell parameters (i.e. size and symmetry) due to a series of consecutive and correlated atomic motions, therefore it becomes evident only on > ps time scales [70]. To quantify the change, one calculates the relative change[8] $\eta(hkl, t)$ of Bragg peak (hkl).

$$\eta(hkl, t) = \frac{I_{\text{on}}(hkl, t) - I_{\text{off}}(hkl)}{I_{\text{off}}(hkl)} = \frac{I_{\text{on}}(hkl, t)}{I_{\text{off}}(hkl)} - 1 \propto \frac{|F_{\text{on}}(hkl, t)|^2}{|F_{\text{off}}(hkl)|^2} - 1 \quad (1.11)$$

The subscripts "on" and "off" refer to the status of the optical pump pulse. When the pump is on, some fraction, $\gamma(\Phi)$, of molecules is excited. The excitation fraction is dependent on the pump fluence, Φ, as well as the absorption coefficient of the molecule (assuming fixed). Taking this into account, $F_{\text{on}}(hkl, t)$ can be further expressed as [76],

$$F_{\text{on}}(hkl, t) = \gamma(\Phi) F_{\text{es}}(hkl, t) + \left[1 - \gamma(\Phi)\right] F_{\text{off}}(hkl) \quad (1.12)$$

Here the structure factor of the excited species, $F_{\text{es}}(hkl, t)$, is changing as a function of time. With the definition of the differential structure factor (DSF) $\epsilon(hkl, t) = F_{\text{es}}(hkl, t) - F_{\text{off}}(hkl)$, Eq. 1.12 then becomes,

$$F_{\text{on}}(hkl, t) = \gamma(\Phi)\epsilon(hkl, t) + F_{\text{off}}(hkl) \quad (1.13)$$

Plugging Eq. 1.13 into Eq. 1.11, and assuming the sample under study has an inversion center, such that the structure factors are all real numbers, then $\eta(hkl, t)$ can be re-expressed as,

$$\eta(hkl, t) = \left[\frac{\gamma(\Phi)\epsilon(hkl, t)}{F_{\text{off}}(hkl)}\right]^2 + \frac{2\gamma(\Phi)\epsilon(hkl, t)}{F_{\text{off}}(hkl)} \sim \frac{2\gamma(\Phi)\epsilon(hkl, t)}{F_{\text{off}}(hkl)} \quad (1.14)$$

---

[8]This is also named the *response ratio* in photocrystallography.

The last step is valid when the first term is a small quantity. In this regime, the relative change at a given probe delay, t, is linearly proportional to the excitation fraction, $\gamma(\Phi)$. The DSF is directly linked to atomic displacement from the definition,

$$\epsilon(hkl, t) = \sum_{j}^{n} f_j \cos\left[2\pi i h_a x_j^a(t)\right] - \sum_{j}^{n} f_j \cos\left[2\pi i h_a x_j^a(-\infty)\right] \tag{1.15}$$

where $h_a x_j^a = hx_j + ky_j + lz_j$ using the Einstein notation, and j runs through all atoms in a unit cell. The time-dependent spatial coordinates of atoms $x_i(t)$ after excitation are connected to the static equilibrium positions $x_i(-\infty)$ through the relation $x_i(t) = x_i(-\infty) + dx_i(t)$, with $dx_i(t)$ being the induced motion from chemical reaction or physical processes. The consequences of Eq. 1.11– 1.15 and the types of time-dependent changes are summarized as follows:

(1) In general $\eta(hkl, t)$ is not a linear function of either the coordinates or the excited fraction. The temporal changes of the atomic coordinates are absorbed into the changes of the Bragg peak intensities through the sine or cosine ($e^{i\phi} = \cos\phi + i\sin\phi$) terms.

(2) The Debye-Waller factor can become time-dependent due to the effect of temperature change (i.e. heating from laser excitation). But for experiments on molecular crystals in the low to intermediate excitation regime, due to inefficient and slow thermalization between electrons and the lattice, such effect usually takes place on a longer time scale than the nuclear dynamics of interest.

(3) The shape factor (contained in the proportionality constant between I(hkl, t) and $|F(hkl, t)|^2$) of the crystal only modulates the intensity profile but not the time dependence of the coordinate changes. In cases where the crystal changes shape due to, e.g. lattice distortion, the shape factor can take on a slow time dependence like in (2).

(4) The motion of an atom along a specific principle axis (e.g. $dx_i(t)$ along **a** axis) factors into $\eta(hkl, t)$ through multiplication with the corresponding Miller index

19

(e.g. $h * x_i(t)$). Such contribution is the same for Bragg peaks sharing one index (e.g. (181) and (283)). This can be helpful to interpret the results in crystals with high symmetry and simple composition. For Bragg peaks differing by one index only (e.g. (181) and (281)), their temporal dependence usually has a strong correlation (differing only by the amplitude or the sign of $\eta(hkl, t)$).

The above discussion is related to Chapter 3, I describe a solid state experiment employing UED, in which the time dependence of Bragg peak intensities reflect coherent motion of photoexcited triiodide ions.

1.3 Rationale behind the present study

First and foremost, the study of triatomics provides a model system for understanding the physics governing chemical processes. The fact that a simple system can hold such intriguing complexity beggars imagination with respect to how complex, high-dimensional many-body systems in chemistry and biology work. Despite earlier efforts, the extension of pulse shaping techniques into the true UV region (wavelength shorter than 400 nm) has only been realized recently [77], thanks to the availability of high-efficiency holographic gratings in this spectral range. Broadband and high-conversion-efficiency noncollinear optical parametric amplifier (NOPA) systems have made it possible to generate tunable pulses in the UV region using their frequency-doubled outputs. This obviates the need for systems to be studied to have high absorption in the visible spectral region corresponding to the low harmonics of the laser's fundamnetal wavelength. Combination with a broadband supercontinuum probe has enabled the pump-supercontinuum-probe (PSCP) experiments to access most, if not all the UV-Vis spectral region [78]. On the other hand, the rapid developments in UED and relevant sample handling and delivery techniques in the past decade have made it possible to investigate fragile organic samples without full structural reversibility. It is therefore an exciting time now to put together these technologies to re-examine the classic triiodide reaction and tackle the unresolved issues.

Besides its fundamental significance as a model triatomic reaction, the electrochemical version of the triiodide reaction has been heavily used in the solar cell industry since the invention of the Grätzel cell [79], which featured the I_3^-/I^- redox pair as a mediator of electron transfer via the intermediate $I_2^{-\bullet}$. The light-to-electricity conversion efficiency of this type of dye-sensitized solar cell is now > 11%, but why and how the triiodide part of the reaction contribute to a high efficiency is poorly understood [80, 81]. In addition, one problem related to practical implementation of the Grätzel cell is its propensity for photodegradation in long-term usage, induced by UV radiation. This concerns the degradation of the I_3^- in the redox pair [80]. Therefore, the study of photoreaction pathways of the triiodide reaction is likewise beneficial to the solar cell community.

2 Combining transient absorption spectroscopy with coherent control

Outline: This chapter begins with a critical summary of previous important findings on the triiodide reaction in the solution phase. Then the settings and results of the closed- and open-loop coherent control experiments in ethanol (EtOH) are presented and discussed. The chapter ends with proposed additional reaction pathways to explain the observations.

 Contributions: For this experiment, Dr. Valentyn Prokhorenko designed and constructed the NOPA and Ryan Field designed and constructed the mid-UV pulse shaper before I joined the group. I helped constructing the along with Valentyn and Ryan. I built the liquid delivery system (LDS) from scratch (including selecting and purchasing the peristaltic pump). I and the group technician Santosh Jangam designed the table support for the LDS.

2.1   The triiodide reaction in solution phase

In EtOH solution, the triiodide reaction has been monitored up to ~ 400 ps after photoexcitation using various types of femtosecond pump-probe spectroscopy [82,83]. The predominant dissociation channels yield $I_2^{-\bullet}$ and I^-, along with the iodine radicals (reaction channels 1.2 & 1.3). The I_2-producing channel (Eq. 1.1) is believed to be suppressed[1] despite being energetically allowed. The photofragment $I_2^{-\bullet}$ has a broad absorption band peaked at around 750 nm [84] and another that penetrates into

---

[1]I_2 has very well-characterized PESs in the ground state and low-lying excited states and it has a ground-state vibrational mode of 214 cm^{-1}, which is fairly different from that of I_3^- and $I_2^{-\bullet}$, detected to be in the range 93-115 cm^{-1}. The I_2 mode oscillations haven't been measured in any solution phase study of the triiodide reaction.

22

(a)

(b)
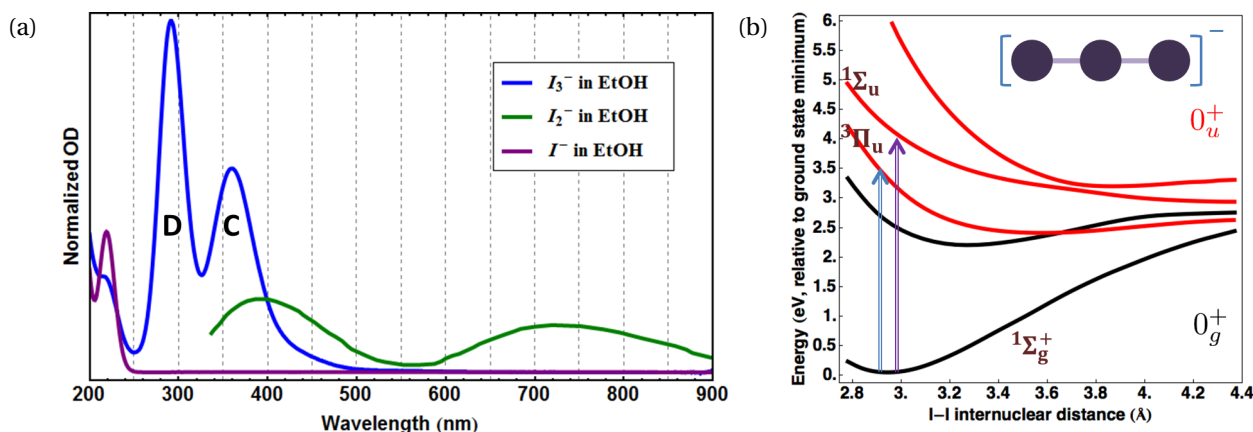
Figure 2.1: (a) Static absorption spectra of I_3^-, I^- and the short-lived $I_2^{-\bullet}$ (adapted from [82]) in EtOH solution. The optical densities are normalized according to Fig.1 of [81]. (b) Theoretical PESs cut along the symmetric stretching coordinate calculated for a symmetric I_3^- in the gas phase (adapted from [15] and redrawn). Both the nonrelativistic (brown) and relativistic (red and black) molecular term symbols are used in (b) for comparison. The PES cuts plotted in red share the same relativistic term symbol and symmetry. The same is true for the black curves. The blue and the purple arrows denote the C and D band transitions of I_3^-, respectively.

the C band of I_3^- (see Fig. 2.1a). The species I_3^- and $I_2^{-\bullet}$ have the same extinction coefficients at 400 nm in EtOH, and I_3^- and $I_2^{-\bullet}$ should maintain a 1:1 stoichiometric ratio according to the reaction, so this wavelength was regarded as the isosbestic point of the dissociation channel involving $I_2^{-\bullet}$ [82]. The observations of solution-phase dynamics on the triiodide reaction (excitation to C or D band) can be summarized into the following points,

(1) The photoproduct $I_2^{-\bullet}$ is formed in its electronic ground state with excess vibrational energy dependent on the photon energy for excitation of I_3^-. Vibrational coherence transfer from I_3^- to $I_2^{-\bullet}$ was invoked to explain the coherent beats observed in the near-IR absorption band of $I_2^{-\bullet}$ [19]. A very recent (late 2015) 2D resonance Raman experiment provided further evidence [33].

(2) Ground state symmetric stretching mode of I_3^- (110-112 cm^{-1}) was determined using degenerate pump-probe measurements and the stretching mode of $I_2^{-\bullet}$ found in separate experiments differ only by a small amount ($\geqslant 10$ cm^{-1}) [25, 85, 86].

23

Ground state antisymmetric stretching mode of I_3^- was determined in ISRS-type experiments [87] to be in the range 140-147 cm^{-1}.

(3) Vibrational dephasing time, τ_{ph}, was measured to be shorter in more polar than non-polar solvents [25, 83, 86]. For example, in [83] τ_{ph} was found to be 1.2 ps, 0.89 ps and 0.53 ps in ethanol, acetonitrile and water, respectively. The differences were attributed to the various degrees of linear symmetry breaking of I_3^- in polar and non-polar solvents.

(4) A low frequency solvent mode was originally detected, though not with superior SNR, in a resonant impulsive stimulated Raman experiment in 1993 (13 cm^{-1} in [88]) and was further verified in a transient grating experiment in 2014 (~ 20 cm^{-1} in [32]). The nature of this mode has been loosely attributed to intermolecular interaction between I_3^- and the solvent molecules [89, 32].

(5) By probing the dynamics at the isosbestic point between I_3^- and $I_2^{-\bullet}$, the $I_2^{-\bullet}$ channel was found to make up 100% and 80% of the dissociation yield via excitation to the C and D bands, respectively [82]. This implied an I^- channel contribution of 0% and 20% in the respective dissociation processes. However, in this once-only study the system response was only measured up to a pump-probe time delay of ~ 34 ps.

(6) Three distinct time scales of the reaction were identified within the first 1 ns after photoexcitation. They correspond to different stages of the recombination reaction. A long-lived excited triiodide ion, $[I_3^-]^*$, and $I_2^- \cdots I$ contact pair, were proposed as potential reaction intermediates to explain the multistaged behavior but definitive spectroscopic deconvolution remained difficult [90].

The use of coherent phase and amplitude control of the photodissociation can influence the reaction's branching ratio, and, therefore, photoproduct formation. By selectively enhancing or discouraging certain pathways, the coherent control scheme can uncover information on participating reaction pathways that are not yet accounted for. The following experiment employs these control schemes for the first time on the

triiodide reaction for such a purpose.

2.2 Coherent control experiment in solution phase

2.2.1 Experimental setup

The detailed layout is shown in Fig. 2.2a. A commercial Ti:sapphire ultrafast laser system (Coherent Elite USP) provided 800 nm, 35 fs FWHM pulses operating at 1 kHz. Its output was split into two parts, one part was directly used as the probe pulse to monitor the broad absorption band of the photoproduct $I_2^{-\bullet}$ around 750 nm. The other part was used to pump a home-built two-stage NOPA with an output at 580 nm. The NOPA fundamental was then compressed using a pair of Brewster-angle prisms, and frequency-doubled. The output 290 nm pulses as well as the undepleted 580 nm fundamental was sent through the grating-based 4f pulse shaper (details in a later section), where the two colors were separated due to their difference in their Bragg diffraction angles. The residual chirp in the 290 nm pulse was compensated using the shaper and set as the baseline chirp (+4700 fs^2). Characterization using a home-built frequency-resolved optical gating (FROG) device [94] obtained a transform-limited (TL) pulse of ~ 60 fs with a FWHM of 3 nm. The pump and probe pulses were focused into a flow cell using the same off-axis parabolic mirror (OAPM, effective focal length = 8") with UV-enhanced aluminium coating. The beam widths (FWHM) of the pump and the probe pulses at the sample position were determined by the knife edge method to be 82 μm and 79 μm, respectively. The trasmitted pump and probe pulses were then collimated using a 2" lens, and detected at every laser shot by two photodiodes (New Focus 2032), whose outputs were registered simultaneously by a National Instruments data acquisition (NI-DAQ) card.

Sample preparation and delivery

The powdered sample tetra-n-butylammonium triiodide, or TBAT (Sigma-Aldrich, CAS No. 13311-45-0), was dissolved in UV-grade ethanol (Uvasol, Merck Millipore) to
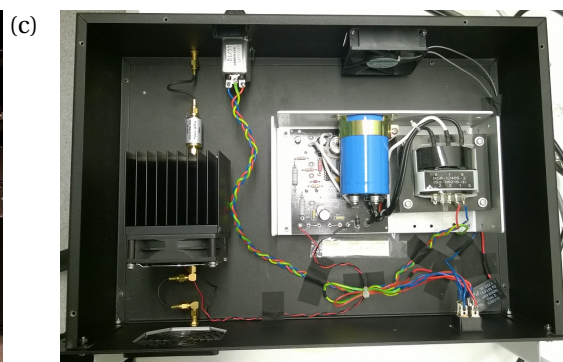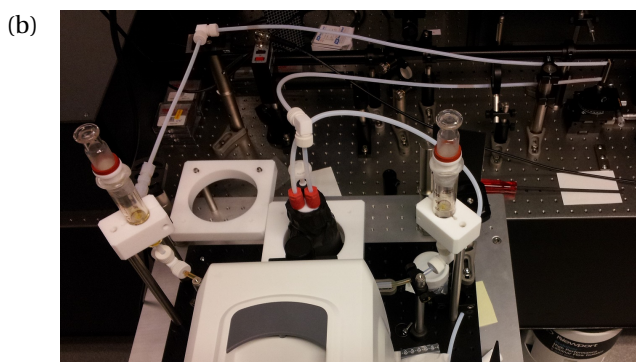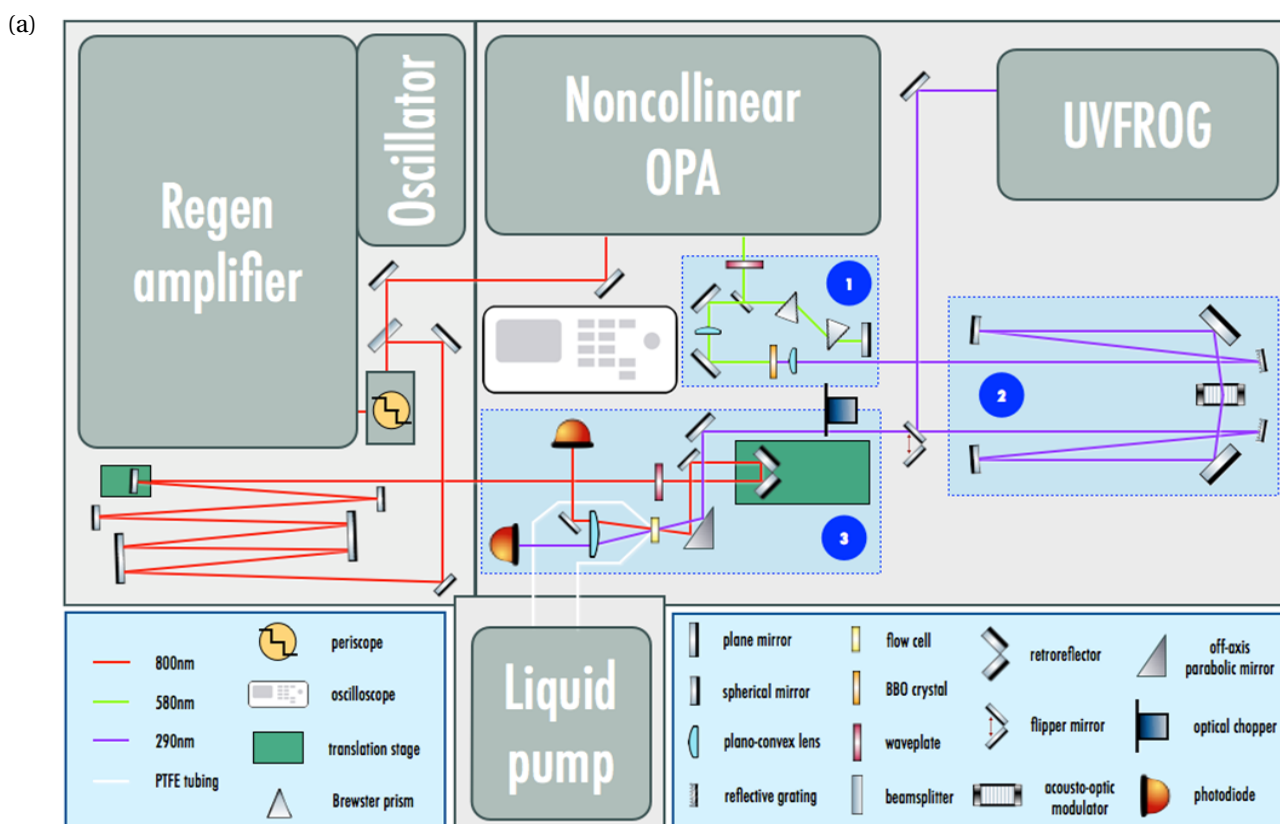
Figure 2.2: (a) Experimental layout of the coherent control experiment. The numbered labels in the graph denote (1) frequency doubling of the NOPA output, (2) 4f pulse shaper in the mid-UV, and (3) pump-probe detection. (b) Home-built liquid delivery system for I_3^- solution with a peristaltic pump and Teflon tubings. (c) Home-built RF amplifier for the waveform generated from the arbitrary waveform generator (AWG) card installed in the measurement computer. The amplified RF output is sent into the acousto-optic modulator (AOM) to generate the acoustic standing wave for optical pulse shaping.

make a solution of 0.25 mM (OD ~ 1 at 290 nm). UV-grade solvent was used to reduce scattering of the optical pump in the experiment. The solution was flowed through a home-built liquid delivery system (see Fig. 2.2b) involving a 100 μm-path-length flow cell with Spectrosil quartz windows (Starna), a sample reservoir, two glass syringe dumpers, and a peristaltic pump with Teflon tubings (Cole-Parmer Masterflex HV-77912-10).

The short-path-length flow cell greatly reduced the solvent signal contribution due to generation of solvated electrons, as compared with 500 μm-path-length cell which had been tested before. The reservoir maintained the sample concentration (OD ~ 1 at 290 nm) during the course of an experiment since the solution phase experiment is only partially reversible [82] or reversible on a μs-ms time scale [91]. This made it possible to run measurements at a pump repetition rate of 500 Hz.

The Teflon-compatible peristaltic pump is essential because I_3^- corrodes most metals and alloys including stainless steel, a common material for pump rotors, and synthetic polymers (e.g. Tygon, Viton, PVC, etc.) used to make flexible tubings, except Teflon (PTFE). The design of a peristaltic pump makes sure that the rotor is only in contact with the tubing but not the solution (as opposed to a gear pump), which keeps any form of corrosion from happening. The drawback of using Teflon tubings is its rigidity compared with other flexible materials mentioned above, therefore the vibration coming from the motion of the pump rotor can affect the stability of the measurements. To solve this issue, a home-built removable trolley was used to support and isolate the peristaltic pump from the optical table, and Sorbothane sheets were used to dampen the vibrations. In actual measurements, the effect of the rotor cycle was undetectable in differential absorption signals.
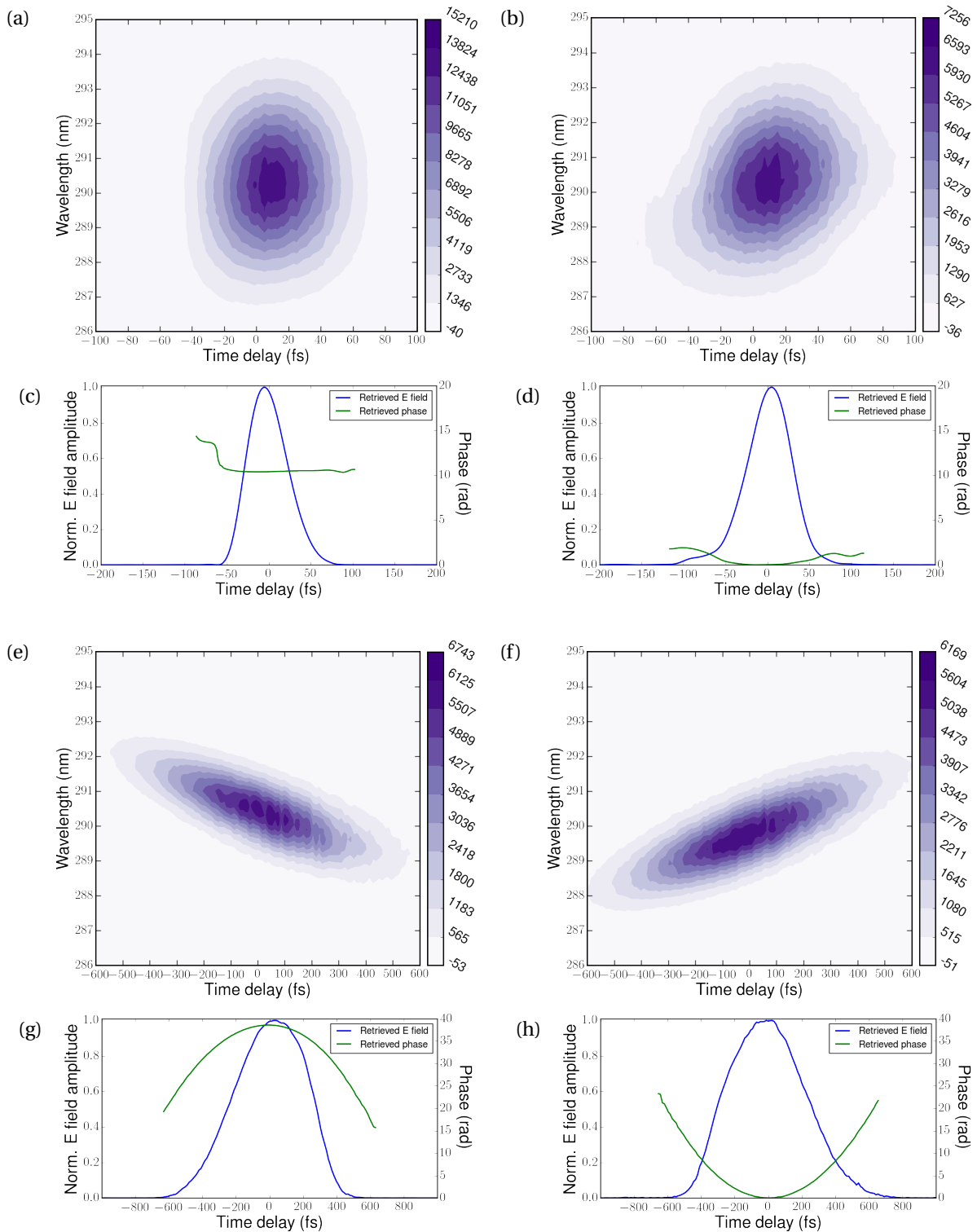
Figure 2.3: FROG traces of (a) 56 fs TL optical pump pulse centered at 290 nm, (b) the 61 fs optimal pulse obtained from optimization using the genetic algorithm, (e) pulse with -10000 fs^2 and (f) +10000 fs^2 second order chirp programmed into the it using the AOM. Their durations are 534 fs and 574 fs, respectively. The pulse duration, E field amplitude and phase are retrieved using the commercial program *Femtosoft FROG 3*. The amplitude and phase profiles are shown in (c), (d), (g) and (h), under the corresponding FROG trace.

Pulse shaping and characterization

The pulse shaper was constructed by Dr. Ryan Field based on an existing design in the 4f-geometry [77] for mid-UV operation shown in Fig. 2.2a. The collimated incoming beam was spectrally dispersed and re-collimated in the Fourier plane of the diffraction grating (Optometrics 3-8248), where the aperture of the acousto-optic modulator (AOM, Brimrose FSD150-50.260) was located. The beam, now elongated in the transversal dimension parallel to the table, passed through the AOM and was diffracted off a transient grating created and controlled by an external AWG PCI card (GaGe ComputerGen 11GX), which was installed on the measurement computer. The outgoing beam followed a symmetric beam path with respect to the input side, therefore exiting the shaper as a collimated beam. Thanks to the high efficiency of the UV reflective gratings, the technical efficiency of the whole shaper was able to reach ~ 50% at around 290 nm.

Pulse characterization was carried out using a home-built transient-grating FROG (TG-FROG) [92, 93]. It was based on an all-reflective diffractive-optic design described in detail in [94]. Example traces obtained from FROG characterization of the optical pump pulses are shown in Fig.2.3.

2.2.2 Coherent control of $I_2^{-\bullet}$ photoproduction

Closed-loop control

Closed-loop control of the photoproduction of $I_2^{-\bullet}$ was performed using a genetic algorithm routine [49] that maximizes the $I_2^{-\bullet}$ yield detected at 800 nm by adjusting the 1D spectral phase (1D vector) using the pulse shaper. The routine worked with a random initial phase and altered the phase profile after each cycle ("genetic mutation and selection"). In this experiment, the pump power was kept constant and convergence of the $I_2^{-\bullet}$ yield was seen after ~40 optimization cycles. The optimization scheme was repeated a few times and very similar phase profiles were obtained. The optimal pulse

was characterized by the TG-FROG and the FROG trace is shown in Fig. 2.3b.

Open-loop control — chirp scan

Since the optimal pulse had a quite similar shape as the TL pulse, an open-loop control experiment was carried out to check for consistency. In this experiment the second-order chirp of the pump pulse was varied from -10000 fs^2 to +10000 fs^2 while detecting the transmitted 800 nm pulse as well as the depleted pump pulse at a fixed time delay of 100 ps ("chirp scan"). On this timescale the TA signal is principally from photogenerated $I_2^{-\bullet}$. The chirp dependence at excitation energies from 100 nJ – 425 nJ was also measured in the same way. At the maximal chirp rate applied (± 10000 fs^2), the pulse was stretched to ~ 550 fs as measured by FROG (see traces shown in Fig. 2.3e and 2.3f). Results from these measurements are presented in Fig. 2.4(a)-(d). The symmetric TA signal dependence on the chirp rate is consistent with the closed-loop optimization result that favored a near-TL pulse shape. The asymmetric chirp dependence (more absorption with a positively chirped pulse) of the pump absorption is in agreement with a previous study on an isomerization model system [95]. The outstanding features in the chirp scan results include the slight shift of the optimal chirp that maximizes the absorption and the "dip" structure near zero chirp, both of which start to develop at lower excitation energy. They deserve further investigation using wavelength-resolved probe.

Open-loop control — power scan

Another important control parameter is the amplitude, or, therefore, the power of the pump pulse. The power dependence of the $I_2^{-\bullet}$ yield can help locate the excitation fluence regime of the measurements. During the experiment, the pump pulses were kept at TL level and the (excitation) energy was varied in the range of 40 – 430 nJ, while monitoring the transmitted pump and the $I_2^{-\bullet}$ absorption at a fixed time delay of 100 ps, the same as the chirp scan for comparison. The results are shown in Fig. 2.4e-f. A nonlinear trend is observed for the excitation energy-transmission dependence
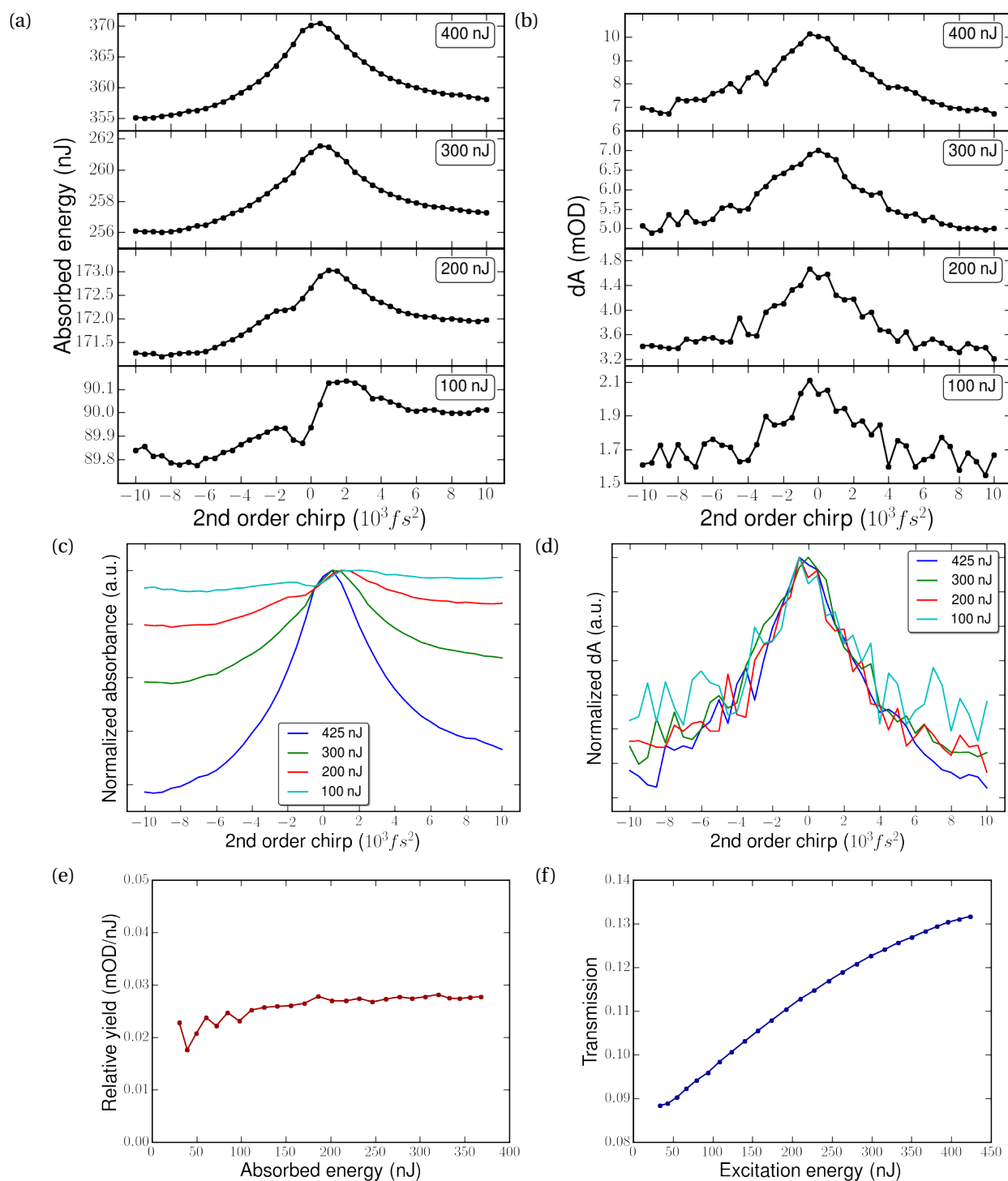
Figure 2.4: Second-order chirp dependence of (a) pump absorption and (b) differential absorption measured at different pump energies (labelled on the upper right corner of each plot). In (c) and (d), each curve from (a) and (b) are normalized to its maximum value. (e) The near-flat dependence of relative yield on the absorbed pump energy. (f) The dependence of transmission on excitation energy.

at high excitation energies ($\geqslant$ 200 nJ). This indicates (1) the involvement of another absorbing mechanism. The other power dependence of importance is that on the relative yield of the reaction, which proves to be a better indicator of the excitation regime than the yield [95]. The relative yield is defined as,

$$\phi_R = \frac{dA}{A} \tag{2.1}$$

In one-photon photochemistry, following the Stark-Einstein law, this quantity is linearly proportional to the quantum yield, which has no fluence dependence. However, in a broad range of excitation energies, the relative yield becomes a function of the excitation fluence, $\phi_R = \phi_R(\Phi)$. A linear fluence dependence of $\phi_R(\Phi)$ signifies the occurrence of two-photon absorption. The results in Fig. 2.4e show a flat dependence throughout most of the scanned power range (at low pulse energies the scattered light can create more measurement uncertainty in the data). This indicates that (2) only one-photon photochemistry is taking place. Combining (1) and (2), it's possible to conclude that an additional pump-absorbing mechanism or species is present in the solution.

2.2.3 Transient absorption spectroscopy with transform-limited and chirped pump pulses

For a better understanding of the results from the coherent control experiments, transient absorption measurements were performed using both TL and chirped pump pulses (see Fig. 2.3a, e-f for FROG traces) at different time delays. In this experiment, the energy of the pump pulses were maintained at 450 nJ regardless of the chirp. The transient absorption traces are presented in Fig. 2.5. At short time delays, the different responses between TL and chirped pump pulses are caused by the difference in the pulse duration as well as the peak intensity. The long pulse duration of the chirped pulses (> symmetric stretching mode period of I_3^-) smooths out the coherent oscillations that are present in the trace measured with TL pump pulses. The reduction in peak intensity also flattens out the sharp spike that is partly due to solvent response
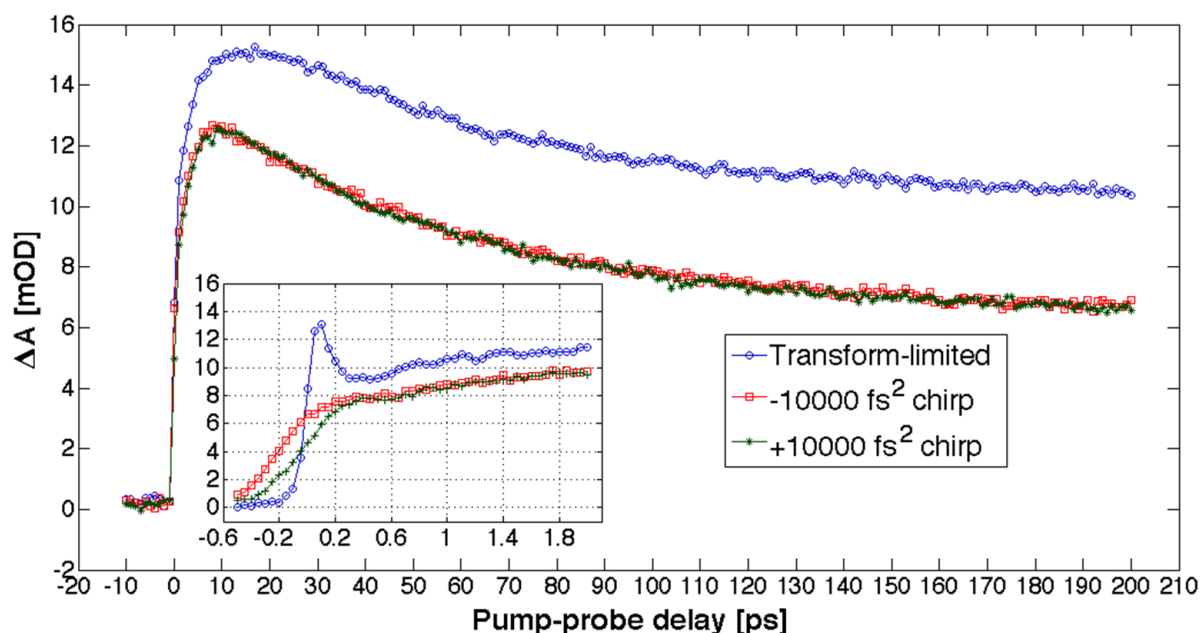
Figure 2.5: Time-resolved differential absorption signal at 800 nm with TL (blue), positively chirped (green) and negatively chirped (red) pump pulses of the same pulse energy. The traces at long (main figure) and short time delays (inset) share the same unit of time (picosecond).

(i.e. optical Kerr effect). Another piece of evidence for the change of dynamics concerns the dissociation-recombination turning point (peak of the long-time TA trace). With TL pump pulses, it happens at the pump-probe time delay of 16 ps, but with chirped pump pulses, this point is shifted to 5 ps earlier. At longer time delays, the sign of the chirp creates no difference in magnitude of the differential absorption signal (and therefore the $I_2^{-\bullet}$ yield). For the measured TA signal at all probe delays after time zero, the chirped pulses (with $\pm 10000 \, \text{fs}^2$ chirp) are less efficient at creating photoproducts than the TL pulse.

Fitting the long-time pump-probe traces in Fig. 2.5 yields the time constants shown in Table 2.1. The trace obtained with TL pump pulses is best fit with *three* components while the other two with *two* components, which put two time constants on commensurate timescales. Alternatively, if three components for the traces with chirped pump pulses are chosen, the confidence interval of the fitted time constants will be bigger

than the fitted values, indicating a wrong fit. This surprising feature strongly indicates that the TL pulse can generate an intermediate which caused the plateau-like feature in 10-20 ps region evident in the corresponding trace.

Table 2.1: Time constants for differently chirped pump pulses

Pump pulse chirp (fs^2)	τ_1 (ps)	τ_2 (ps)	τ_3 (ps)
0	2±1	9±3	51±4
10^4	3.5±0.2		54±1
-10^4	3.0±0.2		57±2

NB: The range in each time constant represents the 95% confidence interval from the fitting procedure.

2.3 Discussion and conclusion

In the experimental results presented in this chapter, the significant modification of photodissociation yield, reflected in the chirp and power dependence of the differential absorption signal is direct evidence of control, but the physical processes that contribute to it may not be easily traced. The limitation of probing with a single wavelength is that spectral averaging can belie the effect of other underlying mechanisms, e.g. spectral shift, on the observed symmetry of the chirp dependence in Fig. 2.4b. Only a control experiment with a spectrally-resolved broadband probe (i.e. that of a supercontinuum dispersed into a spectrometer) can elucidate such issue. However, aside from the spectral shift argument, which a recent experiment on high-field control has made a good case [95], the chirp and power dependence presented in section 2.2.2-2.2.3 strongly suggest the existence of some additional pump-absorbing chemical species or pathways that can reduce the observed photodissociation yield at different time delays. In lieu of this, the two likely scenarios capable of accounting for the observations are [96],

Cascaded single-photon absorption of the reactant: This amounts to a $\chi(1) : \chi(1)$ process for I_3^- and involves an electronically accessible upper excited state. The effect
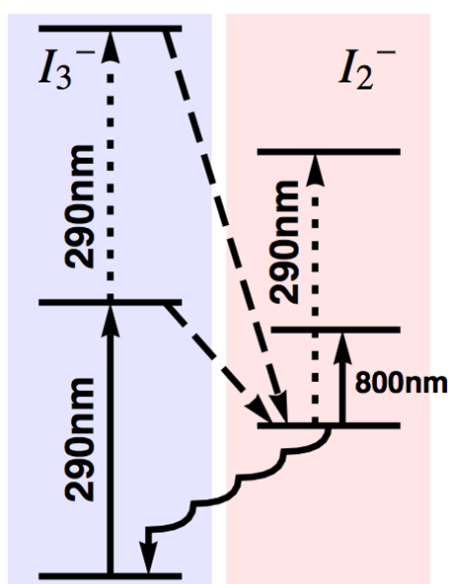
Figure 2.6: A modified energy diagram involving proposed additional mechanisms to account for the observed phase and amplitude control results. The lowest three energy levels comprise the original energy diagram involved in the triiodide reaction through the $I_2^{-\bullet}$ channel. The two added upper levels are accessible by cascaded single-photon absorption of I_3^- or pump-photon absorption of $I_2^{-\bullet}$.

is more effective with TL pump pulses due to their higher peak intensity relative to the chirped pulses.

Photoabsorption of photoproducts: This can happen only after $I_2^{-\bullet}$ is produced after approximately a vibrational period of the symmetric stretching mode of I_3^- (300-350 fs). For the long pulse used in the chirp scan, this can function as a parasitic effect that masks the real chirp dependence of $I_2^{-\bullet}$ formation. From previous experimental and theoretical studies, it is known that $I_2^{-\bullet}$ has two dissociative upper electronic states that link to its two absorption bands [97, 98]. In this way, the reaction is transformed into a sequential single-photon dissociation process.

A visual presentation of the new model involving these two photoabsorption mechanisms is depicted in Fig. 2.6. In actuality, these two mechanisms may well coexist to give rise to the observations discussed earlier in this chapter.

As this chapter shows, we can use the so-called coherent control protocols to affect the yield and the branching ratio of a photochemical reaction but we cannot unambiguously interpret the effects of the pulse shape. The main limitation of coherent control

is connecting the desired pulse shape dependence to the microscopic details related to the molecular dynamics of interest. This situation is the classic inversion problem that occurs in physics [99] with multiparameter degeneracies in the observables [100]. Coherent control using all optical methods can, at best so far, only derive the optimal pulse shape inverted to the control mechanism as underlying molecular dynamics for simple system with exactly known ground states [101]. Even here for the I_3^- system, the creation of intermediates in solution with unknown PESs will render such an unique inversion of pulse shape impossible. In this regard, ultrafast electron diffraction (UED) can provide directly the atomic motion influenced by the pulse shape and project out the light-matter interaction leading to control. Combining optical coherent control with (solution-phase) UED will allow us to uniquely invert the optimal control or open loop control pulses to uncover their effects on the molecular dynamics. The present studies are important as they lay the groundwork for probing quantum coherence in molecular reaction dynamics as well as provide further characterization of the operating dynamics in a previously well-studied experimental condition (I_3^- in EtOH). This development is, therefore, a first step for enabling structural probes to be applied to coherent control experiments, and will herald a new approach for testing time-dependent *ab initio* theories for reaction dynamics and our understanding of how to steer chemical proceses.

3 Combining broadband transient absorption spectroscopy with ultrafast electron diffraction

Outline: This chapter begins with a description of the crystalline environment of solid state TBAT. It proceeds with a critical assessment of the previous results on femtosecond time-resolved study of solid state triiodide samples. Then two separate experiments using broadband TAS and UED are presented. In the end, the connections between the two experiments are discussed.

  Contributions: Dr. Cheng Lu grew the TBAT samples in Toronto for the UED experiments, I grew additional TBAT samples in Hamburg for the TA measurements. I prepared them using ultramicrotome. Conducted the experiments along with help from Dr. Stuart Hayes and Dr. Gastón Corthey. I performed global analysis of the transient absorption data using the code devised by Dr. Valentyn Prokhorenko. I further performed advanced frequency analysis of the residuals.

3.1 The triiodide reaction in solid state

3.1.1 Crystal structure and absorption spectrum

Triiodide ion is able to form ionic crystals with various organic counterions [14]. Studying the triiodide reaction in the solid state requires a compound with a cation without overlapping absorption bands with I_3^-. To expand on a previous solid state study [26], experiments are carried out on crystalline TBAT (n-Bu$_4$NI$_3$). The single crystals of TBAT have a black appearance and needle-like or elongated shapes (see Fig. 3.2b). The needle-shaped crystals are not used for the experiments because

(a)

(b)
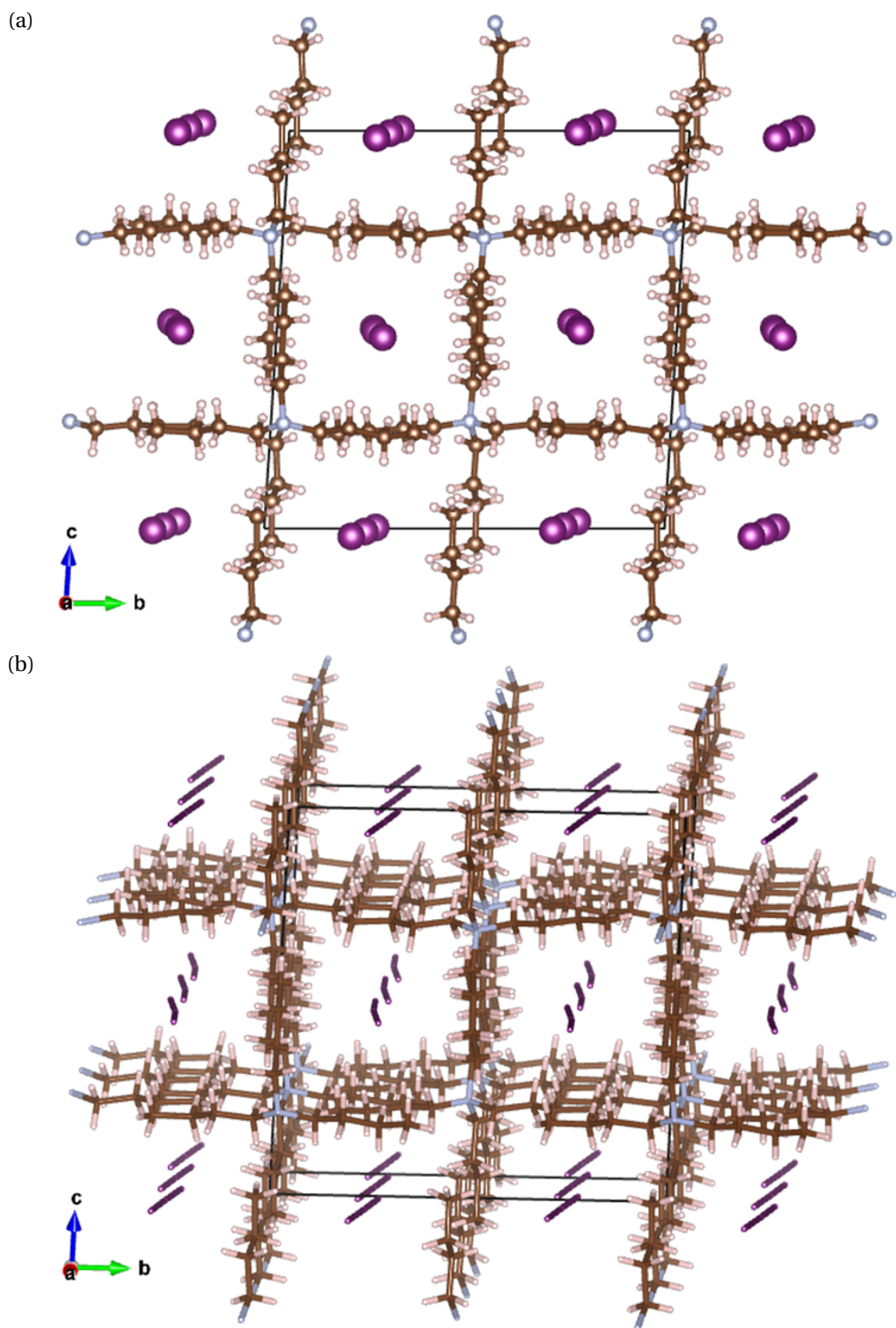
Figure 3.1: (a) Ball-and-stick structure of tetra-n-butylammonium triiodide viewed from the crystallographic **a** axis. (b) A stick-only view of the same cut-out of the crystal slightly tilted away from the **a** axis. In both figures the black parallelepiped frame demarcates the boundary of a single unit cell. The atomic coordinates are taken from X-ray refined structure recorded at 173 K [103]. The figures are generated using VESTA [104].

of their very limited usable area. The absorption spectrum of solid TBAT sample shows two shifted and broadened bands in the UV-Vis region (250-800 nm) compared with solvated I_3^- (see Fig. 3.2a). The shifts are ~ 20 nm for the D band and ~ 50 nm for the C band. The appearance of a long tail toward the red end is partly due to scattering and partly the growth in intensity of the spin-flip absorption bands A and B as assigned in [102]. These remarkable differences are the makings of the crystalline environment. Structurally speaking, in a TBAT crystal there exist two types of I_3^- chains, here referred to as the straight and the bent chains, with the I-I-I bond being 178° and 175°, respectively. More details on the crystal structure are given in Appendix B. The simplest approximation to interpret the spectrum in the UV-Vis region is to consider a linear combination of two distinct absorption spectra from the two crystallographically independent chains with different I-I-I angles mentioned earlier. This interpretation has been confirmed by comparing quantum chemical calculations in the gas phase I_3^- and solid state TBAT[1]. Physically speaking, the slightly bent geometries relax the selection rules of the perfectly straight I_3^- ions in the gas phase and shift the energies of the bonding orbitals that contribute to the electronic transitions. Therefore, some of the spin-flip transitions become allowed and the transition energies are shifted accordingly. The facts most relevant to the experiment are that I_3^- absorbs relatively more strongly in its C band than D band in the solid state than in solution, and 400 nm, simply the second harmonic of a Ti:Sapphire laser system, is very close to the center (~ 410 nm) of the C band of solid state TBAT.

3.1.2 Pump-probe experiment with 300 nm excitation

Due to the partial reversibility of the triiodide reaction in the solid state, only one attempt has been made to study it so far using single-shot spectroscopy [26]. In this work, Poulin and Nelson divided the wavefront of the probe pulses into 400 parts using two echelon gratings at right angles, before focusing onto the sample [106, 107].

---

[1]The results of the theoretical calculations are shown in Appendix E. I thank Professor Carole Morrison and Dr. David Rogers for their elucidative calculations that greatly helped with the understanding of the convolved spectrum in the solid state.
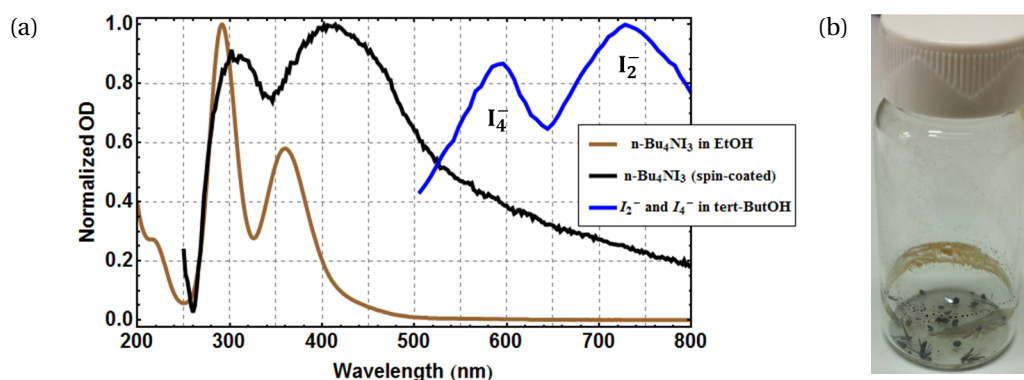
Figure 3.2: (a) Comparison of normalized absorption spectra of triiodide in solution (brown) and in solid state TBAT (black). The C and D bands in solution retain their labels in the corresponding solid state redshifted absorption bands. The blue curve shows absorption peaks of $I_2^{-\bullet}$ and $I_4^{-\bullet}$ obtained in tertiary butanol (*tert*-BuOH), adapted from [105], which will become useful in a later discussion. (b) TBAT crystals of slightly different morphologies (e.g. acicular, columnar, tabular) grown from evaporating saturated alcoholic solution.

In this way, every two spatially adjacent diffracted beamlets are time-delayed by 25 fs. In their study, the pump pulses were centered at 300 nm (D band excitation), the probe was the output from a NOPA which can be tuned throughout the absorption band of $I_2^{-\bullet}$ in the red. The bandwidth within the NOPA spectrum (tens of nanometers) was binned together to form a single trace. Since the experiment was carried out at room temperature and at relatively high excitation fluence, the sample suffered irrecoverable damage in the form of discoloration visible by eye after a maximum of about 20 pump shots[2].

From their arduous work, the authors compared the photoinduced geminate recombination of three different triiodide compounds in solid state. The results of two (TBAT and TPPT, or tetraphenolphosphonium triiodide) with very distinct features are displayed in Fig 3.3. The TBAT reaction recovers almost completely within 3 ps after time zero while the TPPT reaction is far from complete within the 8 ps detection range. The explanation following this work attributed these distinct behaviors to a

---

[2]From private conversation with Professor Keith Nelson during the FEMTO12 conference.

direct evidence of the lattice confinement of the reaction. According to them, the 1D geometry of the I_3^- ions in TBAT facilitates the recovery process through fast geminate recombination *in situ*, whereas in TPPT, the reaction happens such that the photofragments have to diffuse around to the next reaction site before recombination thanks to the spacious voids provided by the crystal structure. Therefore the recombination rate of TPPT was measured to be drastically slower than that of TBAT. In their experiment, however, the sample thickness was not precisely measured, only an estimate of ∼ 200 μm was given in Poulin's thesis [25]. The samples grown from solution were directly used without further thinning, so low probe transmission was mentioned as a serious problem [25] during data acquisition.
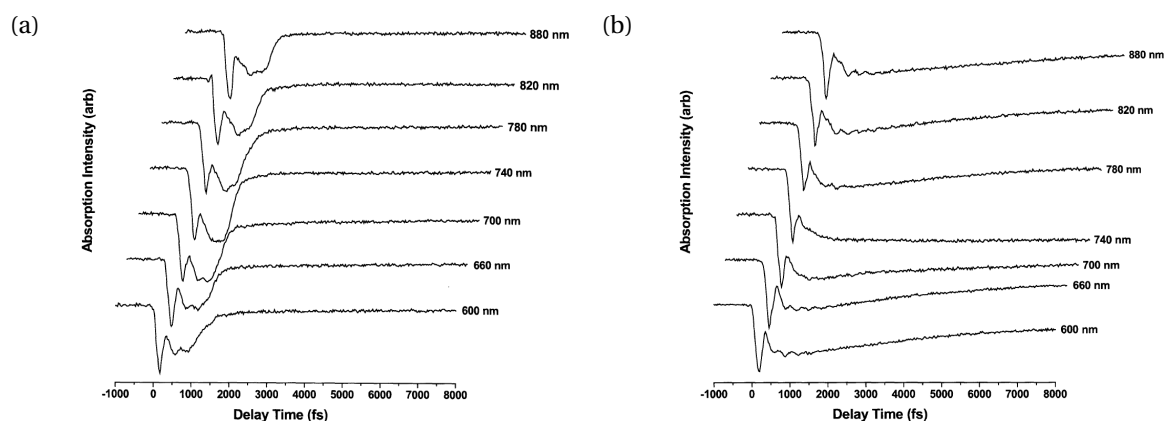
Figure 3.3: Frequency-resolved pump-probe studies of solid state triiodide compounds, (a) TBAT and (b) TPPT with 300 nm optical excitation and color-tunable probe pulses. The figures are adapted from [25] with permission.

3.2 The 400 nm-pump-supercontinuum-probe experiment on solid state TBAT

We extend the above pump-probe experiments to the C band of TBAT (see Fig. 3.2a) with 400 nm photoexcitation as part of the required background studies for the UED experiment to follow. From the optical pump-probe experiment we want to get a glimpse of the expected dynamics in the solid state for samples prepared under

similar conditions, and to determine the number of potential photocycles as well as the appropriate excitation condition.

3.2.1   Optical pump-probe setup

Details of the experimental setup is shown in Fig 3.4a. The pump and the probe pulses were derived from the same ultrafast Ti:Sapphire laser (Coherent Elite USP), with an output of ~ 40 fs operating at 500 Hz and centered at 800 nm. This laser fundamental was frequency-doubled to produce the excitation pulse at 400 nm. The probe pulse was a supercontinuum (or "white light") generated by focusing the laser fundamental into a 2 mm-path-length quartz cuvette (Hellma) filled with de-ionized water. The pump and probe beams were collimated and focused separately onto the sample inside the vacuum chamber of a liquid nitrogen cryostat (Oxford Optistat DN-V2). The cryostat sat in a custom-designed support that connects to an X-translation stage and a jack, enabling two-dimensional control of the sample position by moving the cryostat. The sample temperature can be regulated down to 77 K by feedback control of the heater current. Samples were cut to ~ 1 μm thick (OD ~ 1 at 400 nm) from solution-grown crystals (see Fig. 3.2b) using an ultramicrotome (Leica EM UC7). The sample preparation procedures were chosen to best approximate that for electron diffraction, and they will be detailed in section 3.3.2.

Before the measurements, the polarization of the pump pulse was set to optimize the transient absorption signal (maximize growth and/or minimize bleaching) at a fixed time delay. The transmitted probe beam is detected using a home-made grating-based Czerny-Turner-type spectrometer equipped with a back-thinned CCD (Hamamatsu S11155-2048-02) run on its fast electronic board (Hamamatsu C11165-02), which enabled detection of single laser shots.

42
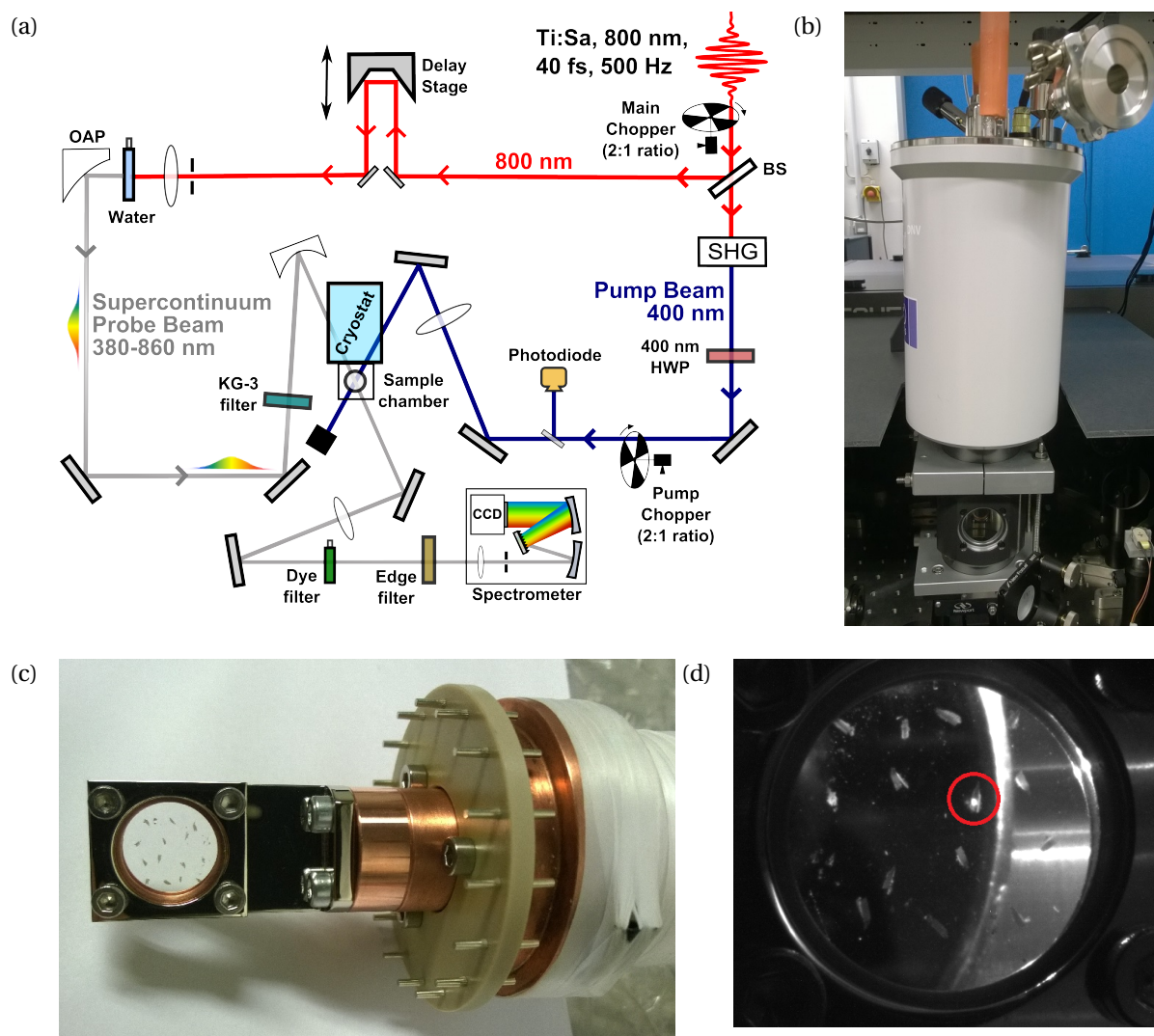
Figure 3.4: (a) Schematic of the optical pump-probe setup with 400 nm optical excitation and supercontinuum probe. At the center is a liquid nitrogen cryostat, the photograph of which is shown in (b). The samples were placed on a fused silica substrate, which was sandwiched between two copper rings and the cryostat's sample holder pieces as shown in (c). Scattering of laser beams from the surface of the sample, like that shown in (d), was registered by a camera to assist in optimizing the pump-probe spatial overlap before measurements.

TBAT crystal growth

Sample preparation used 97.0% pure n-Bu$_4$NI$_3$ purchased from Sigma-Aldrich, which was directly used for crystallization. Since TBAT doesn't have a high solubility in most common solvents, ethanol was chosen as the solvent for simplicity. The black

crystals forms in a matter of ~ 3 weeks from evaporating saturated EtOH solution. Recrystallization was sometimes needed for increasing the thickness of the crystal for ease of mounting and cutting. Previously, another method of crystallization by adding I_2 to saturated n-Bu$_4$NI solution was used. These two methods yielded crystals with comparable sizes and quality.

Spectral tinkering of the supercontinuum probe

A discovery made more than a decade ago [108] showed that the spectral width of a supercontinuum is positively correlated with the bandgap of the generating medium. For this experiment, water was chosen as the supercontinuum medium because of its large bandgap (~ 7.5 eV), which makes the blue edge of its supercontinuum extend below 390 nm whereas traditional materials like sapphire (6.9 eV bandgap) terminates at ~ 450 nm. Moreover, no rotation of the source is required to keep it free of optical damage, as is the case for alkaline halides like CaF$_2$ (12.0 eV) [109] and LiF (13.6 eV) [110]. A bandpass filter from colored glass KG-3 (passband 315-710 nm) was used to reduce the intensity of the spectrally-broadened fundamental in the 750-800 nm region after it passed through the 2 mm water cuvette. In addition, a dye filter composed of a mixture of IR-780, IR-140 and IR-820 dyes in MeOH was placed before the spectrometer to attenuate the region close to the 800 nm pump to avoid saturation of the CCD on the single-shot level. These dyes have absorption peaks at 780 nm, 800 nm and 820 nm in MeOH, respectively. This arrangement also kept the chirp introduced by the dye filter from affecting the time resolution at the sample position. The probe pulse energy before the sample was ~ 18 nJ with a FWHM of 100 nm and the detection window spanned over an octave from 380-855 nm. During experiments, an edge filter with a cut-on wavelength of 400 nm was placed before the spectrometer to reduce the pump scattering, trimming the net detection window down to 405-855 nm.

44

Detection scheme and data analysis

To circumvent optical and photothermal damage, the repetition rate of the pump pulses was reduced to 125 Hz (probe pulses at 250 Hz) using two choppers as depicted in Fig 3.4a. The main chopper was placed before the pump-probe beam splitter, a small portion of its output was picked up by a photodiode to convert it into a TTL signal for triggering the pump chopper. In this way the mechanical instability of the master-slave chopper operation was minimized for single-shot detection using the fast CCD. The voltage readings from the photodiode after the pump chopper was registered by a NI-DAQ card for sorting the pump-probe spectra and normalizing the differential absorption data. The differential absorption was calculated using the formula,

$$dA(\lambda, t) = -\log_{10} \frac{I_{\text{pon}}(\lambda, t) - I_{\text{bkgd}}}{I_{\text{poff}}(\lambda, t) - I_{\text{bkgd}}} \tag{3.1}$$

where $I_{\text{pon}}(\lambda, t)$ and $I_{\text{poff}}(\lambda, t)$ are spectrally resolved 2D intensity arrays directly obtained from the CCD. An outlier-rejection algorithm (with details in Appendix D) was used to remove the noise caused by chopper instability and perform averaging before $dA(\lambda, t)$ was calculated.

3.2.2 Setup calibration

The instrument response function (IRF) of the pump-probe setup was estimated by measuring the Kerr effect response from the fused silica substrate used for supporting the sample. The result is shown in Fig. 3.5. From fitting to a sine-modulated Gaussian curve of the form, $A\sin(2\pi f t + \phi)\exp\left[-4\ln 2 \cdot \left(\frac{t-t_0}{\text{FWHM}}\right)^2\right]$, the FWHM of the IRF throughout the probing window was found to be 240-280 fs, depending on the wavelength. The IRF is clearly probe-limited due to its uncorrected spectral chirp.
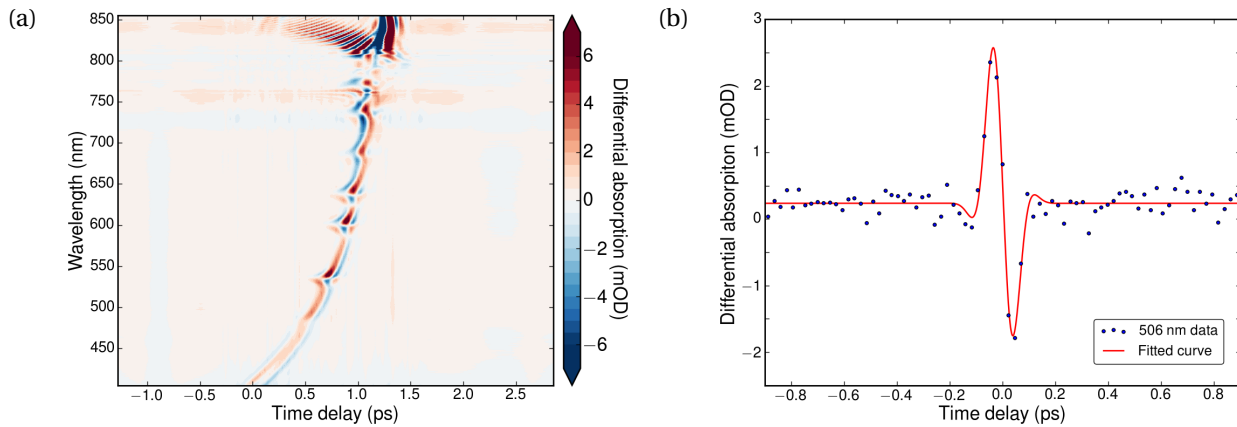
Figure 3.5: Transient Kerr response from the fused silica substrate (a) across the detection window and (b) a line cut along the specified wavelength range, the Gaussian part of the fitted curve has a FWHM of 127±21 fs.

3.2.3 Polarization dependence

The directionality of the I_3^- chains defines a clear macroscopic transition dipole moment, which exhibits a strong dependence on the polarization of the excitation pulse. This dependence was measured by varying the pump polarization using a half-wave plate (HWP) while maintaining that of probe's and record the differential absorption signal at a fixed time delay. The result is presented in Fig. 3.6, complete with fitted curves using the expression $dA(\theta) = a + b\cos(\theta + \theta_0)^2$.

First of all, the polarization dependence confirms the quality of the sample, since a disordered sample (e.g. spin-coated) would have a negligible excitation polarization dependence. Another interesting feature is that, while the ground-state bleaching signal is almost zero at the perpendicular polarization, the growth signal from $I_2^{-\bullet}$ production has a finite offset from zero even at its minimum, indicating the existence of a possible independent contribution to the signal. Lastly, the slight difference ($\sim 15°$) of the minimum-signal pump polarization (MSPP) between the bleaching and the growing bands is most likely[3] due to the orientation difference between of $I_2^{-\bullet}$ and

---

[3]Another possible explanation is the non-identical polarizations of the different colors present in the supercontinuum probe pumped by linearly-polarized 800 nm pulses, but the sudden transition of

(a)

(b)
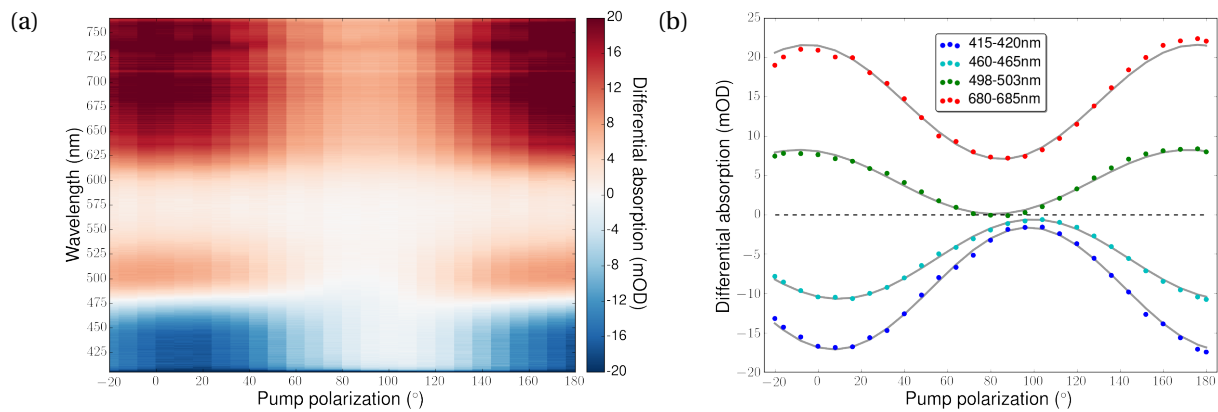
Figure 3.6: (a) Pump polarization dependence of the differential absorption signal at a fixed pump-probe delay across the detection wavelengths. (b) Line cuts through the 2D diagram in (a), averaged over four representative wavelength regions along with fitted grey curves. The measurement was performed at 245 K.

I_3^-. This 15° difference bears resemblance to the dihedral angle formed between the two types of I_3^- chains in the unit cell (see Appndix B). The polarization dependence measurements performed at 80 K and 245 K showed similar features.

3.2.4 Fluence dependence and sample reversibility test

Fluence dependence of the sample response was measured at 80 K with an excitation energy at sample position varied from 90 nJ to 631 nJ, corresponding to the fluence from 0.0953 to 0.671 mJ/cm^2 (or from 1.92×10^{14} to 1.35×10^{15} photons/cm^2)[4]. The results are displayed in Fig. 3.7, a linear dependence can be extrapolated up to the highest fluence used, which confirms that the experiments are within the linear excitation limit.

To test the sample reversibility at different temperatures, differential absorption was measured at a fixed pump-probe delay at four sample temperatures (80 K, 135 K, 190 K and 245 K). Representative results at 245 K are shown in Fig. 3.8. It is evident from this measurement that the optical damage to the sample is negligible at a low excitation

---

the MSPP at around 475 nm, which is where the $I_2^{-\bullet}$ and I_3^- bands cross, makes this a less likely scenario.

[4]Damage to the sample was seen at higher fluences, where the green spectral region developed a bleaching band that only strengthened in magnitude in consecutive scans.

(a)

(b)

(c)

(d)
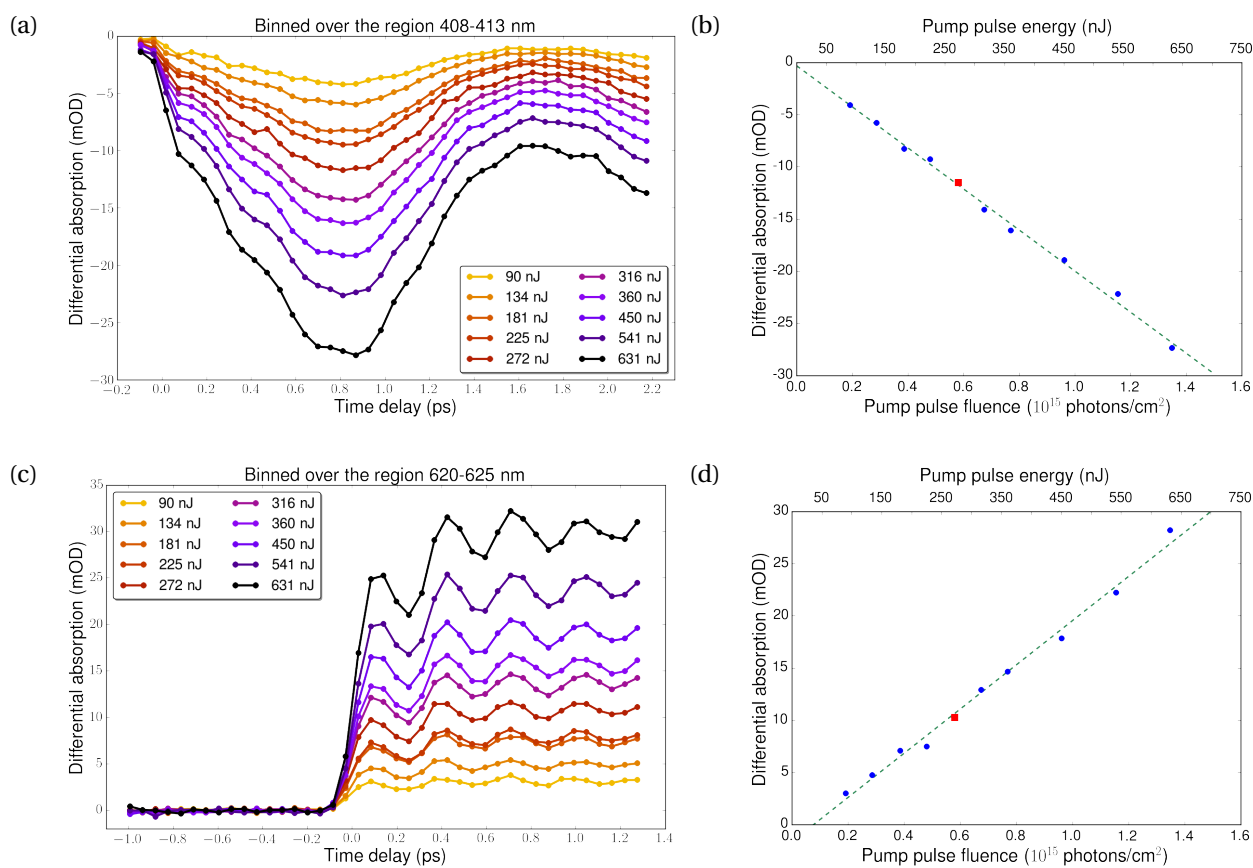
Figure 3.7: Fluence dependence of (a) the bleaching band and (c) the growing band (spectral range specified in the figure title). To examine the dependence more quantitatively, the differential absorption signals at a few time points in each trace measured at a specific excitation fluence were averaged to construct a representative signal value. These time points were chosen around a probe time delay of 0.8 ps from (a) and 0.4 ps from (c). Then the representative signal values are plotted against the excitation fluence in (b) and (d), for spectral regions of (a) and (c), respectively. In either case a linear fit describes the relationship sufficiently and the fit is also included in each plot. The red squares in (b) and (d) indicate the typical pump fluence used in the pump-probe measurements described later. The modification of oscillation amplitudes at high fluences is mostly due to the change in kinetics (as in (c)) or the strengthening of a mode that is very weak at lower fluences (as in (a)).

fluence (the same is true at other measured temperatures). Lowering the sample temperature was found to change the recovery rate of the reaction. The follow-up section presents and discusses the similarities and differences of TA signal measured from 80 K up to 245 K.
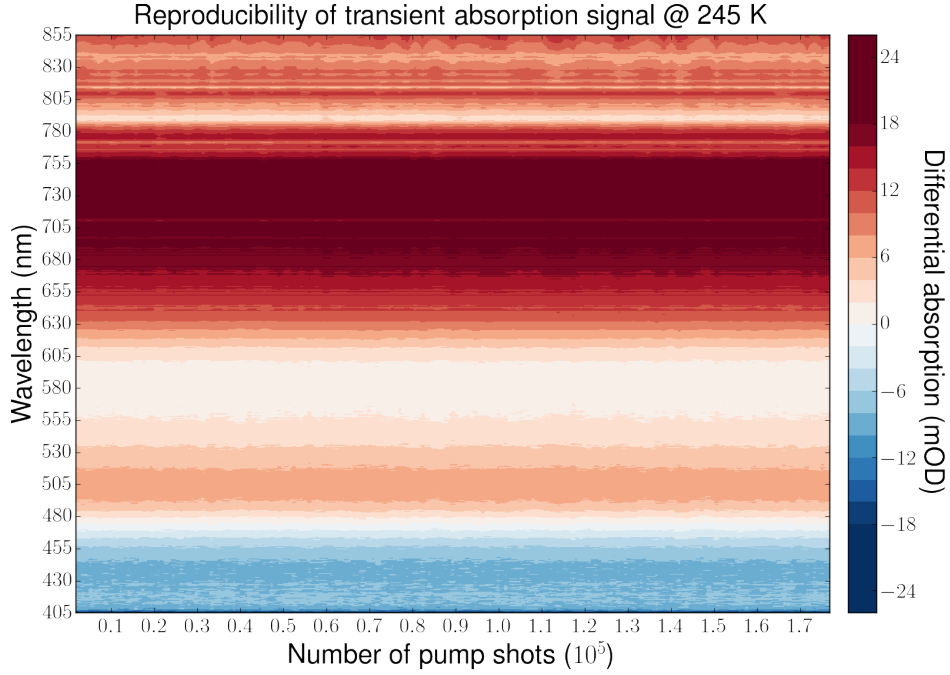
Figure 3.8: Transient absorption measurement performed at 245 K with a fluence of 0.31 mJ/cm^2 (6.3×10^{14} photons/cm^2) and at a probe delay of ∼ 600 fs after time zero. The filled contour plot shows the consistency of the transient absorption signal detected across the spectral window from 405-855 nm. The artefact in the region around 800 nm is due to the instability in the white-light probe.

3.2.5 Temperature-dependent short-time dynamics

At all temperatures where measurements were conducted, the initial part of the transient absorption signal is strongly modulated by coherent oscillations up until about 10 ps after time zero. To disentangle these oscillations from the underlying population dynamics, global analysis [43, 111] was first applied to extract the population dynamics from 2D time-resolved traces (e.g. Fig. 3.9a) using the fitting function,

$$\Delta A(\lambda, t) = \mathrm{IRF}(\lambda, t) \otimes \sum_i \mathrm{DAS}_i(\lambda) \exp[-t/\tau_i] \qquad (3.2)$$

where IRF(λ, t) is the wavelength-dependent instrument response function. This deconvolution scheme was achieved using the *Analyzer_PP* program developed by Dr. Valentyn Prokhorenko [111]. Then the residuals from the fitting at different

wavelengths were analyzed using continuous wavelet transform (CWT) and short-time Fourier transform (STFT). The theoretical background and proof of reliability of these frequency analysis techniques is presented in Appendix C. In the following subsections, the focus of the text is on the broadband TA data acquired at 245 K because of its immediate relevance to the electron diffraction experiment (carried out at the same temperature). Data at other temperatures are briefly discussed for comparison.

Fast dynamics at 245 K

The short-time (< ~ 16 ps after time zero) wavelength-resolved transient absorption spectrum is shown in Fig. 3.9a. The two dominant features are the bleaching and the growing bands residing, respectively, in the shorter and longer wavelength side of the spectrum. Comparing with the absorption profiles in Fig. 2.1a and Fig. 3.2a, it is reasonable to attribute the growing band to mostly the generation of $I_2^{-\bullet}$ and the bleaching band mostly to the depletion of I_3^-. The spectral region around 550 nm with little change of absorption correlates well with the absorption minimum of $I_2^{-\bullet}$ in solution (see Fig. 2.1a). Further detailed analysis divides the probed spectral window into six regions, each with slightly different but related dynamical features. For each region, a representative trace is selected for frequency analysis after binning in a wavelength range (4-10 nm) with very similar dynamics. The tentative mode assignments used in the following are based on a previous resonant Raman experiment performed at 77 K [112, 113]. The frequency analysis results are presented pictorially for regions A, B, D and E, which are of importance to the identification of photoproducts and reaction channels. To maintain a consistent trade-off between time and frequency resolution, the same set of three wavelets and two Tukey windows [114] are used in the following time-frequency analyses, unless otherwise mentioned. More details on the methods used are given in Appendix C.

   Region A (405-475 nm): This region is dominated by the bleaching signal of ground-

(a)

(b)
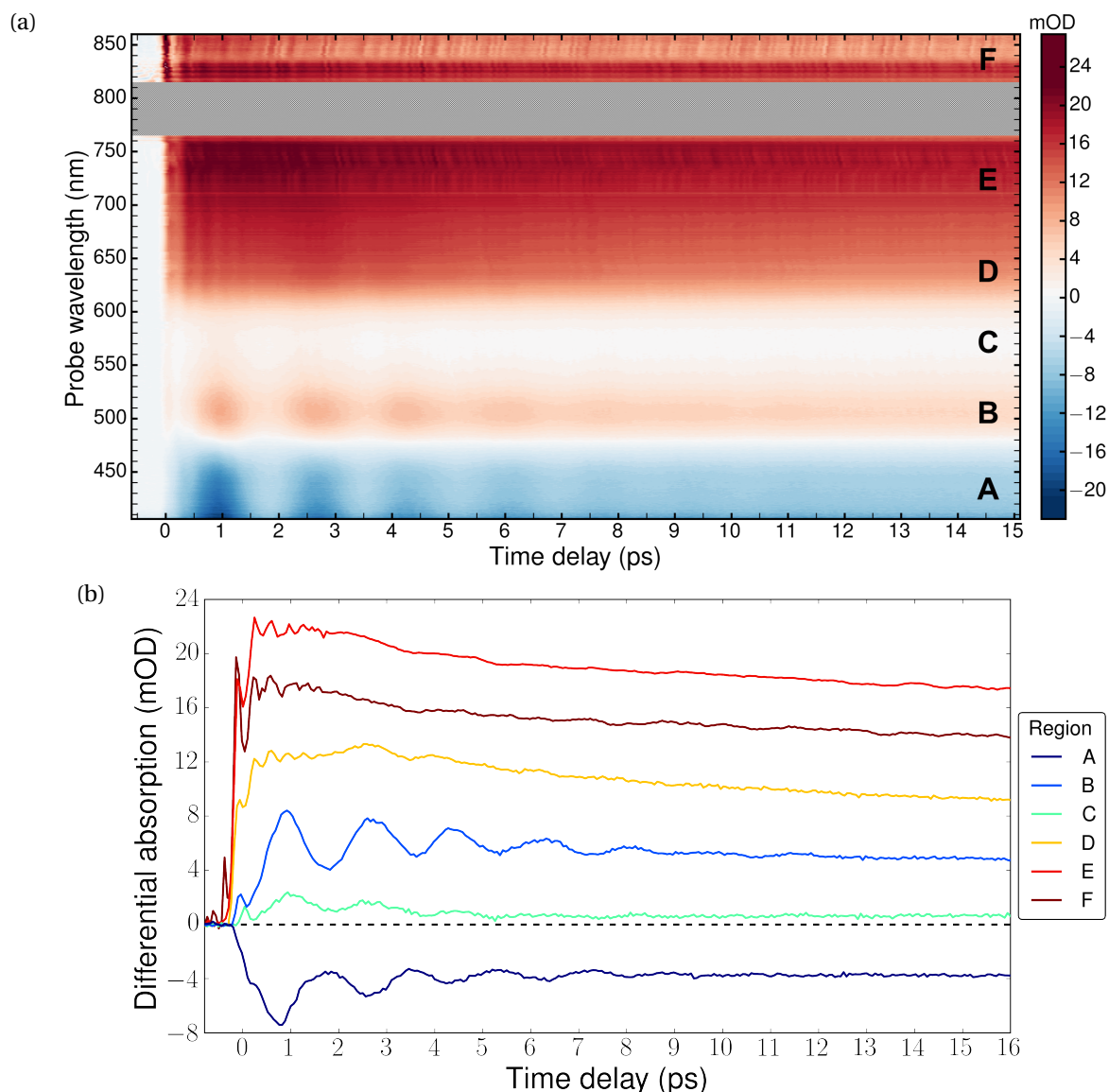
Figure 3.9: (a) TA spectra at 245 K recorded with 60 fs steps. The hatches block the region affected by the instability near the 800 nm supercontinuum pump. This region has poorer instability due to the collective effects of multiple nonlinear optical phenomena. (b) Representative traces from every region labeled in (a), the curves in regions E and F were smoothed using a Savitzky-Golay filter after a time delay of ~ 2 ps in order to compare with the rest on the slower dynamics. The time zero for each trace in (b) was adjusted using the shift parameter obtained from exponential fitting using the *Analyzer_PP* program.

state I_3^-. A very pronounced 20 cm^{-1} libration mode is seen with coherence lasting for ~ 9 ps. The oscillations with smaller amplitudes on top of the libration mode in this
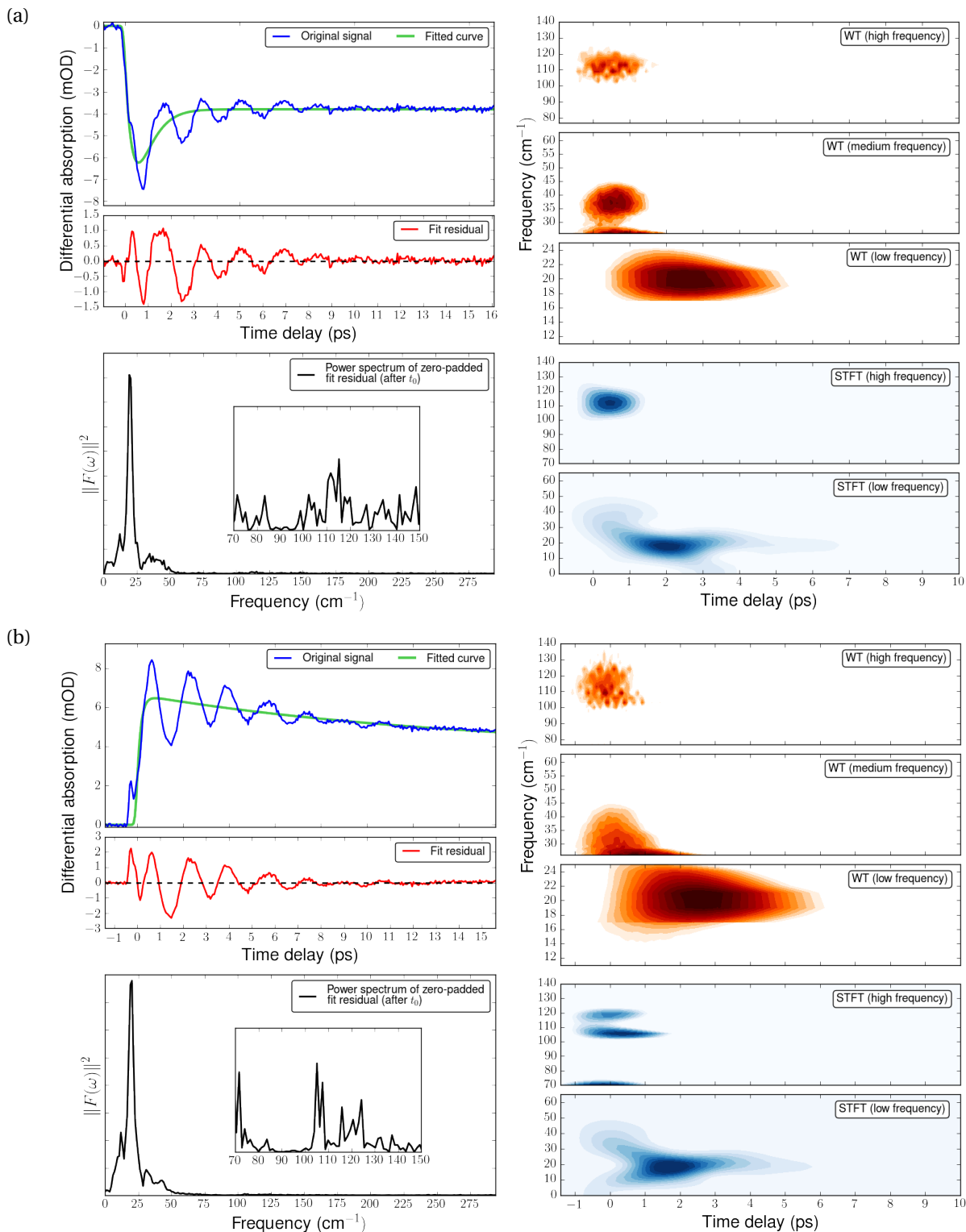
Figure 3.10: Frequency analysis of a typical trace in (a) region A at 464 nm (binned over 462-466 nm) and in (b) region B at 510 nm (binned over 505-514 nm). The binning ranges were chosen for a region with similar dynamics. In each case, the upper left corner shows the trace in blue and the fitted population dynamics in green, the difference of the two is the residual plotted in red. Fourier transform of the residual cut after time zero is shown on the lower left corner, along with an inset zooming in on the high frequency region. The plots on the right side show analyses using multiple wavelet transform scalogram and spectrogram (from short-time Fourier transform, or STFT) in different frequency regions. Different color scalings were used to expose the important features in each region.

band are identified to have a frequency of ~ 35 cm^{-1} and 113 cm^{-1}. The latter can be assigned to the impulsively excited ground state symmetric stretching mode of I_3^-, which matches perfectly the frequency observed in solution phase studies [82, 85, 86]. The frequency composition of a typical trace in this region is shown in Fig. 3.10a. As is evident in the time-frequency representations, the onset of the libration mode appears to be delayed from the stretching mode oscillation.

Region B (475-530 nm): After a crossover region near 475 nm the bleaching band turns into a growing band (see Fig. 3.10b), a signature that the positive contribution of the photoproducts (e.g. $I_2^{-\bullet}$) starts to dominate the TA trace. The phase of the libration mode oscillation is shifted through the crossover region by about π away from those in region A, which makes a typical trace at the center of region B be in antiphase with one at the center of region A. The sign is inverted due to the overwhelming contribution from the growth of $I_2^{-\bullet}$. Moreover, the high-frequency band at > 100 cm^{-1} broadens in the CWT representation compared with region A. This is due to the limitation of the high frequency resolution of CWT. Using a longer temporal window in STFT than used to analyze region A to improve the frequency resolution, two separate components are identified from this broadened band, which confirms the existence of (at least) two species in this band.

Region C (530-605 nm): The amplitude of the very pronounced ~ 20 cm^{-1} oscillations in Regions A and B become much weaker here. This very weak growing feature that characterizes this region is highly likely the result of a valley between the two absorption bands of the photoproduct $I_2^{-\bullet}$ (see Fig. 2.1a).

Region D (605-700 nm): Beyond the transition region C, a new growing absorption band takes shape. Now the initial fast vibrational oscillation is intensified and its frequency is shifted down to close to 100 cm^{-1}. In addition, this frequency band starts to broaden towards the long-wavelength side of this region. The libration mode frequency has also dropped below 20 cm^{-1}. In addition, a ~ 30 cm^{-1} and a ~ 40 cm^{-1} mode appear in place of the ~ 35 cm^{-1} observed in the previous regions.
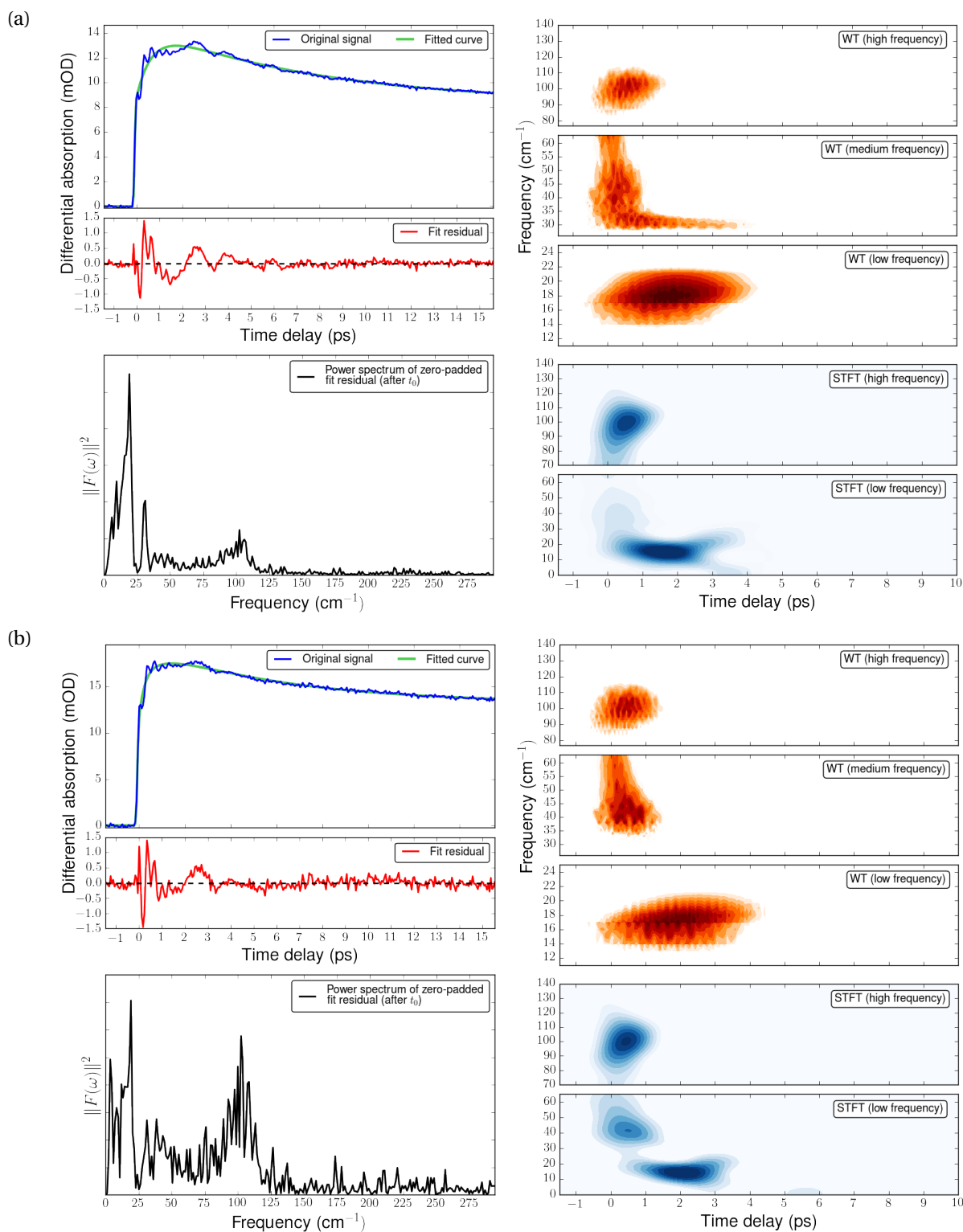
Figure 3.11: Frequency analysis of two traces in region D at (a) 630 nm (binned over 627-633 nm) and (b) 682 nm (binned over 677-686 nm), respectively. The same set of wavelets and the frequency windows as in Fig. 3.10a are used in the analysis.

Two decomposed traces in this region are shown in Fig. 3.11 due to the relative importance as it is linked to a new photoproduct $I_4^{-\bullet}$, which will be discussed in a later section.

Region E (700-775 nm): On the short-wavelength side of the growing band, the low-frequency libration mode becomes very weak and its frequency is shifted down to ~ 16 cm^{-1}, therefore its origin may be different. The region of the stretching mode in the CWT representation is now significantly broadened and sits at close to 100 cm^{-1}. This frequency band breaks down to three major components in the STFT spectrogram as shown in Fig. 3.12. The two components > 100 cm^{-1} that reflect the stretching vibrations of I_3^- and $I_2^{-\bullet}$, but the mode around 90 cm^{-1} is not known to be associated to any of the two species. Therefore, it can be a coupled mode between the lattice and the molecular motion or a mode from a distinct photoproduct.
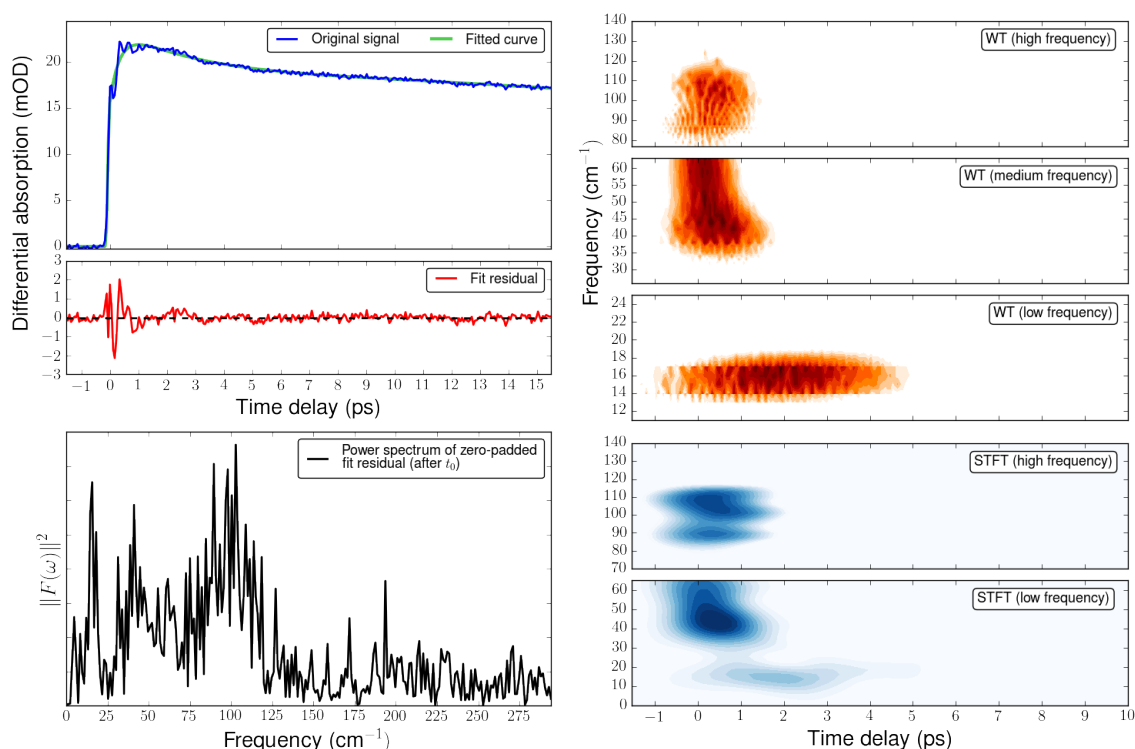
Figure 3.12: Frequency analysis of a typical trace in region E at 734 nm (binned over 730-737 nm). The high-frequency STFT used a longer window (therefore compromising time resolution) than that in the analysis of region A in order to expose the three frequency components in the 85-115 cm^{-1} range.

Region F (810-855 nm): On the red side of the growing band, a sharp spike is seen close to time zero, trailed by fast oscillations on par with the stretching mode of $I_2^{-\bullet}$ described in region E. The libration mode is not present in this region. Here the behavior is in line with the "coherent dissociation" picture described in Poulin's thesis [25]: the dissociation doesn't start from time zero and the initial spike was attributed to the excited state absorption of I_3^-. In the present experiment the region before time-zero around 800 nm is affected by coherent artifacts from the supercontinuum probe (see Fig. 3.9b).

These results of frequency analysis confirms the existence of at least two species, I_3^- and $I_2^{-\bullet}$, with overlapping absorption bands in the detection window distinguished by their slightly different stretching modes. From global analysis, the whole time range is well fitted with a combination of 4 exponentials from time zero to a pump-probe time delay of ~ 16 ps. The DAS corresponding to every one of them is shown in Fig. 3.14d with the lifetimes specified in the plot. $DAS_1(\lambda)$ exhibits a "tilted-balance" feature with the zero-crossing at around 475 nm. From the absorption spectra in Fig. 3.2a, it is evident that $DAS_1(\lambda)$ can only be associated with the decay onset of excited I_3^- after vertical transition on the time scale of the pump pulse duration (~ 100 fs). This is overwhelmed immediately by a growing contribution from the photoproduct $I_2^{-\bullet}$ (with a pronounced absorption band peaked close to 785 nm), as is reflected in $DAS_2(\lambda)$-$DAS_4(\lambda)$ in the sample plot. The decay of excited I_3^- and the growth of $I_2^{-\bullet}$ are the two dominant features within this time range.

Dynamics at lower temperatures

Time-resolved data from -1 ps to 16 ps were also recorded at 190 K, 135 K and 80 K with 60 fs time steps and a 125 Hz pump repetition rate. Visual representation of these data can be found in Appendix A. The general features of a bleaching band from I_3^- and two growing bands from $I_2^{-\bullet}$ were reproduced at all three temperatures. An outstanding feature among them is the shift of the low frequency bands towards even shorter wavelengths.
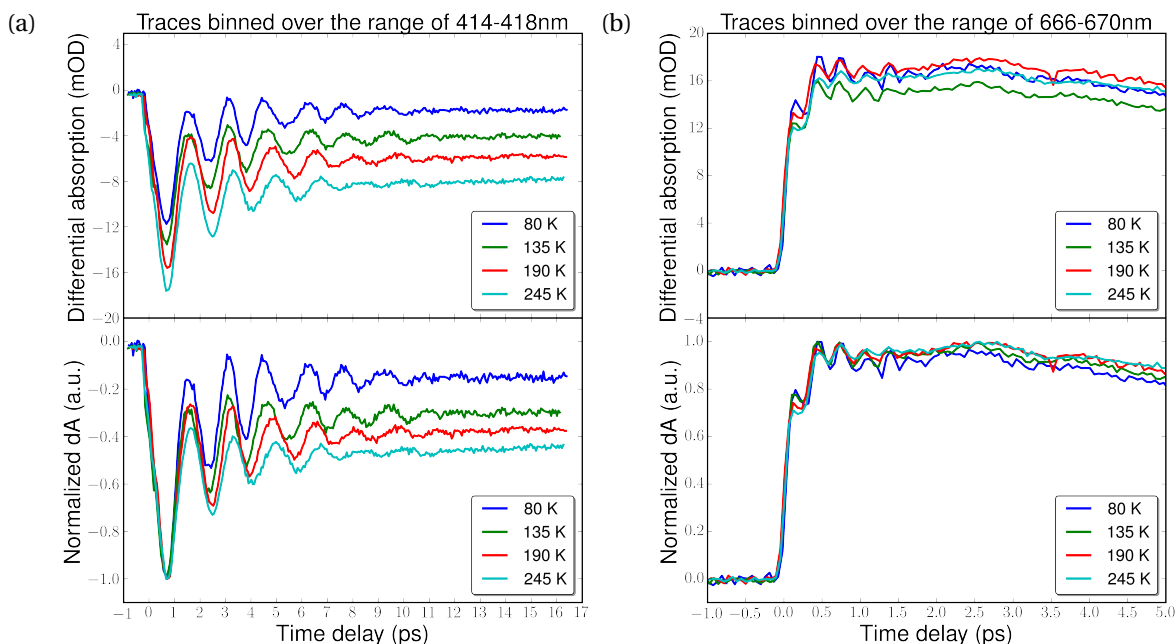
Figure 3.13: Comparison of (a) libration mode and (b) stretching mode oscillations at four different temperatures. A clear shift is seen in the libration mode (a lattice mode), while the stretching mode (a molecular mode) maintains its frequency.

The results of frequency analyses similar to those in the previous section show that the libration mode frequency is affected by the temperature but the stretching mode is not (see Fig. 3.13). Global analysis yields the DAS (see Fig. 3.14) and decay constants (excluding the long-lived component) for the datasets at the four temperatures are presented in Table 3.1. These results show that the sample temperature affects τ_1

Table 3.1: Time constants for short-time dynamics

Temperature (K)	τ_1 (ps)	τ_2 (ps)	τ_3 (ps)
80	0.23±0.01	1.48±0.02	6.60±0.09
135	0.24±0.01	1.26±0.01	5.39±0.06
190	0.24±0.01	1.05±0.01	5.92±0.06
245	0.24±0.01	0.86±0.01	6.34±0.05

NB: The range in each time constant represents the 95% confidence interval from the fitting procedure.

very little, since it stems from the vertical excitation of I_3^-, as evidenced in the positive feature on the short wavelength side (C band of I_3^-) and the negative feature on the long
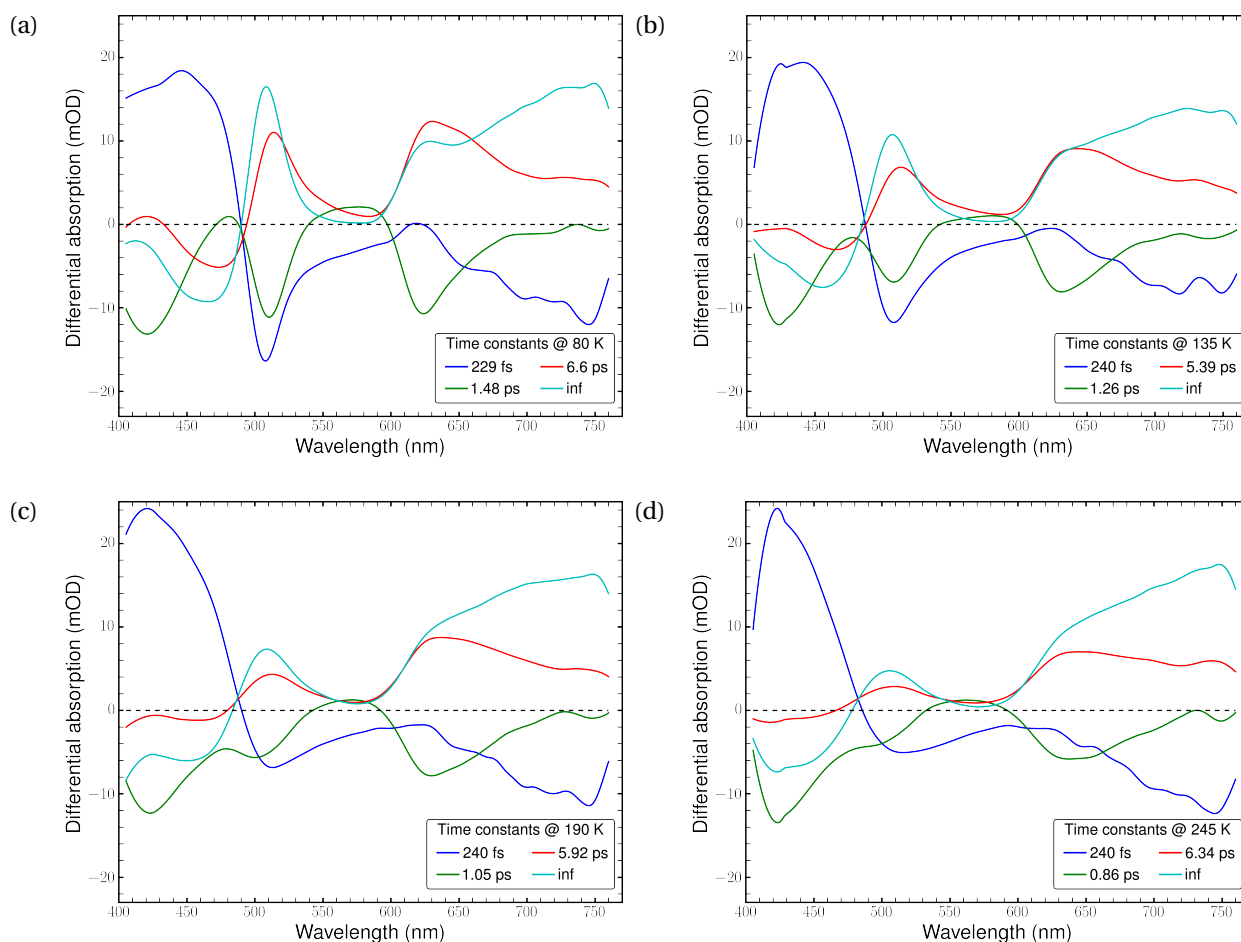
Figure 3.14: DAS from global analysis of the TA data at (a) 80 K, (b) 135 (K), (c) 190 K and (d) 245 K. The TA data were recorded with 60 fs time steps. The legend in the DAS diagram displays the time constants of each component. The component with a time constant of infinity is not resolvable within the range of data recorded.

wavelength side (near-IR absorption band of $I_2^{-\bullet}$). On the other hand, τ_2 is drastically reduced as the temperature increases, since it relates to the first time scale of $I_2^{-\bullet}$ formation. The DAS feature for τ_2 is the balancing of the population of I_3^- and $I_2^{-\bullet}$ in terms of total absorbance, which has now become evened out. This is thus a turning point in the reaction kinetics. On the next two time scales, the DAS in region B (475-530 nm) has decreasing amplitudes as temperature increases. This probably comes from the change of reaction rates and the band shift (see Fig. A.1 in Appendix A). The emergence of an unidentified band in the region 605-680 nm on the τ_3 timescale has never been observed in previous studies. Here it may indicate the existence of another

reaction intermediate such as $I_4^{-\bullet}$ due to spectral similarity (see [105] or Fig. 3.2b for the absorption spectrum of $I_4^{-\bullet}$ in alcoholic solution, in solid state the spectrum can be redshifted like that of I_3^-). The tetraatomic radical ion can be formed from an $I^\bullet$ fragment bonded to a nearby I_3^- chain.

3.2.6 Temperature-dependent long-time kinetics

The bleaching and growing bands formed in the short time exhibit a slow and unending recovery well into the ns timescale (the translation stage covered up to about 1.6 ns after time zero). The coherence of the reaction-associated modes is completely lost after ~ 12 ps for the low-frequency libration mode and the reaction transitions into purely population kinetics.

Pico- to nanosecond kinetics at 245 K

This dataset was combined from segments recorded with 1 ps, 5 ps/10 ps and 20 ps time steps (see Fig. 3.15). At long time delays the recovery proceeds in a multi-exponential manner, with different rates across the spectral window. These features are summarized in the following. A full collection of traces is presented in Appendix A.

Region A (405-480 nm): In addition to the recovery of the bleaching band, a weak growing feature is seen from a time delay of ~ 500 ps onwards. Since this region is overlapped by the D band of I_3^- and the high-lying absorption band of $I_2^{-\bullet}$, such growing feature is likely only caused by the difference in decay rate of $I_2^{-\bullet}$ and the recovery rate of photobleached I_3^- and/or their differing absorption coefficient in this region[5].

Region B (480-530 nm): A plateau is observed between 50-400 ps. The origin of it is likely the shift of bands due to vibrational relaxation.

Region C (530-605 nm): The signal level in the weak growing band that has little change from the chemical reaction decreases to close to zero after the coherence of

---

[5]If this is not true, the recombination pathway may be more complex than $I_2^{-\bullet}+I^\bullet \rightarrow I_3^-$.

the 20 cm^{-1} libration mode is lost within 10 ps.

Region D (605-730 nm), E (730-775 nm) & F (810-855 nm): the short- and the long-wavelength sides of the growing band decay at similar rates, implying that on this timescale the absorption of this broad band is due mostly to one species, $I_2^{-\bullet}$. Its bandwidth is maintained and no narrowing from, e.g. vibrational cooling, as reported in solution-phase experiment [25], is observed.

(a)

(b)
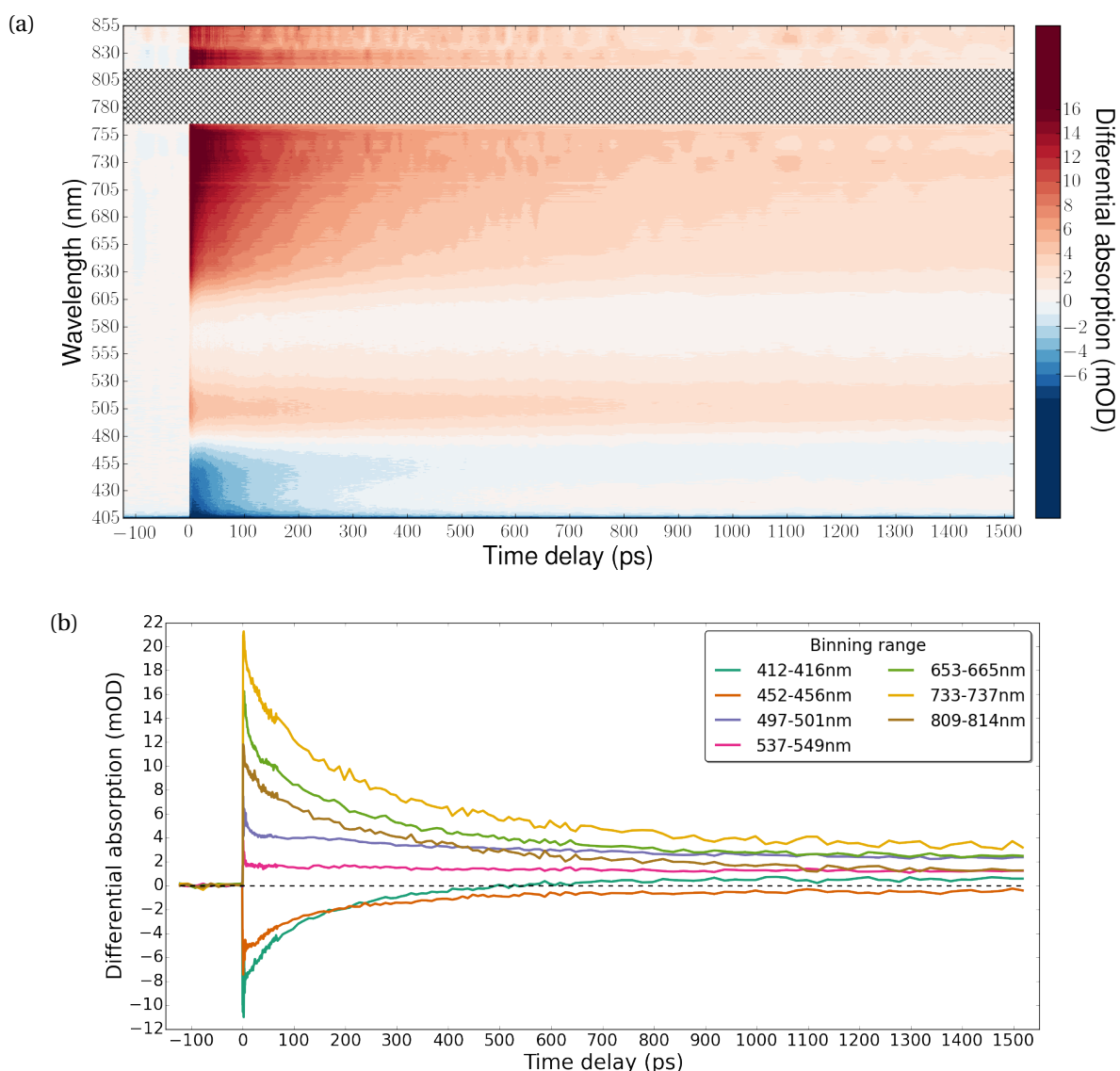
Figure 3.15: (a) Long-time dynamics recorded at 245 K across the detection wavelengths. (b) Select cuts along the specified wavelength regions. Each binned wavelength range contains very similar data.

Pico- to nanosecond kinetics at lower temperatures

The 2D plots of the datasets recorded at lower temperatures are presented in Appendix A (see Fig. A.4). The list of fitted time constants from global analysis is presented in Table 3.2. Among these, τ_3 shows a mostly steady increase as the temperature lowers, while τ_2 has a minimum at 135 K. Compared with Table 3.1, one notices that τ_3 and the unresolved (infinity) decay component in the previous table are the same as τ_1 and τ_2 in the present one, respectively.

Table 3.2: Time constants for long-time dynamics

Temperature (K)	τ_1 (ps)	τ_2 (ps)	τ_3 (ps)	τ_4 (ps)
80	5.4±0.2	98±4	470±20	5700±600
107.5	6.6±0.2	88±5	380±20	5700±500
135	5.0±0.2	55±3	340±10	5700±500
190	6.1±0.2	79±4	370±20	5700±900
217.5	7.4±0.3	81±5	330±20	5700±900
245	8.1±0.3	95±5	320±20	6000±1000

NB: The range in each time constant represents the 95% confidence interval from the fitting procedure.

3.2.7 Summary and discussions

The analysis given so far represents the status quo of the ongoing effort to understand the triiodide reaction in solid state via broadband pump-probe spectroscopy. The following list summarizes the observations from the TA data,

(1) Observation of a host of internal and external modes involved in the reaction. Among these, a few can be immediately assigned based on previous static and time-resolved studies in condensed phases. They are a libration mode and the symmetric stretching mode of ground-state I_3^- at 20 cm^{-1} and ~ 113 cm^{-1}, respectively, and the stretching mode of the photoproduct $I_2^{-\bullet}$ at ~ 106 cm^{-1}. The coherent oscillation of the libration mode lasts as long as ~ 12 ps at low temperatures. The fact that triiodide is a quasi-linear rotor with a large moment of inertia hasn't been fully

(a)

(b)

(c)

(d)
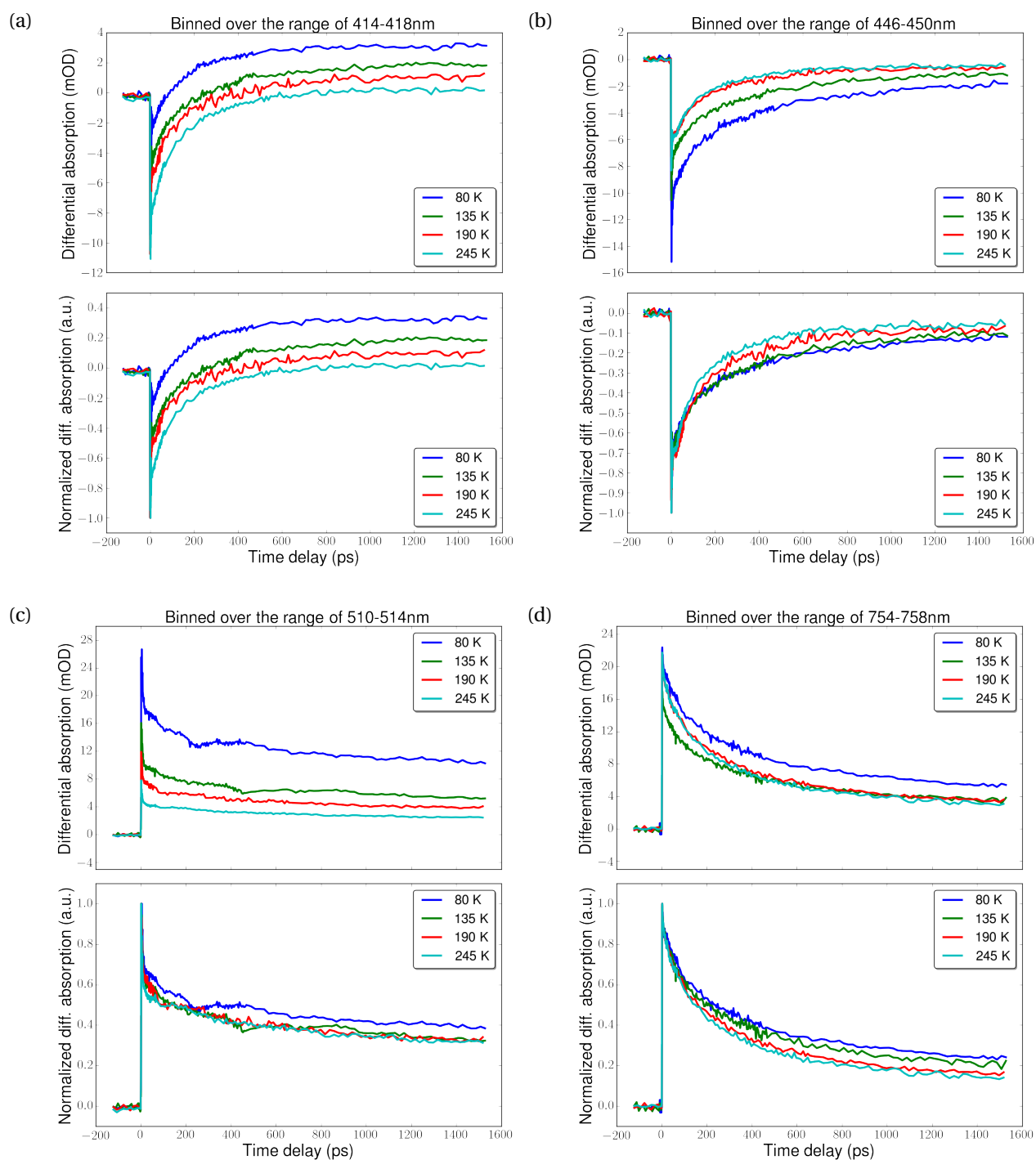
Figure 3.16: Comparison of the long-time dynamics at different sample temperatures. (a) shows the ground-state I_3^- recovery accelerated by an absorbing component and finally became an absorbing feature. In (b), the recovery proceeds without being overtaken by the absorbing feature. (c) In region B, a plateau-like feature appears between 50-400 ps. (d) A selected spectral region in the near-IR showing the reduction of $I_2^{-\bullet}$. Temperature-dependent rates are seen on the sub-ns timescale.
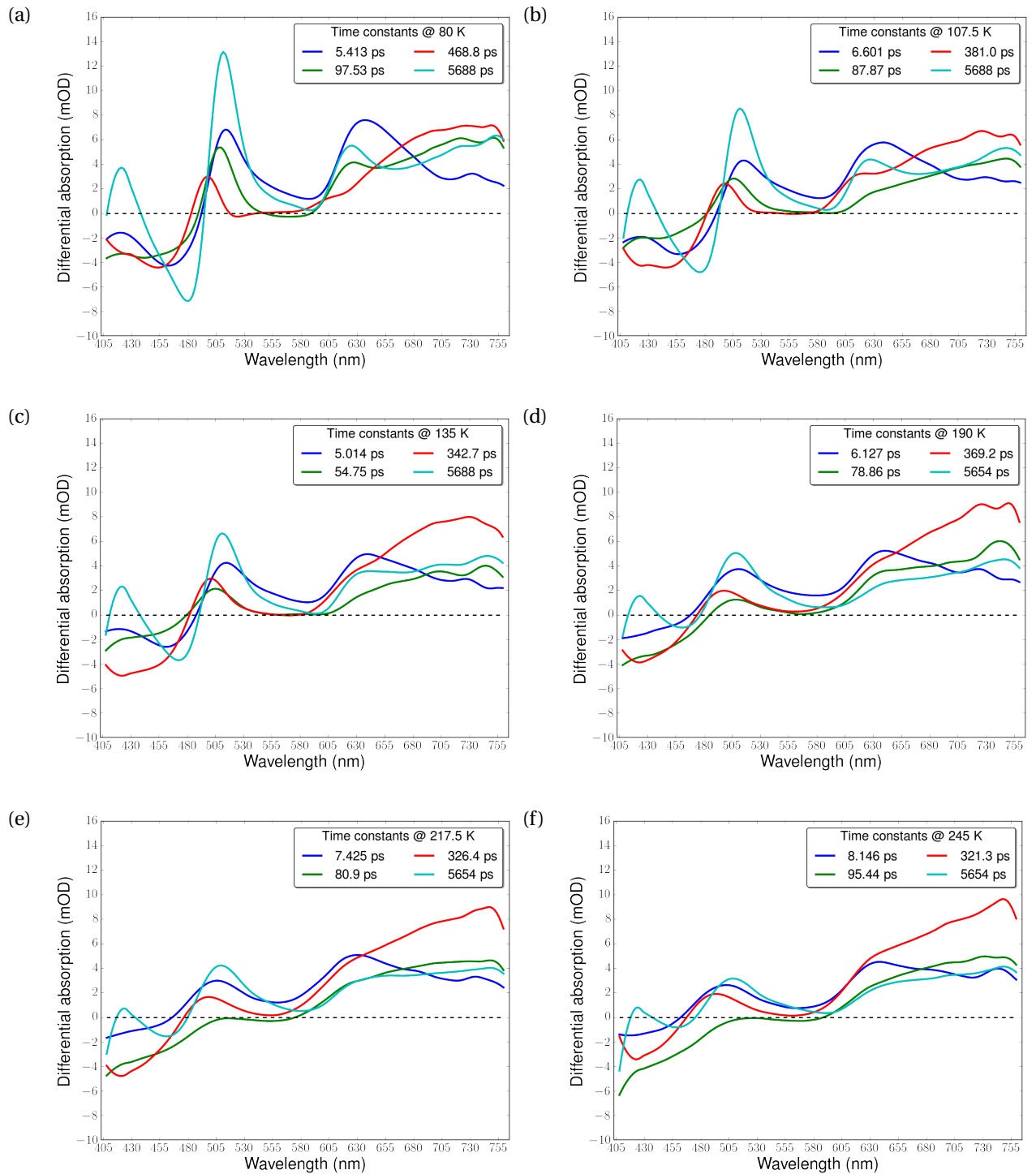
Figure 3.17: DAS obtained from global analysis of the long-time dynamics at different temperatures. The first two components strongly resemble those in Fig. 3.14 at the same temperature. The long-lived component there can now be resolved on the present time scale as τ_2.

63

appreciated before this experiment. The relevance of this libration mode to the solvent mode recently confirmed with similar frequency in [32] is unclear.

(2) Observation of coupling of internal and external modes through a chemical reaction, a unique phenomena of condensed phase reaction dynamics. There is strong evidence that these low-frequency lattice modes have a delayed appearance with respect to the molecular stretching modes in region A, B and D of the TA spectrum (see time-frequency diagrams in Fig. 3.10 and Fig. 3.11.). Therefore it is more likely that they are at least partly initiated through coupling to the PES of the triiodide reaction from bending or recoiling motions rather than through impulsive-Raman-type excitation.

Recorded TBAT Raman modes

Sugai & Saito	Zambounis et al	Mode assignment	Spotted in TA?
14	--		
22	19-22	Libration	Y
31	30-32	Libration	Y
37	--		Y
47	44	Bending	Y
54	--		
66	--		
79	--		
100	--		
108	107-108	SS (straight)	Y
115	114-115	SS (bent)	Y
125	125	AS (straight)	
--	140-144	AS (bent)	

Frequencies in different regions of TA spectrum

Frequency (cm^{-1})	A	B	C	D	E	F
10	•	•	•	•		
16				•	•	
20	•	•	•	•		
30				•		
35	•	•	•			
45				•		
70			•			
90				•	•	
106		•		•	•	•
113	•	•			•	
122			•			

Figure 3.18: The left table includes Raman frequencies compiled from Sugai & Saito [112] and Zambounis et al [113]. A full list of frequencies with important contributions to different regions in the TA spectrum is shown in the right table. The symbol "•" in the column indicates that the mode is present in the spectral region.

(3) The decay associated spectra reveal an initial inverted distribution of population in the reactant's and photoproduct's absorption bands, followed by the growth of

photoproducts and, consequently, the multiphased recombination that gradually restore the population balance. The slow recovery persists well into the nanoseconds, implying a diffusion-limited process in solid state [115] that proceeds after the true geminate recombination is completed.

(4) Identification of a possible alternative reaction channel $2I_3^- \xrightarrow{h\nu} I_2^{-\bullet} + I_4^{-\bullet}$ (or simply $I^\bullet + I_3^- \rightarrow I_4^{-\bullet}$ with $I^\bullet$ coming from the dissociation of I_3^-) on the few-ps timescale through spectral features seen in the transient absorption spectrum and the DAS obtained from global analysis.

(5) Temperature-dependent shift of absorption bands is observed in most regions of the spectral window. This is especially so in the region < 530 nm. The possible $I_4^{-\bullet}$ absorption band around between 605-680 nm is incorporated into the near-IR band of $I_2^{-\bullet}$ at higher temperatures. In general, a blueshift is observed for dynamical features (i.e. bleaching or growing bands in TA spectra) captured in transient absorption spectra. In addition, an increasing temperature also markedly reduces the dephasing time of the coherent oscillations as shown in Fig. 3.13a.

The frequencies compiled from static Raman measurements on solid state TBAT samples are compared with the frequencies observed in the TA experiment in Fig. 3.18, including the known assignments to atomic motions. In general, for TBAT with two distinguishable and quasilinear I_3^- chains, there are four vibrational normal modes (including two non-degenerate bending modes) and two libration modes for each chain. With the three translation modes included, the total number of distinct modes involving each distinct I_3^- chain is 4+2+3=9, and 18 in total for the two independent chains in a unit cell. They can be obtained from phonon mode calculation using CASTEP (performed by Prof. Carole Morrison) and are listed in Table E.3 of Appendix E. Taking into account the difficulty of CW Raman spectroscopy in observing low-frequency modes that are close to the Rayleigh line, this number matches well with the documented number of modes shown in Fig. 3.18. The modes not currently assigned are either from unidentified lattice modes, or modes specific to the photoproduct $I_4^{-\bullet}$.

The documented $I_2^{-\bullet}$ stretching mode has very similar frequency to the symmetric stretching mode of the straight I_3^- chain in TBAT, which makes distinguishing the two modes in frequency analysis difficult, but the location that the mode appears (i.e. in the bleaching or growing band) can help pin down the origin.

It is worth noting here that some of the observations made here are in stark contrast to Poulin & Nelson's work [25, 26], which described a very fast (< 3 ps) full recovery of the reaction when triiodide ions were excited to the D band with 300 nm pump pulses. One immediate cause for the discrepancies could be that the different excitation wavelength will initiate distinct dynamics in the D-band excited state compared with excitation to the C band, as in the present experiment, due to different branching ratios. This is at least true in gas phase studies [17, 18] and a former study in solution using the isosbestic point as a monitor of the branching ratio [16]. The more practical reason may be that the experimental conditions between their and the present experiments are very different (refer to Section 3.1.2 for a summary of their work). With a boiling point of a mere 70 °C (Sigma-Aldrich), the TBAT sample can easily melt in single-shot room-temperature experiments caused by laser heating. And moving to different spots on a solution-grown sample, which usually has inhomogeneous surface quality, can produce dissimilar signals due to various amounts of scattering [25]. This has been seen in samples with poor surface quality in the present experiments. These samples distort the transmitted probe beam's spatial profile and a constant scattering signature appears on the short-wavelength side of the TA spectrum. The samples with good surface quality show TA signals presented in sections of 3.2.3-3.2.6 and these results are reproducible. Additionally, the thick samples described in Poulin's thesis [25] can also, to a great extent, create artefacts of the observed dynamics due to lateral averaging over the thickness of the sample.

3.3 Ultrafast electron diffraction studies on solid state TBAT

3.3.1 Electron diffraction setup

An ultrafast electron diffractometer (UED machine) visualized in Fig. 3.20a is the setting of an optical-pump-electron-probe experiment. The optical pump pulse at 400 nm and the photoelectron pump pulse at 266 nm were derived via harmonic generation from the previously mentioned ultrafast laser system (Coherent Elite USP). These two beams were routed into the vacuum chamber using two sets of periscopes. After photoemission from the Au photocathode, the photoelectrons gained energy when traversing a voltage difference of 120 kV across 10.5 mm to the anode, where the beam was intercepted at the inter-chamber wall by an aperture with a diameter of ~ 150 μm. The electron beam and the optical pump beam met at the sample position in the back-illumination geometry. Their beam sizes there were about 550 μm and 300 μm at FWHM, respectively. After passing through the sample the electron beam was focused by a magnetic lens onto the detector to obtain a sharp diffraction pattern without transforming into the real space, as was first demonstrated in 1931 [116]. Right before the detector, the electrons were converted to visible photons using a phosphor plate. The photons were then channeled to a CCD camera (Princeton Instruments Quad-RO: 4320) using a fiber taper with hexagonal edges. A stack of Peltier thermo-electric modules was used to lower and maintain the sample temperature in order to avoid vacuum damage to the sample (stability test of sample see Section 3.3.3). The stack was glued between two Cu blocks, which connected to the manipulator arm on one side and the sample holder on the other. Running at the optimal current, the Peltier stack maintained the sample temperature at ~ 275 K. Temperature was measured using the four-wire method with a Pt resistor. During the measurements, cold nitrogen gas was used to cool the sample further down to 245 K and a feedback controller with a heater was used to maintain the sample temperature to a precision

67

of ~ 0.1 K.

3.3.2 Sample preparation and characterization

Samples for the electron diffraction and optical pump-probe experiments were cut using a diamond knife (Micro Star Technologies, MT series, 3.0 mm blade) from bulk crystal using an ultramicrotome. In electron diffraction, the samples had a thickness of ~ 120 nm, and they were placed on standard Cu TEM meshes (Plano GmbH). The standard cutting procedures followed largely the accounts for TEM sample preparation as in [117]. Water was used to fill the boat attached to the diamond knife (therefore the name wet ultramicrotomy) because of water's high surface tension and the very low solubility of TBAT in it. Wet cutting was always preferred over the dry version. A critical issue in ultramicrotomy is on how to minimize the compression of thin sample slices, or to reduce lesion-induced surface roughness and to preserve structural integrity during cutting and transfer to the mesh. In the worst case, the sample slice wrinkles up and becomes unusable. Five points (the *tricks*) were found to be of great importance for this reason. They are summarized in the following and can be immediately applied to preparing other soft organic samples using wet ultramicrotomy.

(1) The **water surface** in the boat should form a convex crescent that descends from the edge of the knife. This ensures that the initial section of the slice can slide down the liquid surface as it's being cut from the bulk to make room for the section that comes after. With other kinds of water surfaces (i.e. flat or concave) the sample slice easily becomes crumbled during cutting. This is of paramount importance to soft organic materials.

(2) **Slow cutting** was found to reduce the compression. A moderate speed of 1mm/min was used when cutting electron diffraction samples. Pausing the knife-bearing mechanical arm in between a cutting cycle was more helpful in this respect than running the knife continuously.

(3) The cut slices should be **harvested one at a time**. In this way, there is less chance

68

(a)

(b)

(c)
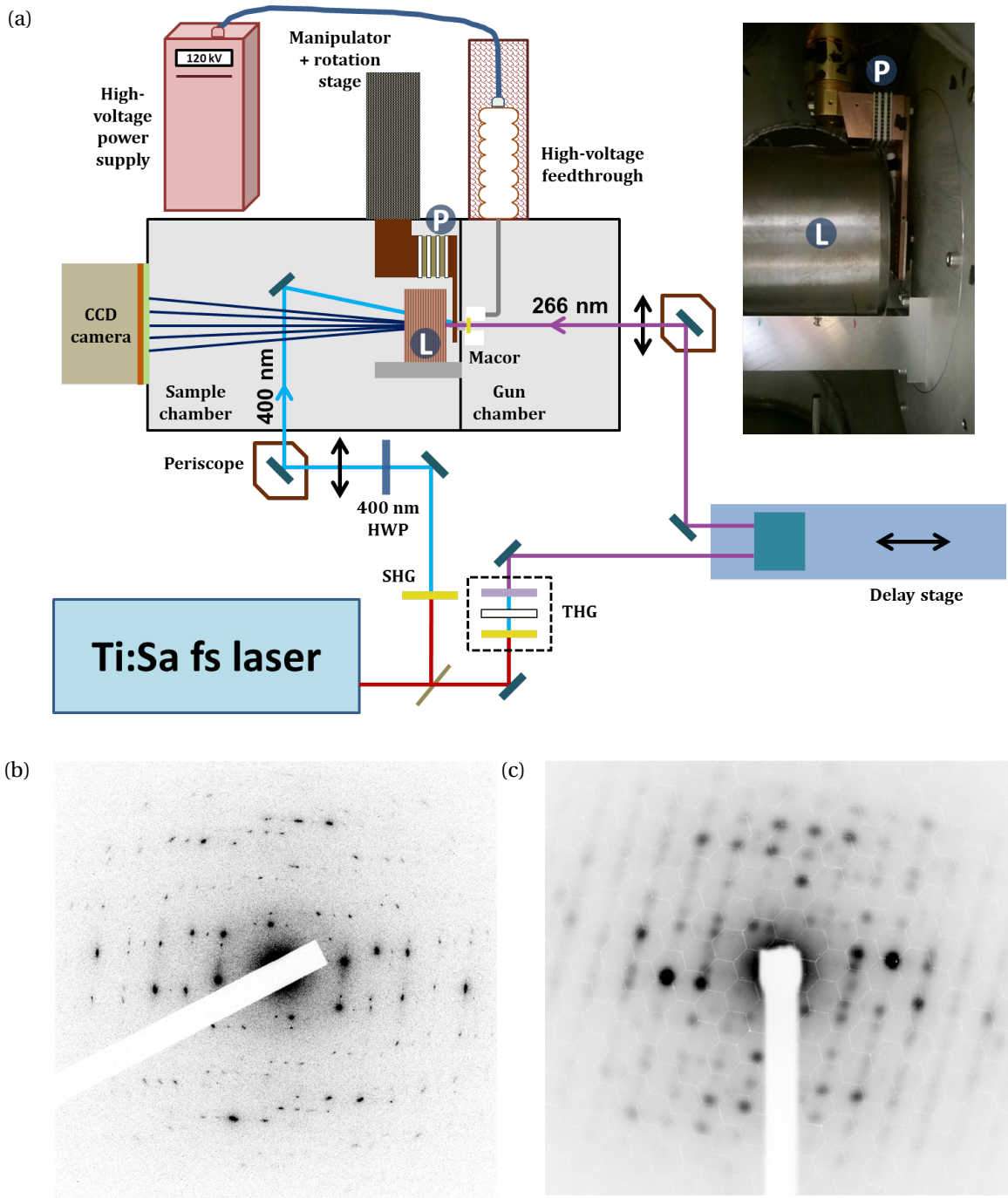
Figure 3.20: (a) Schematic of the UED machine. The inset photo shows the picture of the Peltier stack (P) and the magnetic lens (L). The Peltier stack is sandwiched between two Cu blocks that connect to the manipulator arm and the sample holder on either side. The Macor block holds the Au photocathode in place. Photoelectrons released by the 266 nm photons from Au are accelerated by the gradient between the electrodes before reaching and diffracting off the sample. The 120 nm-thick samples are prepared by wet ultramicrotomy and diffraction patterns obtained from (b) a 200 kV TEM (JEOL 2100) and (c) the UED machine are compared here.

that the slices that come after can bump into those that are produced before, which, for soft organic samples, can cause cracking up of slices into smaller pieces.
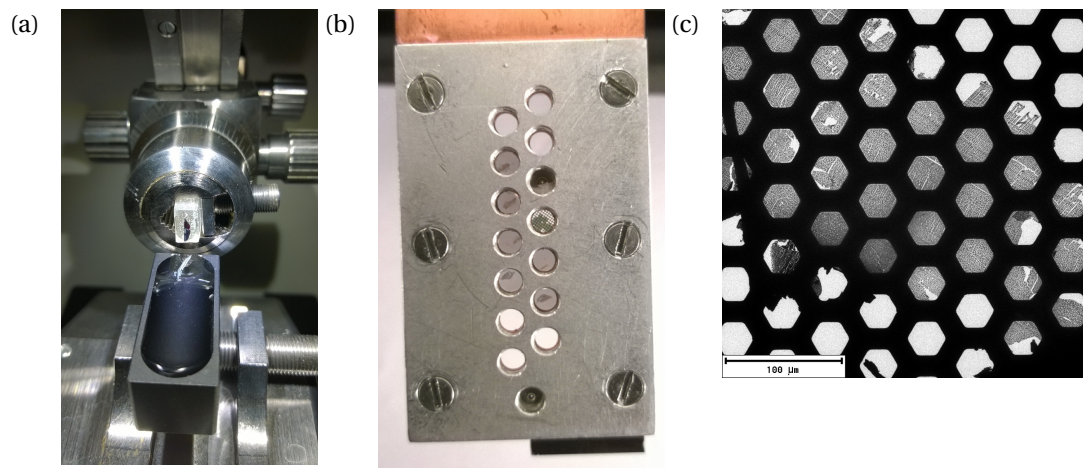
Figure 3.19: (a) TBAT sample preparation using an ultramicrotome: the thin slice floating on water was cut from the bulk (black and glued to the opaque resin substrate) clamped in the chuck of the ultramicrotome. (b) The mesh-supported thin samples were mounted on the Cu sample holder before transferring to the vacuum chamber. The direction of the samples were rotated manually such that the long axis is close to parallel to each other. This ensured that the optimal pump polarization for the samples can be regarded as the same. (c) Wide-field real-space TEM (JEOL-2100) image of TBAT sample obtained using 200 keV electrons.

(4) Harvesting the slices **directly using the TEM mesh** is preferred when preparing diffraction samples than using a pick-up loop. This reduces the number of contacts with the sample. In either scenario, retrieving the sample from below the sample proved to cause less damage to sample integrity than from the top.

(5) **Transfer** should be made **to sufficiently wet surfaces**, where the samples are left for drying. This greatly reduces the shock wave caused by the breaking-up of water droplets on the mesh or pick-up loop when they get absorbed by the blotting medium. For electron diffraction samples, a fully drenched piece of tissue paper suffices. For optical pump-probe samples to be placed on a (slippery) glass substrate, a wet blotting paper should be within reach of the pick-up loop during transfer to gently soak up the water and keep the sample in place.

After preparation, the samples were preserved in a fridge at around 4 °C until experimental use. This has been found to be especially important for fragile organic samples like TBAT, because cooling greatly reduces the potential damage from oxidation or sublimation under ambient conditions, which, from practical experience, happens at a faster rate for thin samples than the bulk crystals.
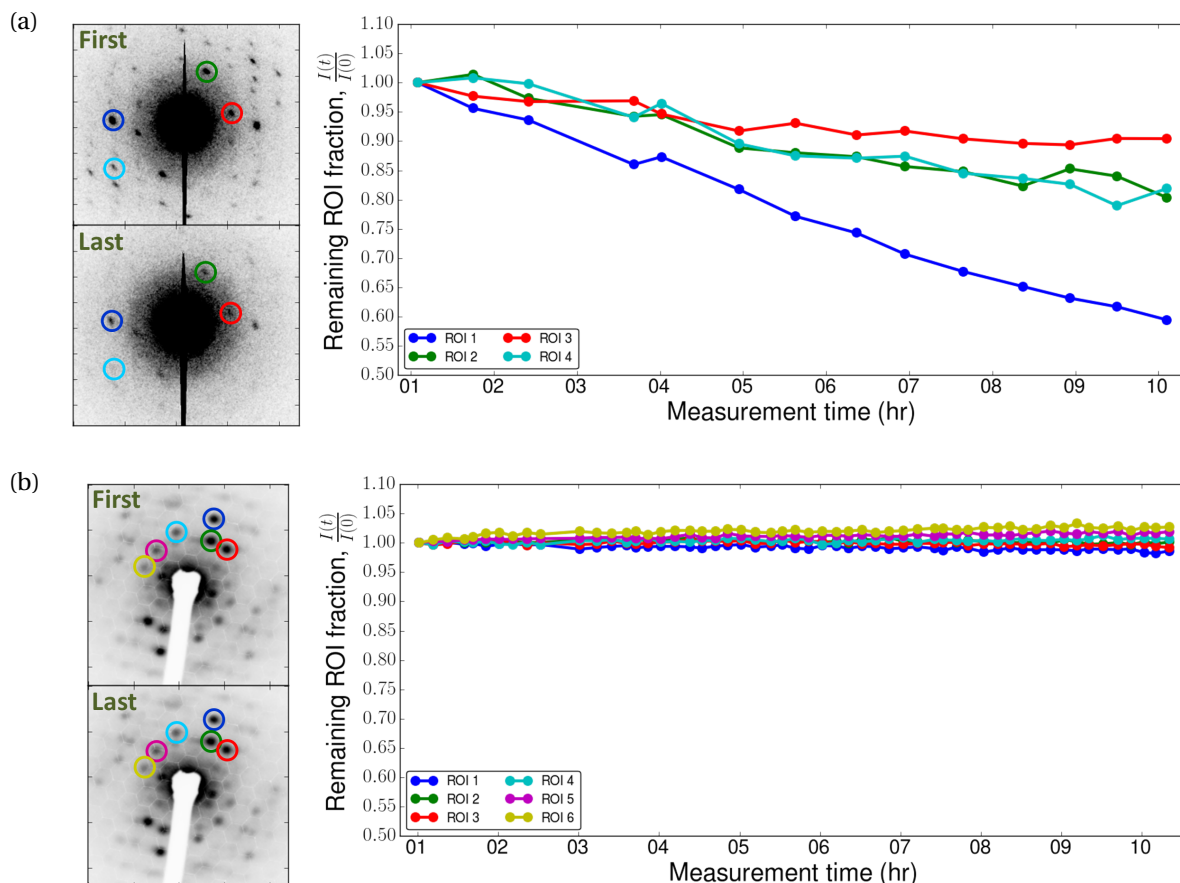
Figure 3.21: (a) Vacuum decay of sample without temperature stabilization, measured using the RF gun UED machine at University of Toronto. (b) The sample is resistant to vacuum with temperature stabilization using a Peltier stack to lower the temperature to ~ 275 K. The small deviations are mostly due to thermal expansion of sample holder as a result of the accumulated heat radiation from the nearby magnetic lens as well as electron beam shift over time as a result of laser beam pointing instability. This measurement was conducted in Hamburg using a DC gun UED machine. In the formula for the remaining ROI fraction, I(t) and I(0) are integrated ROI intensities normalized by the electron number of the corresponding image, $t = 0$ is the start of the static diffraction measurement.

71

3.3.3 Sample stability under ultrahigh vacuum and photoexcitation

The ultrahigh vacuum (UHV) condition (10^{-7}-10^{-8} mbar) that the sample chamber needs to stay in is an adversarial condition for fragile organic samples with hundred-nanometer thickness. This is the main reason behind such stability tests, which are usually performed at the very beginning of a project. Unfortunately, TBAT at 120 nm or less is not stable in UHV. The quality of sample drastically degrades over the course of several hours, which eventually leads to complete amorphization within a day, as is evident from the diffraction pattern. Bringing the sample temperature down to ~ 275 K with the Peltier stack, at only a mere ~ 23 K from room temperature in the lab, was found to maintain the sample freshness over the course of weeks at the very least. The results from these two scenarios (without and with temperature stabilization) are compared in Fig. 3.21.
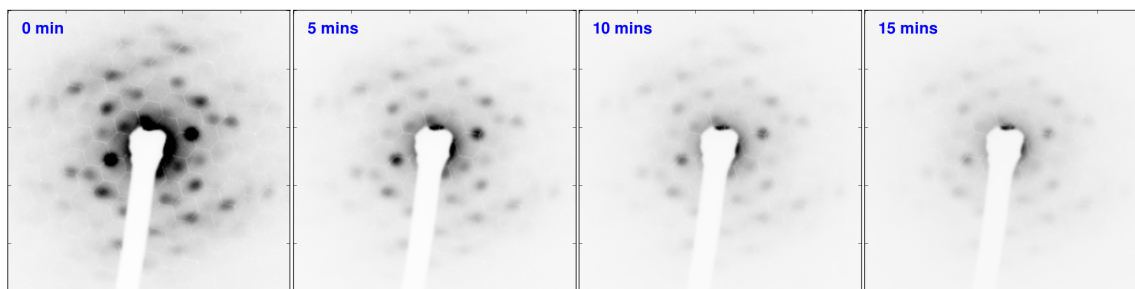
Figure 3.22: A sequence of diffraction pattern of TBAT sample at 275 K (temperature stabilized using the Peltier stack) illuminated with focused 400 nm optical pump running at 1 kHz. The time on the upper left corner of each image denotes the period of illumination. Each image is normalized with respect to the total electron number count after background subtraction. The maximum color scale for the 0-min image is 3, 6, and 9 times that of the 5-min, 10-min, and 15-min image, respectively, for the purpose of viewing. This illustrates the drastic optical damage the sample receives as a consequence of the slow recovery and irreversibility of the chemical reaction.

In addition to vacuum stability, the sample's optical stability under 400 nm-pump illumination was tested from 1 kHz to 100 Hz. The results for 1 kHz are shown in Fig. 3.22. Incipient optical damage appears visibly a few minutes after the start of illumination. This is, however, slower than that observed in the single-shot experiments [25],

due mainly to the effect of temperature stabilization. Optical damage disrupts and destroys the crystal structure in real space and therefore a drop of diffraction peak intensity is immediately seen in Fourier space as a sign of the loss of crystallinity. Over time, the diffraction pattern slowly develops incomplete rings at low diffraction order (k-space location close to the beam center), signifying the degradation of crystallinity.

3.3.4   Determination of sample orientation and indexing

Because of the sample preparation procedure and the uncertainty introduced during sample mounting in the UED machine, its orientation needs to be determined prior to data analysis. In practice, measuring a series of static diffraction patterns at slightly different incident electron beam angles can provide sufficient data for orientation fitting. The diffraction pattern was recorded after rotating the manipulator arm around y axis (perpendicular to electron beam direction along z) and re-optimizing the positions at each angle to maximize the diffraction intensity. The range from 87° to 91° was achievable[6] with 1° step manual adjustment (see Fig. B.2). Peak-finding was automated by first sifting through local maxima on different areas of the image and then fitting the area around each maxima to a 2D Gaussian function to extract the peak position. A detailed description of the algorithm is provided in Appendix D. The program is efficient in picking out isolated diffraction peaks rather than the occasional hot pixels appearing on the detector as well as avoiding the edges from the fiber taper, but it has issues distinguishing highly overlapping peaks, which are affected by the unit cell size of the sample as well as the spatial coherence of the electron beam.

The rotation series yielded a library of the peak parameters (position and intensity) at the measured beam angles. The orientation was found by comparing simulated peak parameters with those obtained from experiments using a minimization scheme. However, due to the (very) limited number of observed peaks, a total of 430 in five images, multiple solutions were found. To narrow down the search, the diffraction

---

[6]For a reference, during time-resolved measurements, the goniometer was set at 90°.

(a)

(b)
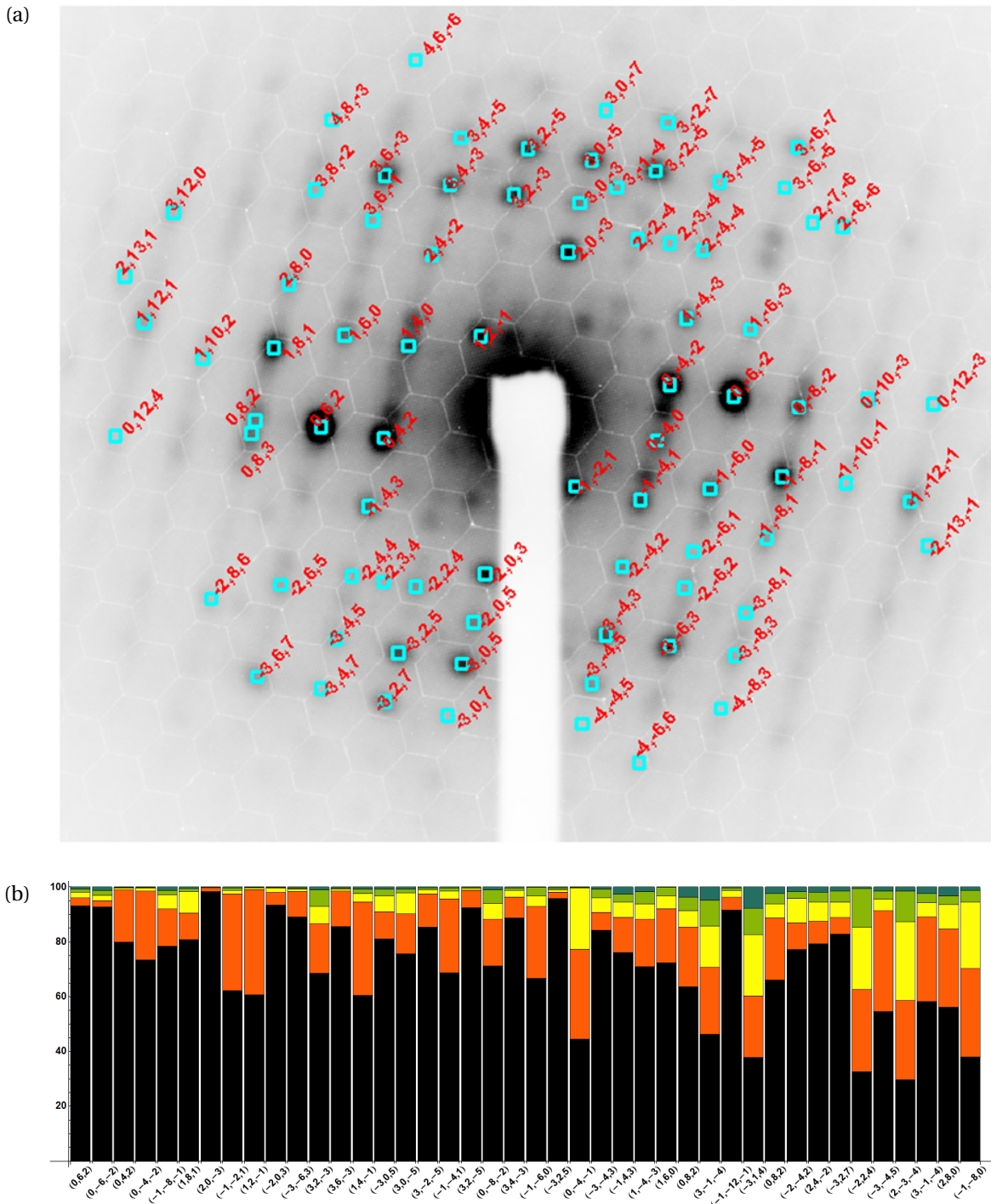
Figure 3.23: (a) Static diffraction pattern with Miller indices labeled on a number of peaks. (b) Bragg peak intensity contribution (in percentage and indicated by different colors) to some of the most intense diffraction peaks in (a). The indices on the x axis represent the principal component of the diffraction spot. The same indices are also used to label (a).

patterns in the whole rotation series (see Fig. B.2 in Appendix B) were simulated and compared directly with the 2D experimental data. This part of the orientation finding was done by Dr. Alexander Marx. From his computer routines, the electron beam direction in real space fractional coordinates (of the crystallographic system) was determined to be [-7.00, 1.26, -4.29]. The angles that the electron beam formed with the principal axes in the real and reciprocal spaces of TBAT are shown in Table 3.3.

Table 3.3: List of angles formed between the electron beam and a principal axis in real (a,b,c) or reciprocal (a*,b*,c*) space

a (°)	b (°)	c (°)	a* (°)	b* (°)	c* (°)
140.40	90.73	142.86	126.77	79.48	128.39

Since the I_3^- chains lie along or very close to the crystallographic a axis (see Fig. 3.1), a 140.40° angle means that the beam will diffract off the chains at an oblique angle. This slanted view means that most (if not all) types of motion this quasilinear ion can exhibit can be captured by the electrons in time-resolved diffraction data. A fully indexed diffraction pattern is presented in Fig. 3.23.

3.3.5 Data analysis for time-resolved measurements

To construct the time-resolved traces from a sequence of diffraction patterns, the relative change (in percentage) of a diffraction spot $\eta(t)$ at time t is calculated using the following expression,

$$\eta(t) = \frac{\left[I_{\mathrm{pon}}(t) - I_{\mathrm{pon}}^{\mathrm{bkgd}}\right] - \left[I_{\mathrm{poff}}(t) - I_{\mathrm{poff}}^{\mathrm{bkgd}}\right]}{I_{\mathrm{poff}}(t) - I_{\mathrm{poff}}^{\mathrm{bkgd}}}\% \tag{3.3}$$

where I_{pon} and I_{poff} are the integrated intensities of the diffraction spot in the pump-on and pump-off image, respectively. $I_{\mathrm{pon}}^{\mathrm{bkgd}}$ and $I_{\mathrm{poff}}^{\mathrm{bkgd}}$ are the corresponding integrated detector background of the diffraction spot region. During one day's measurements, these backgrounds are taken to be constants provided excitation conditions stay the same. When no significant pump scattering is seen (depending on sample surface

quality and the pump wavelength), $I_{\mathrm{pon}}^{\mathrm{bkgd}} \approx I_{\mathrm{poff}}^{\mathrm{bkgd}} = I_{\mathrm{bkgd}}$, and the above expression can be reduced to,

$$\eta(t) = \frac{I_{\mathrm{pon}}(t) - I_{\mathrm{poff}}(t)}{I_{\mathrm{poff}}(t) - I_{\mathrm{bkgd}}} \% \tag{3.4}$$

This is true with 400 nm pulses as the optical pump. Shot noise is a significant issue in analysis of electron diffraction data. For the DC electron gun, reducing the electron number to shrink the pulse duration can raise the role shot noise plays in the SNR. Therefore the average of pump-off images of three nearby time delays were used per time point. This is valid since the sample quality only decays slowly on a long time scale. The pump-on pattern is subject to an outlier rejection algorithm before inserting into Eq. 3.3 to calculate the relative change. More details of the outlier rejection scheme used is described in Appendix D.

For combining different scans, the decay of the relative change (discussed in section 3.3.7) should be taken into account. The average value of the relative changes after time zero are used to calculate the scaling factors for each diffraction peak from scan to scan. The overall standard deviation of the mean at each time delay, $\overline{\sigma(t)}$, is obtained by combining that from each scan, $\overline{\sigma_i(t)}$, in quadrature using the formula,

$$\overline{\sigma(t)} = \frac{1}{m}\sqrt{\sum_{i=1}^{m} \frac{\sigma_i(t)^2}{N_i}} = \frac{1}{m}\sqrt{\sum_{i=1}^{m} \overline{\sigma_i(t)}^2} \tag{3.5}$$

where m is the number of scans to be averaged and N_i is the number of repeated frames at a fixed time delay in a single scan. The symbol $\sigma_i(t)$ is the standard deviation of the set of measurements at a particular time delay t in one scan.

3.3.6 Polarization dependence

Similar to optical pump-probe experiment, the polarization dependence was measured by fixing the pump-probe time delay at $\sim$ 1 ps while recording the diffraction

(a)

(b)

(c)
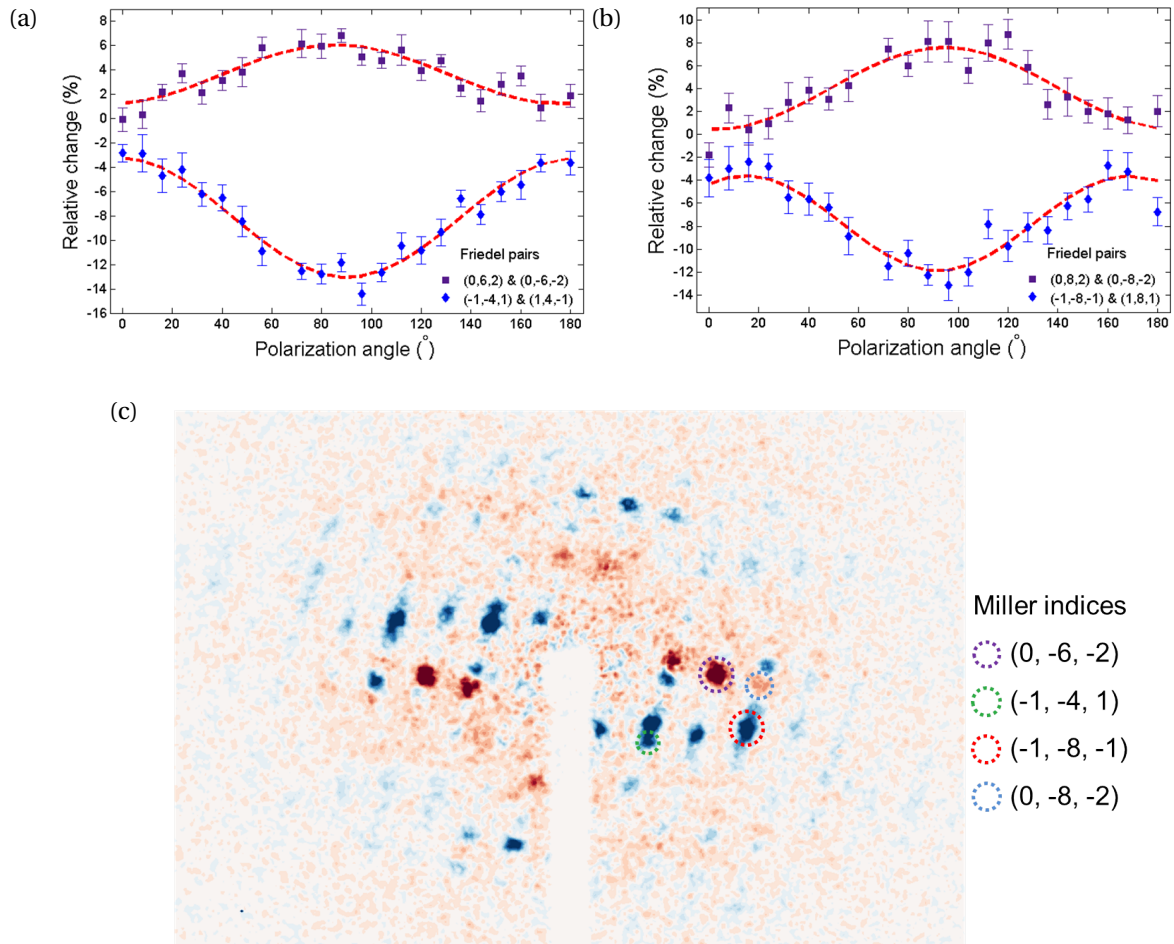
Figure 3.24: (a-b) Polarization dependence of the relative intensity changes of four Friedel pairs with the pump-probe time delay fixed at 1 ps. The sinusoidal fits were included to reflect the dependence. The error bars in both plots represent the standard deviation of the mean. (c) Difference image at a pump-probe time delay of 1 ps, showing the pump-induced changes to the diffraction peaks (red = positive change, blue = negative change). The locations of one spot in each Friedel pair named in (a-b) are labeled on the image (c).

pattern differences with different excitation polarizations. The changes of the diffraction peaks were extracted and presented in Fig. 3.24a-b. The measurements was carried out with ∼ 6 fC electron bunches to improve SNR and reduce the number of pump shots needed for a single time delay. The relative changes can be fit straightforwardly to a sinusoidal (or cosine squared) curve, in agreement with a Malus-type dependence. This is the result of the linear arrangement of triiodide inside the crys-

tal, which maintains a well-defined transition dipole direction, now reflected in the Fourier space. The bigger the pump-induced intensity change a spot had, the stronger the polarization contrast. In addition, those spots without time-resolved dynamics didn't have an obvious polarization dependence.

3.3.7   Fluence dependence and sample reversibility test
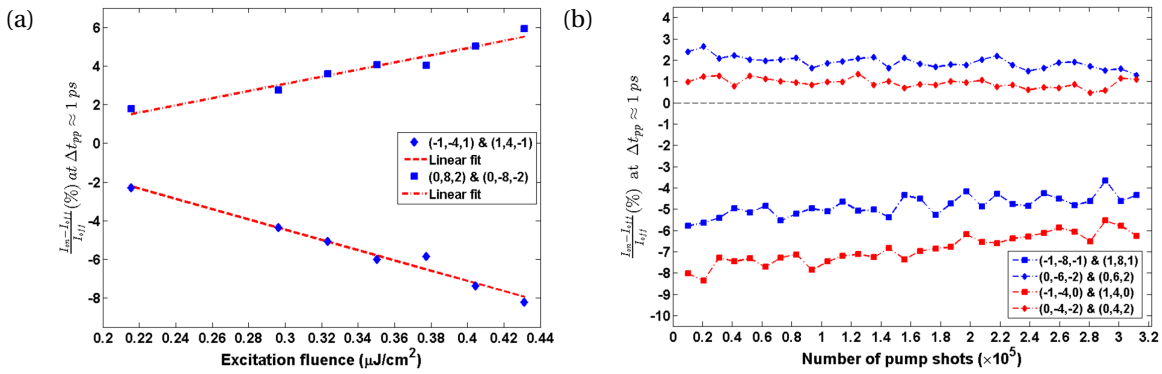
Figure 3.25: (a) Fluence dependence of two selected Friedel pairs plotted along with linear fits. (b) Decay of relative change averaged over selected Friedel pairs. In both sets of measurements the pump-probe time delays were fixed at ~ 1 ps.

The sample response was measured at different excitation fluences to characterize the excitation regime. Due to the limited number of high-quality samples, the fluence of up to ~ 0.43 mJ/cm^2 was used. At each fluence the same set of diffraction spots were analyzed to obtain the relative changes. A linear dependence is seen in the data presented in Fig. 3.25a.

The sample reversibility was measured at a fixed time delay after time zero, the same as the procedure used in optical pump-probe experiment (Section 3.2.4). In Fig. 3.25b, the relative changes of a number of diffraction spots are plotted against the number of 400 nm pump shots. This measurement was carried out with 6 fC electron bunches and a pump repetition rate of 125 Hz. The pump pulse energy was set at 1.35 uJ, corresponding to a fluence of 0.34 mJ/cm^2 (or 6.85×10^{14} photons/cm^2). These parameters are in typical settings of UED experiments described later and the TAS experiments

described earlier (see Fig. 3.8)[7]. It is evident that the sample quality degrades under such conditions, but at a slow rate so that a reasonable number of time delays can be scanned and repeated at one fixed sample position.

3.3.8 Picosecond dynamics
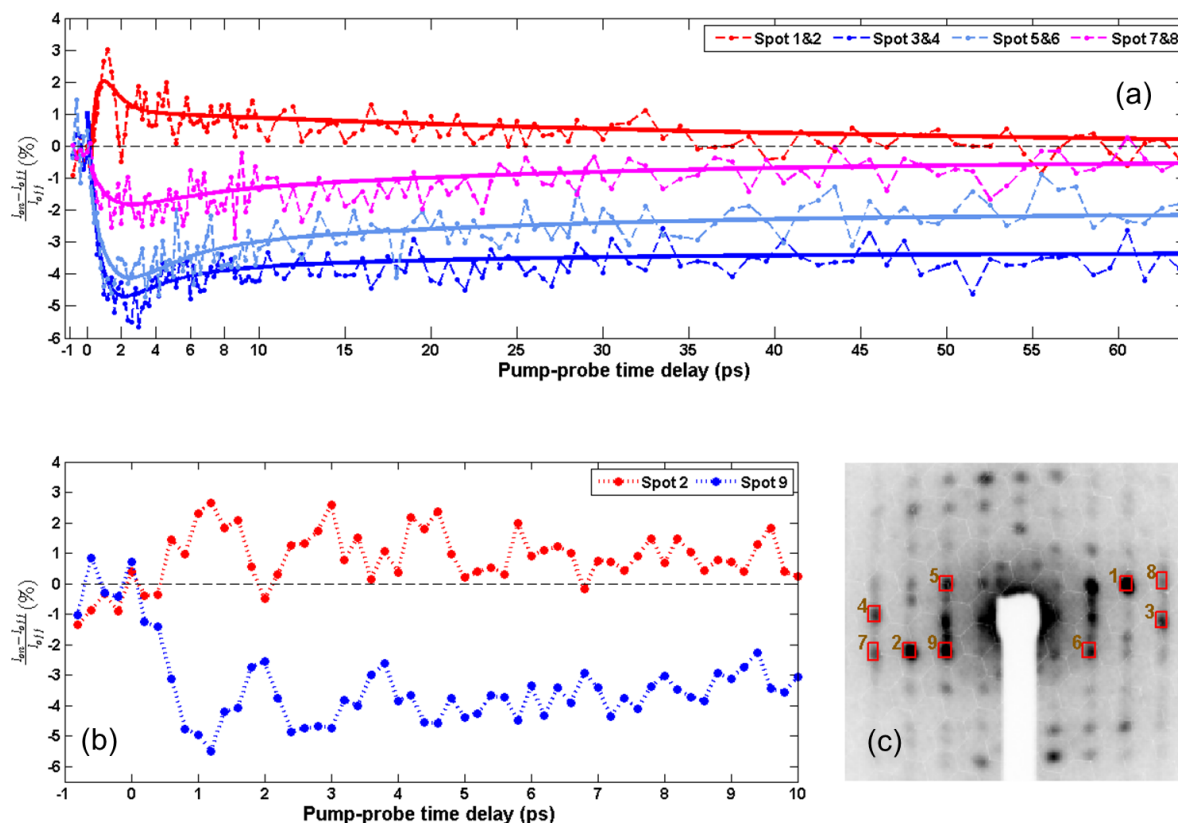
Figure 3.26: (a) Long-time dynamics of some characteristic Bragg peaks. (b) Zoomed-in view the initial coherent oscillation (c) Static diffraction pattern with locations of plotted spots.

Measurements were performed at 245 K from -1 ps to 65 ps with ~ 6 fC electron pulses. A combination of 200 fs, 500 fs and 1 ps time steps were used to cover the whole time span. The results are presented in Fig. 3.26. On this time scale three major types of

---

[7]The major difference in measurement conditions between the TAS and the UED experiments is the sample thickness. In TAS measurements, the sample (~ 1 μm) needs to be thick enough to have OD ~ 1, while in the UED experiment the sample (120 nm) needs to be thin enough to allow electron to transmit and minimize the effects of multiple scattering. Besides, the vacuum pressure in the UED experiment is three orders of magnitude lower than that in the TAS experiment.

dynamics are seen among 48 analyzed diffraction spots.
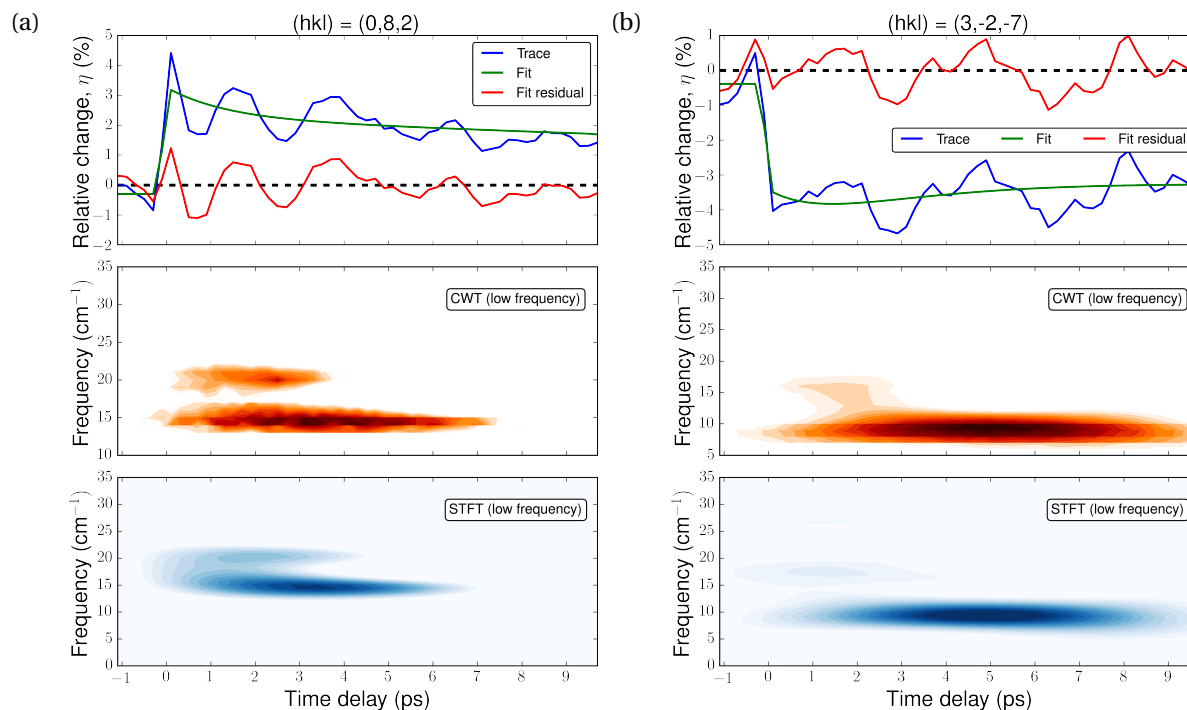
Figure 3.27: Dynamics of selected diffraction spots measured from -1 ps to 10 ps with 200 fs time steps and 6 fC electron bunch charge. The data were smoothed using a Savitzky-Golay filter before the frequency analysis. Note the difference in the frequency scales between the two WT plots. In STFT, the same Tukey window was used for analyzing both.

(1) **Libration sensitive spots:** These spots are all located near the rectangular region on either side of the beam center, as seen in Fig. 3.26. Their time-resolved intensity changes are modulated by the 16 or 20 cm^{-1} oscillations in addition to a non-zero offset resulted from atomic displacements initiated by the reaction. The Friedel pairs with the lowest indices to exhibit such behavior are (1,4,-1)/(-1,-4,1) and (0,6,2)/(0,-6,-2). Some of the spots with closely related indices show changes with opposite signs. These peaks are mostly located in the 3 or 9 o'clock direction in the indexed pattern in Fig. 3.23a.

(2) **Translation sensitive spots:** A 10 cm^{-1} mode (see Fig. B.4 of Appendix B) was found

in the relative intensity change of (3,-2,-7), (2,0,-3) and surrounding peaks (about 1 o'clock direction in Fig. 3.23a). It persists for about three full oscillations and its origin is most likely the translational motion of I_3^- chains.

(3) **Weak growth:** Diffraction spots of this type don't show oscillatory dynamics on few-ps time scale, but develop a slow growth signature from tens of ps onwards. Among the 48 spots analyzed, only 4 were found to exhibit such behavior. These 2 Friedel pairs have the Miller indices (0,4,2)/(0,-4,-2) and (0,4,0)/(0,-4,0), which are low-index peaks for TBAT.

3.3.9 Femtosecond dynamics
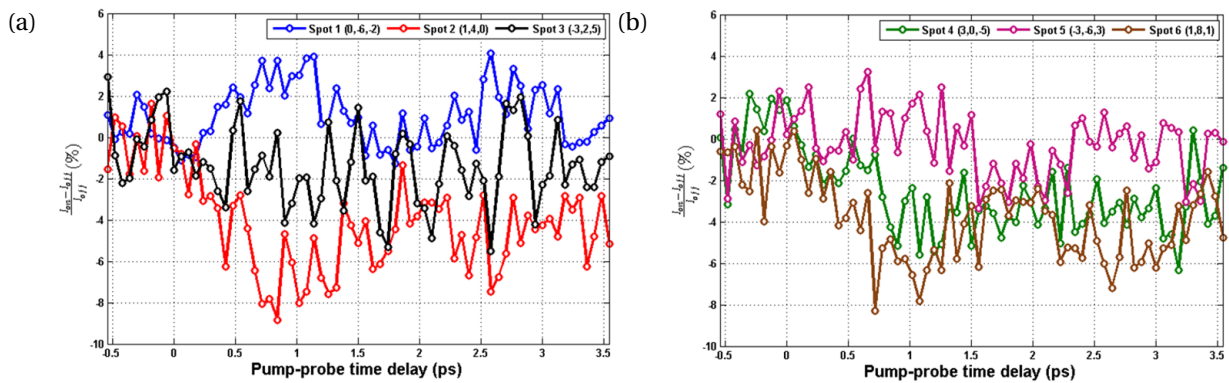
Figure 3.28: Dynamics of selected diffraction spots measured from -0.5 ps to 3.5 ps with 60 fs time steps and 0.7 fC electron bunch charge.

Measurements at short time delays were repeatedly made from about -0.5 ps to 3.5 ps with a time step of 60 fs. This time range corresponds to about two periods of the 16 or 20 cm^{-1} (18 cm^{-1} on average) libration mode, during which, according to the optical pump-probe data presented earlier in this chapter, most of the high frequency internal and external modes are not fully dephased. For these measurements, the electron bunch charge is lowered to ~ 0.7 fC to improve the time resolution of the probe. In this way, it is possible to resolve modes with a period down to about 300 fs, which suffices for discerning the stretching modes of I_3^- and $I_2^{-\bullet}$, given good SNR. The selected time-resolved traces for the short-time dynamics are shown in Fig. 3.28.

Chapter 3. Combining broadband transient absorption spectroscopy with ultrafast electron diffraction

In addition to seeing the very pronounced libration mode, coherent oscillations at
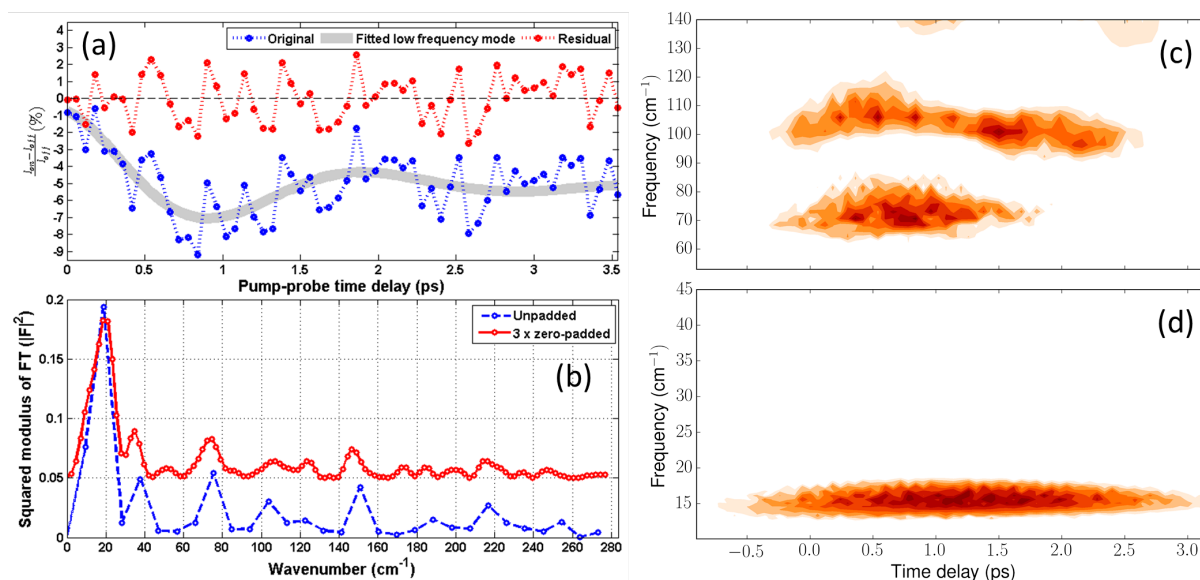
Figure 3.29: (a) Time-resolved trace of the diffraction peak (1,4,0) with 60 fs time steps (time points before time zero are removed). In the plot the low-frequency librational mode is subtracted to reveal high-frequency oscillations. Fourier transform of the original trace in (a) is presented in (b). (c-d) are wavelet spectrograms from CWT of the blue trace in (b) using two different sets of wavelet parameters that separate different frequency bands.

higher frequencies were present in the signal. Frequency analysis (e.g. see Fig. 3.29) using FFT and CWT reveals ~ 70 cm^{-1} mode oscillations that are frequently observed in the intensity changes of the diffraction peaks, some also show the characteristic vibrational frequency of I$_2^{-\bullet}$ that lies in the range of 100-110 cm^{-1} as shown in Fig. 3.29. As they mostly exist only within the first cycle of the 16-20 cm^{-1} libration mode and their strong resemblance to those observed in pump-probe experiments described earlier (compare with Fig. 3.18), they are the direct imprints of the reactants and photoproducts in the reaction. Further structural fitting will elucidate whether and how these modes participate in the triiodide reaction.

3.3.10 Summary and discussions

(1) A number of peaks show an abrupt change of intensity within 2 ps after photoexcitation. This signals a sudden displacement of atoms (e.g. bond-breaking events) that is induced by optical excitation.

(2) Coherent oscillations of the 10 cm^{-1} translation mode and the 16 and 20 cm^{-1} libration modes from ground-state I_3^- were prevalent in a number of Friedel pairs. High frequency modes with a frequency of about 70 cm^{-1} and 105 cm^{-1} were also observed. They are modes of ground-state $I_4^{-\bullet}$ and $I_2^{-\bullet}$, respectively[8]. Their coherence lasts for up to ~ 2 ps after photoexcitation, which matches well with similar modes observed in TA measurements. Due to limited time resolution and SNR, it's so far not possible to distinguish the contribution of these two species directly from time-resolved diffraction data. Inversion of the diffraction data is needed to pin down the particular types of motion. Nevertheless, these coherent features indicate concerted atomic motion initiated by 400 nm photoexcitation.

(3) Careful choice of the measurement condition allowed the triiodide reaction dynamics to be recorded up to 65 ps after photoexcitation. A multi-exponential recovery of the relative change is seen that goes beyond the recorded time delay of 65 ps. The behavior within this timescale is in qualitative agreement with the multi-staged behavior of the recombination dynamics observed in the TA experiment.

3.4 A possible reaction pathway involving $I_4^{-\bullet}$ formation

If two neighboring I_3^- chains are treated as a single reactive unit, a possible intermolecular reaction mechanism can be conceived and summarized in Fig. 3.30 based on the experimental evidence found so far. In this pathway, the reaction progresses along an intermolecular reaction coordinate, $R_2 + R_3 - R$, with the R's defined in the figure. The $I_3^- \cdots I_3^-$ and the $I_2^{-\bullet} \cdots I_4^{-\bullet}$ configurations each occupy a potential local minimum that

---

[8]The ground-state modes of $I_4^{-\bullet}$ is obtained from DFT calculation and shown in Table E.1.

can be connected through the triiodide reaction upon photoexcitation and relaxation back to the ground state PES. Here the symbol "$\cdots$" represents intermolecular interactions. The $I_2^{-\bullet}\cdots I_4^{-\bullet}$ configuration can be regarded as a metastable ground state while the $I_3^-\cdots I_3^-$ configuration is the true ground state. The two-chain partitioning does preserve the translation symmetry of the crystal and represents the minimal reactive unit sufficient to explain the observed structural dynamics ("a-axis chemistry" of TBAT). More specifically, the reaction coordinate construction mentioned above is based on experimental facts that $I_2^{-\bullet}$ and $I_4^{-\bullet}$ are formed in their respective ground states, because their ground-state vibrational modes (105 cm^{-1} for $I_2^{-\bullet}$ and 70 cm^{-1} for $I_4^{-\bullet}$) were detected and at least the excited states of $I_2^{-\bullet}$ all have dissociative characters [118]. The coordinate values at the potential minima are obtained by assuming an average I-I distance to be 2.9 Å. This is a fair assumption for both I_3^- and $I_4^{-\bullet}$.[9] The gap distance, R, in the $I_3^-\cdots I_3^-$ configuration is ~ 3.9 Å and can be found in Table B.1 of Appendix B. $I_2^{-\bullet}$ has a longer bond length (~ 3.3 Å, see Table E.1) but it only affects R_1 and not the R_2+R_3-R coordinate. Since the bending angle is small, a linear geometry is still a good approximation, which further simplifies the math. Therefore, the value of 1.9 Å is obtained by setting R_2 =R_3=2.9 Å and R=3.9 Å, and 3.9 Å is obtained by setting R_3=R=2.9 Å and R_2=3.9 Å. The excited state topology is not immediately conceivable as it remains an open question how many conical intersections connects it to the ground state [18]. The validity of this model can be proven by inverting the UED data along with support from theory, if needed. This work is currently in progress by Dr. Stuart Hayes, which is beyond the experimental scope of this thesis.

3.5 How do the two methods stack up

In both solid state TAS and UED measurements, the time resolutions are limited by the the probe pulse duration. Due to its broad bandwidth, the supercontinuum probe

---

[9]The I-I bond lengths for gas phase $I_4^{-\bullet}$ are 2.99 Å, 3.07 Å and 2.99 Å, with the longest being the bond between the two central iodine atoms. These results are from DFT calculations carried out by Dr. David Rogers.
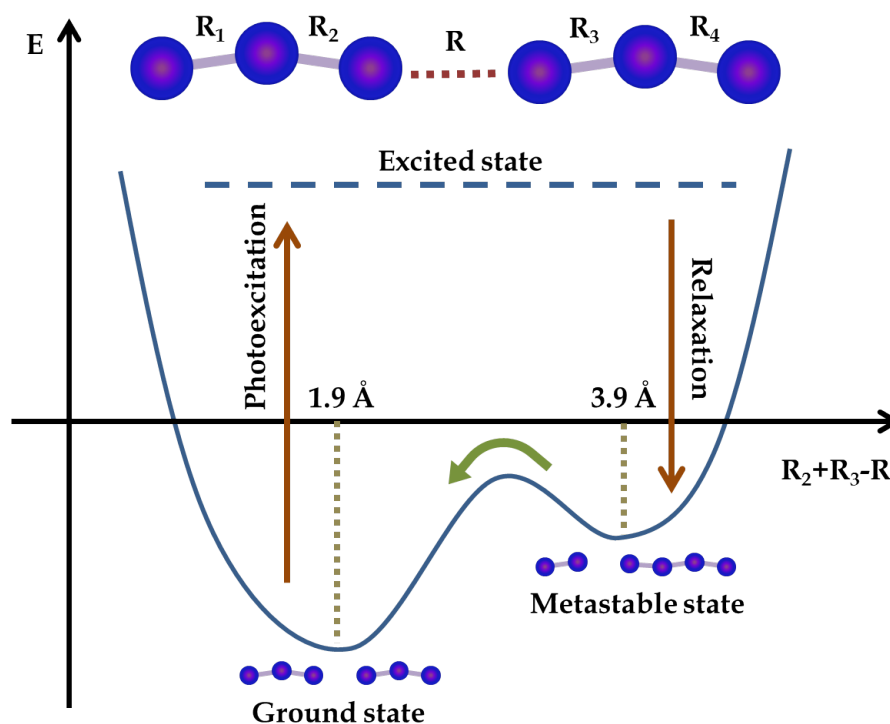
Figure 3.30: Cartoon of a possible intermolecular reaction pathway to generate $I_4^{-\bullet}$. The ground-state PES is approximated by an asymmetric double well while the excited state PES is complex. In the $I_3^- \cdots I_3^-$ configuration R_1-R_4 are intramolecular distances and R is the intermolecular gap. In the metastable $I_2^{-\bullet} \cdots I_4^{-\bullet}$ configuration R_1, R, R_3 and R_4 are intramolecular distances and R_2 becomes intermolecular. Along the reaction pathway the character of these distances may be ambiguous.

exhibits wavelength-dependent chirp that results in a wavelength-dependent system response function between ~ 100-150 fs. The electron pulses are estimated to have a duration of ~ 200 fs [72]. Therefore the resolution between the two experiments are not different by more than 100 fs. In either case, it is theoretically possible to resolve the period of the symmetric stretching mode of I_3^- and $I_2^{-\bullet}$ (300-350 fs). The very similar pump power and polarization dependence of the dynamical changes in TAS and in UED is a clear manifestation of the consistency between these two types of measurements.

Going beyond the similarities, in UED experiments, without inversion, the distinct species-specific dynamics involved in the reaction is, in general, not immediately

accessible from the change of the diffraction pattern, because one type of motion in the real space can affect all diffraction peak intensities in Fourier space by different amounts. Only in rare (and usually simple and restricted) cases can one find a direct link between Fourier and real space physical parameters [119, 120]. In TAS experiment, the real space species can usually be conveniently identified by the spectral region they emerge from, provided that there are no strong spectral overlaps of species with absorption change of similar value but opposite signs. In UED experiments, the signal has contribution from only the difference of nuclear arrangements between the excited and the intact molecules, whereas in TAS, due to the nonlinear nature of four-wave mixing process, other features like ESA or ISRS can also contribute to the differential absorption signal, thereby complicating the interpretation to some extent. An immediate distinction between the signals of these two types of measurements is that, in TAS, the $I_2^{-\bullet}$ band exhibits a sharp rise on the time scale of 200-300 fs (see Fig. 3.11b), but since the electronic change is mostly absent in UED, similar signature of the photoproduct generation only shows up as coherent oscillation with $\sim$ 2% amplitude change in the diffraction peaks, slightly above noise level ($\sim$ 1%). On the other hand, the slower rise of the 16 or 20 cm^{-1} libration mode can be taken unambiguously as a time zero signature in both UED and TAS data, since these lattice modes modulate both electronic structure and nuclear arrangement. Moreover, the ISRS process does not contribute to UED signal. Such different initial responses demonstrate the difference in the signal composition of these two types of time-resolved measurements. In practice, the difference in sample orientation in these two experiments (samples not cut from the same crystal) may also contribute to the different responses since phonon modes are sensitive to crystal orientation[10]. When considering the results from these experiments, such disparity should be taken into account, in addition to the observed common features. In the future, an *in situ* probe [121] can be installed to best correlate the measured sample responses from optical and electron probes at

---

[10]The other difference not compared is the SNR in the two types of measurments. In this respect, TAS measurements are usually at least better by 2 orders of magnitude than UED measurement.

approximately the same location.

The other thing to note is that since the whole spectral range of the I_3^- photochemistry spans from ~ 190-1000 nm (those of $I_3^- - I_2^{-\bullet}$ subsystem alone covering ~ 220-1000 nm), therefore it may not be possible to observe all modes found in the UED data in the TAS data due to limited probe spectral range. Lastly, there can exist dark (radiationless) intermediates that are not directly accessible via optical means but are detectable using electron diffraction [122].

To sum up, the clear advantage of UED, and the primary motivation for this study, is that it provides direct structural information. The TAS and UED results must agree on general features of the dynamics as is the case found here. However, TAS cannot tell the specific atomic or correlated motions giving rise to the transient species, whereas UED provides a direct measurement of the magnitude of these motions in a structural transition. This includes the key reaction modes leading to chemistry, and, therefore, UED offers a first-principle picture of reaction dynamics from experimental data. In the present case, the various diffraction orders need to be inverted to extract real space coordinates with certain convergence criteria. Completing this analysis requires more effort and was not possible within the time constraints of the PhD program.

4 Observation and outlook

Outline: This chapter begins by outlining the major difference between reaction dynamics in solution and solid state. Then a comparison between the current experiment and the iodine-doped-Kr experiment is drawn. This is followed up with a summary of prospective experiment and analyses for future investigation of the system. The chapter ends with a description of the theoretical challenges for a thorough understanding of the reaction dynamics.

4.1   Comparison of dynamics across phases

In molecular crystals, the molecular modes are assimilated into lattice modes but with the molecular characters preserved [123, 124]. The tightly ordered spatial arrangement of triiodide ions in the solid state provide a perfect environment to preserve the coherence and allow them to be detectable (at least one full period) via optical means. In this sense solid state experiments provide a more nuanced picture of the possible course of reaction complementary to solution phase studies. The observation of these novel modes that participate in the reaction reinforces this notion.

Additionally, the dissociation-recombination turning point in the solution phase triiodide reaction (see Fig. 2.5) is more than 10 ps delayed than that in the solid state (see Fig. 3.11). This quantitative feature is strong evidence of the environment dependence of the recombination dynamics—the triiodide ions are confined in smaller

pockets with well-defined orientation in the solid state and therefore the recombination process starts to dominate earlier. Such local environment difference may well come to the point of altering the dissociation/recombination channel, as demonstrated in the possible observation of $I_4^{-\bullet}$ from the TAS results described in section 3.2.5. The inter-triiodide distance in TBAT solid is ~ 3.9 Å, only $\lesssim 1$ Å longer than the I-I bond distance, and the orbitals from neighboring chains may have already overlapped with each other[1]. The I_3^- dissociation may not require a significant atomic displacement larger than 1 Å, as is the case in the gas phase.

Another nontrivial difference between the kinetics seen in the two condensed phases is the polarization dependence. Even though the solid state transient anisotropy measurement is not explicitly performed, from the pump polarization dependence and the crystalline geometry, one can infer that the reaction should progress in a very limited dimension, from which $I_4^{-\bullet}$ can be produced due to head-on collision of an $I^\bullet$ fragment with the nearby triiodide chain. This is in stark contrast to the almost random orientation of the dissociated photoproducts observed in solution phase from transient anisotropy measurements [82, 86].

4.2 Coherence transfer in the solid state

The vibrational coherence transfer between I_3^- and $I_2^{-\bullet}$ fragment is evident in the coherent stretching oscillations of $I_2^{-\bullet}$ in its absorption band around 785 nm. The appearance of low frequency modes in the dynamics implies the coherence transfer to the lattice. Previously such behavior has been observed in I_2-doped Kr solids. When I_2 undergoes photodissociation and recombination, the excess energy is transferred through coherent interaction between the $I^\bullet$ and the Kr matrix [125, 126]. In this way the Brillouin zone-boundary phonon modes were excited and observed in the transient absorption traces. The difference between the TBAT and the I_2-in-Kr

---

[1]I thank Dr. Stuart Hayes for promoting a similar idea in the first place. The spectroscopic evidence was only discovered later when scrutinizing the unknown part of the TAS data.

experiments is that in TBAT the triiodide ions are part of the lattice (the phonon modes feature their concerted motion) and only phonon modes near the Γ-point (zone-center phonons) are of relevance to optical excitation. On the other hand, the iodine molecules in Kr solid are doped impurities and they don't form a sublattice due to the random spatial distribution of these "chromophores", so even though the phonon oscillations are induced by the iodine reaction, they are played out by the motion of the Kr atoms of the host matrix only.

4.3   The unresolved & the challenging

Even as one of the most studied triatomic systems, I_3^- is still offering fresh insights into reaction dynamics of simple chemical systems as new methods are being employed to explore further details. The content of this thesis as well as recent publications by other groups [30, 31, 33] showcase new advancements in this line of research. The UED part of the study is a stimulus for pushing the temporal resolution frontier. Even though the present study made use of the electron number-pulse duration trade-off to achieve desirable resolution, the time resolution of the experiment can certainly be improved using shorter electron pulses. With the next generation of UED machines running at 300 keV now becoming available [127] and having a theoretical time resolution of $\sim$ 80 fs, studies on faster (and irreversible) reaction kinetics in molecular systems will surely be made possible. The following points summarize some relevant future works on the subject.

4.3.1   Surface-crossing dynamics

Since $I_2^{-\bullet}$ is the photoproduct that connects to the antisymmetric stretching mode (v_3) of I_3^-, logically speaking, there should be a glimpse of I_3^- in a v_3 vibrational state before it slides down the excited state PES towards the exit channel, where $I_2^{-\bullet}$ and $I^\bullet$ are produced. So far this impulsively excited I_3^- placed in an excited state antisymmetric stretching mode hasn't been directly captured by any means, though coherent ground-

state ν_3 oscillations have been detected in an impulsive stimulated Raman experiment in solution [87]. To determine the excited-state modes, a three-pulse experiment involving a sequence of pump, Raman/THz and probe pulses can be used.

4.3.2 Reconstruction of reaction intermediates' spectra

The observation of the spectroscopic signature of $I_4^{-\bullet}$ from the results presented in this thesis adds another dimension to the triiodide reaction dynamics. However, the spectra of the reaction participants (reactant, intermediates and photoproducts) are all redshifted by various amounts due to the influence of the crystal field. A full spectral reconstruction of these species is one necessary step forward. This requires target analysis based on the different DAS extracted from global analysis. However, due to the lack of information on the fluorescence spectrum of I_3^-, $I_4^{-\bullet}$ and the knowledge of the excited state absorption of I_3^-, the spectral reconstruction remains a challenging task for the time being.

4.3.3 Detection of I^- and ground state dynamics of I_3^-

Since the absorption of the participating species in the triiodide reaction collectively cover a very broad spectral region (from the blue end of I^- absorption at $\sim$ 190 nm to the red end of $I_2^{-\bullet}$ absorption at close to 1000 nm), monitoring this whole spectral range with good time resolution (< 100 fs) is not yet attainable with homogeneous media. One spectral region of immediate interest lies in the ground-state absorption band below 400 nm, where signs of the emergence of another band is already present in the current results (see Fig. A.1 and A.4 in the appendix). Probing the absorption bands of I^- can provide evidence on the reaction's branching ratio, when comparing with the yield of $I_2^{-\bullet}$.

In terms of the source of the probe pulses, photonic crystal fiber (PCF) is can generate an ultrabroadband supercontinuum [128] covering the desired spectral region, but its

spectral energy density is still too low for probing strongly absorbing species like I_3^- and pulse compression also presents a major difficulty. Nevertheless, a workaround exists. It's currently possible to look at a small probe spectral window ($\sim$ 50-100 nm) with few-fs time resolution using compressed NOPA pulses as the probe. Using a combination of multiple spectrally-resolved NOPAs generated from a single fs Ti:Sapphire laser can cover most of the mid-UV to IR spectral range as thoroughly discussed in [78]. Good time resolution also means that one may be able to resolve vibrational overtones [129, 87] and combination modes [87] at higher frequencies (150 cm^{-1} and above). Such anharmonic modes will help recover the topology of triiodide's PESs (e.g. through fitting empirical PESs) that leads to the suppression of the dissociation channel that yields I_2 in condensed phases.

4.3.4 Electron diffraction study of coherently-controlled reaction

As shown in the coherent control experiment in Chapter 2, the triiodide dissociation yield can be controlled conveniently by adjusting the second-order chirp in the pump pulse. The effect of chirp in displacing atoms in real space hasn't been studied using structurally resolved methods in the solid state. An educated guess is that the sign of the second-order chirp can accelerate or decelerate the atomic motion compared with excitation using TL pulses. The difference from such a chirp effect can be small and one needs better SNR to distinguish the difference than achievable currently. Moreover, it remains to be seen whether the reconstruction technique recently developed [72] for inverting time-resolved electron diffraction data can be used to benchmark the atomic displacements obtained from chirped-pulse excitation against that with TL pulse excitation.

4.3.5 Quantification of optical damage

The origin of optical damage in opaque medium is material-specific. The type of damage can range from thermally-induced as in the study of the melting of Al [67]

to the mostly strain-induced damage in ring-closing reaction of diarylethene [75] to the present triiodide reaction, which is likely a mixture of the two. In-situ probing of optical properties of the thin crystalline sample can be integrated into the electron diffraction chamber for diagnosing the sample condition along the experiment, as well as postmortem analysis using, e.g., a light microscope or an imaging spectrometer. For nonreversible samples, this approach will provide valuable information on the formation of optical damage (e.g. sample ionization, accumulated photothermal species, etc.) which leads to artefactual signals and point to ways to reduce it in order to make the sample suitable for stroboscopic-type studies.

4.4 Benchmark for theory development

Last but not the least, the reaction dynamics of I_3^- investigated in the thesis sets a benchmark for *ab initio* molecular dynamics simulation [130] of condensed phase chemistry. Treating the triiodide system is computationally expensive, due to the number of electrons needed to consider exactly (at least 44 for the $I_3^- \cdots I_3^-$ configuration)[2], the large spin-orbit interaction (SOI) [131], the proper treatment of open-shell radical intermediates and conical intersection dynamics, which altogether brought about the richness of the reaction dynamics of polyatomic molecules with more than three atoms. In recent developments [15] in gas-phase calculations, good agreement with experiment has been found at the relativistic coupled cluster and configuration interaction level of theory. Pushing this to the condensed phase and accounting for reactive environment requires further theory development and optimization of computational resources. Therefore, structural inversion of the UED results will provide valuable reference to guide these developments.

---

[2]Each iodine atom ([Kr]$4d^{10}5s^25p^5$) contains seven valence electrons ($5s^25p^5$). The $I_3^- \cdots I_3^-$ configuration contains two excess charges in addition to the six iodine atoms.

A Supplementary figures of solid state optical pump-probe spectroscopy

A.1 Short-time dynamics

The 2D plots for the datasets acquired at temperatures of 80 K, 135 K and 190 K are shown in Fig. A.1. For comparison, the line cuts along the wavelength direction for the 60 fs-step data at 245K and at 80 K are shown in Fig. A.2 and Fig. A.3, respectively. In these plots, a clear temperature-dependent shift of bands to shorter wavelength is seen, especially for the region < 530 nm. The crossover region (likely an isosbestic point) between the librational bands with opposite signs is located at ~ 480 nm at 245 K and at ~ 491 nm at 80 K. The shift is most striking in the region 500-530 nm, where at 80 K the low-frequency beats (~ 18 cm^{-1}) show a growing trend in the first three cycles before decaying, whereas at 245 K only damped oscillations of very similar frequency are seen. The vibrational oscillation in the region > 600 nm shows higher peak-to-peak contrast at 80 K than at 245 K. In general, the dephasing time of all modes is longer at 80 K than 245 K.

A.2 Long-time dynamics

The 2D plots for the datasets at temperatures of 80 K, 135 K and 190 K are shown in Fig. A.4. The bleaching and growing bands don't fully recover in this time range (up to ~ 1.6 ns). Moreover, the growing signal appearing in the region < 430 nm at long time
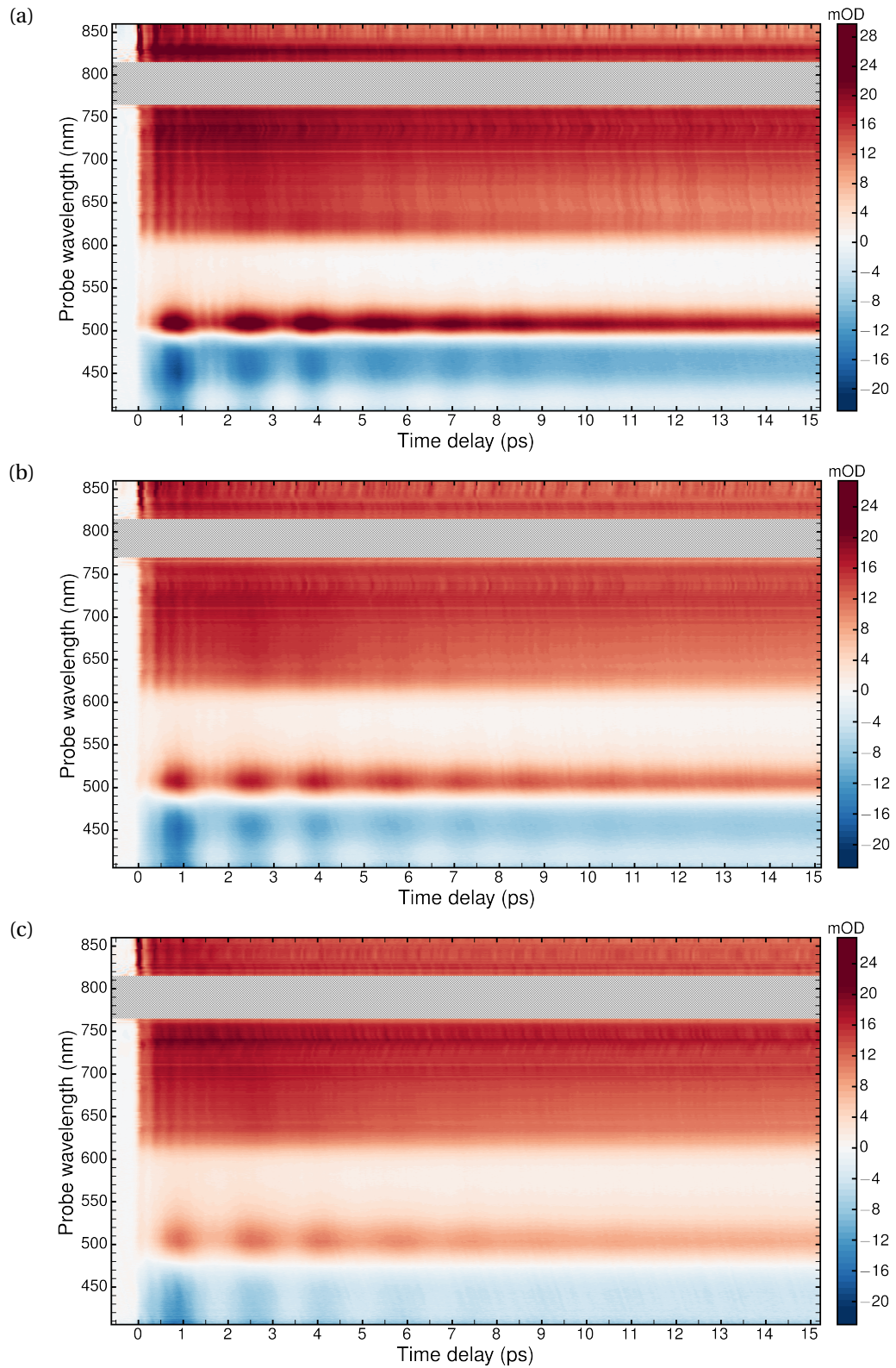
Figure A.1: 2D filled contour plots of TA measurements performed with 60 fs steps at (a) 80 K, (b) 135 K and (c) 190 K. The hatches block the region affected by the instability around the 800 nm supercontinuum pump. Chirp correction has been applied to all datasets.
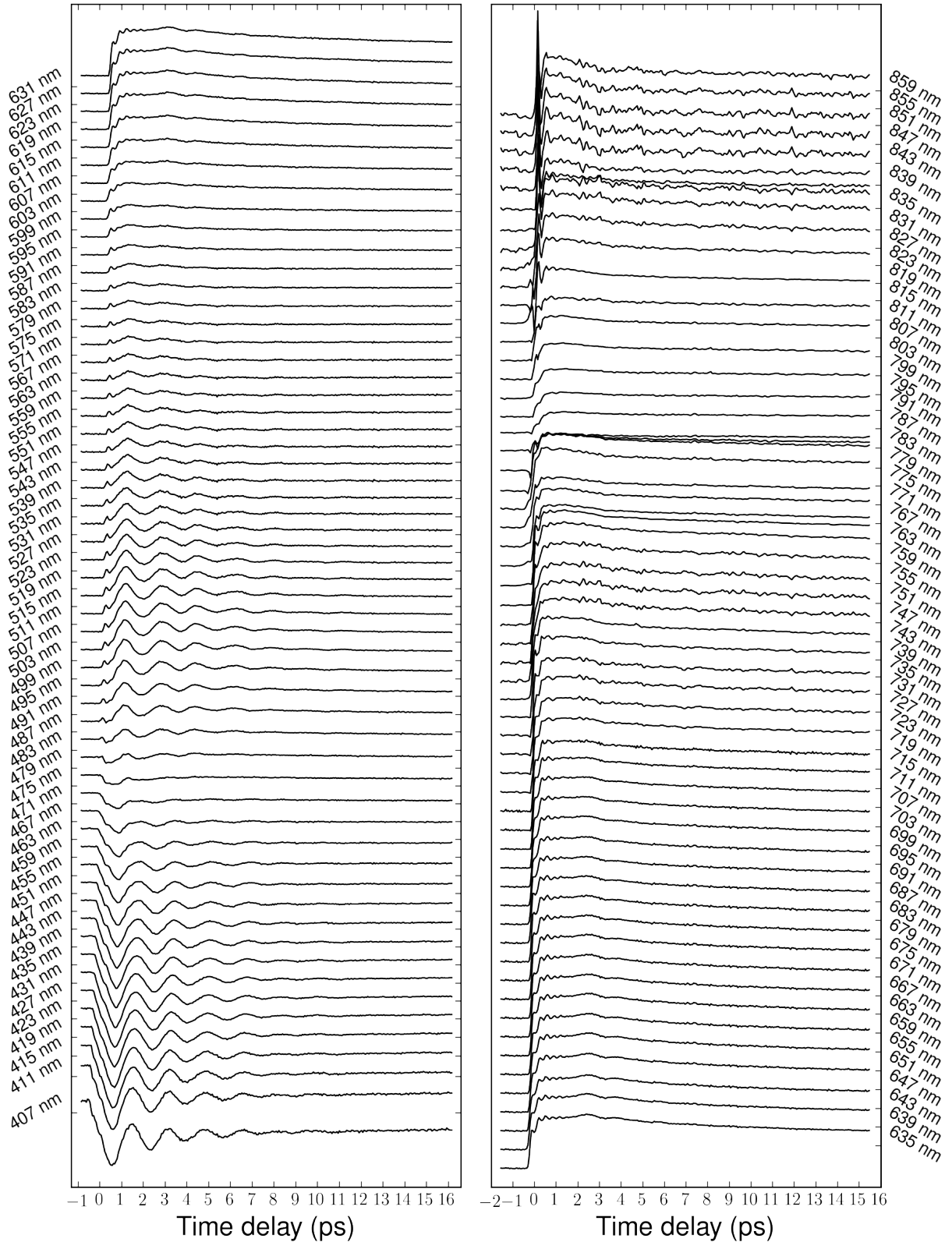
Figure A.2: Wavelength-binned line cuts of the dataset measured at 245 K with 60 fs steps. Each line spans a region of 4 nm, with the center wavelength shown next to each trace. The time zero for each trace is not adjusted for the chirp in the supercontinuum probe. A weak local regression filter (LOESS) is applied to traces beyond 712 nm.
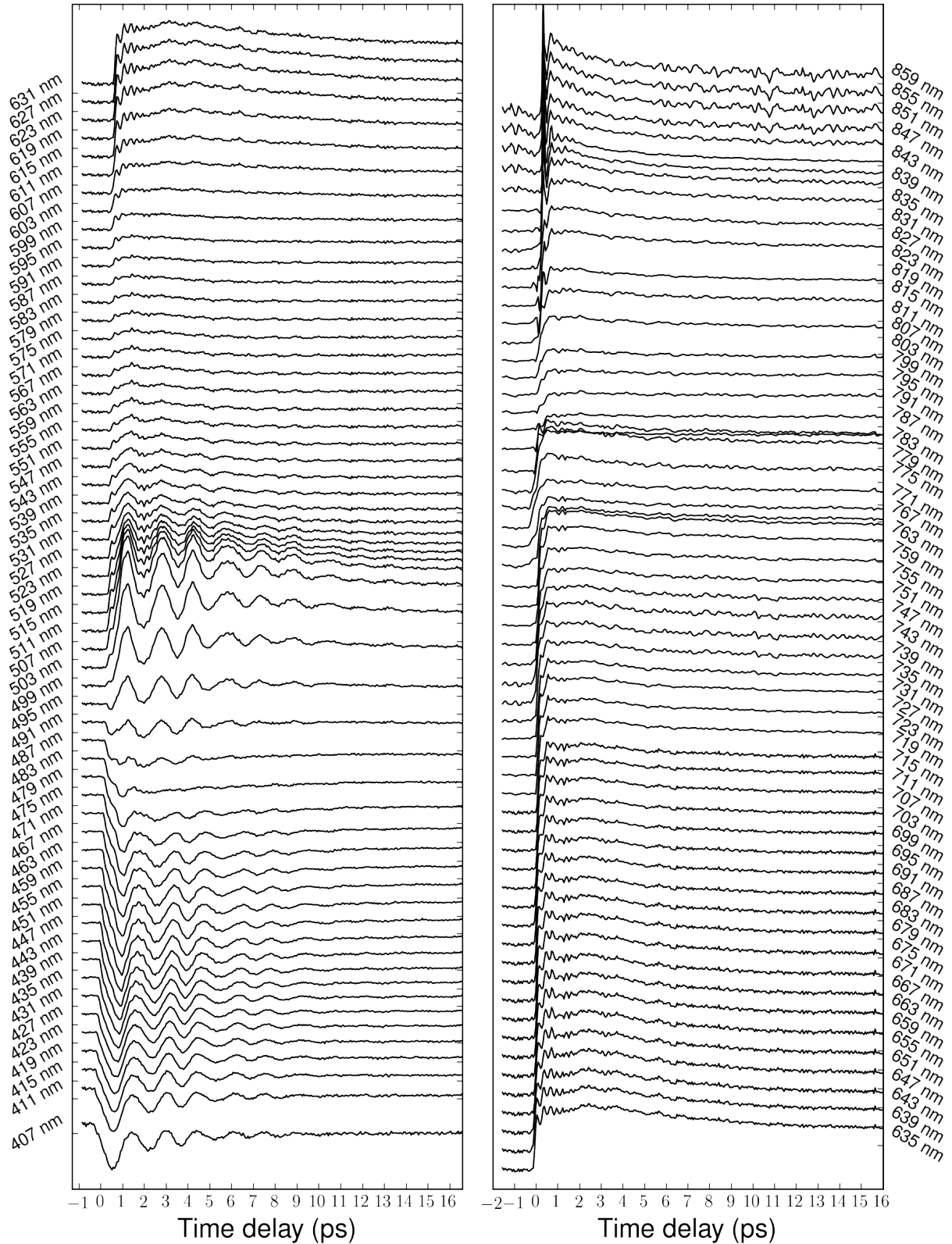
Figure A.3: Wavelength-binned line cuts of the composite dataset measured at 80 K with 60 fs steps. Each line spans a region of 4 nm, with the center wavelength shown next to each trace. The time zero for each trace is not adjusted for the chirp in the supercontinuum probe. A weak LOESS filter is applied to traces beyond 712 nm.

Appendix A. Supplementary figures of solid state optical pump-probe spectroscopy
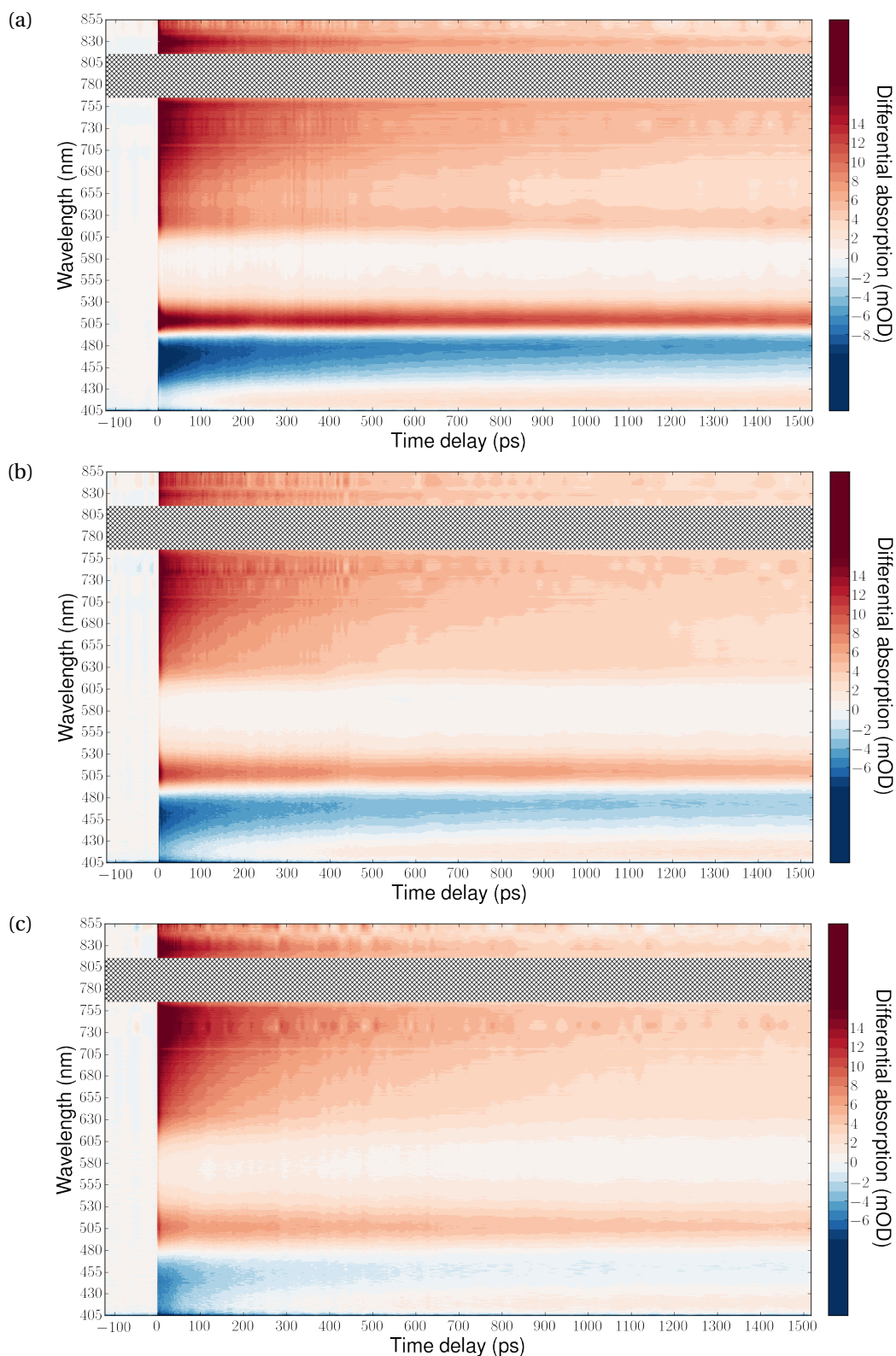
Figure A.4: 2D filled contour plots of measurements performed with a combination of time steps (from 1 ps to 20 ps) at (a) 80 K, (b) 135 K and (c) 190 K. The hatches block the region affected by the instability around the 800 nm supercontinuum pump.

Figure A.5: Wavelength-binned line cuts of the composite dataset taken at 245 K with various time steps of 1 ps, 10 ps and 20 ps after photoexcitation. Each line spans a region of 4 nm, with the center wavelength shown next to each trace. A weak LOESS filter is applied to all traces.
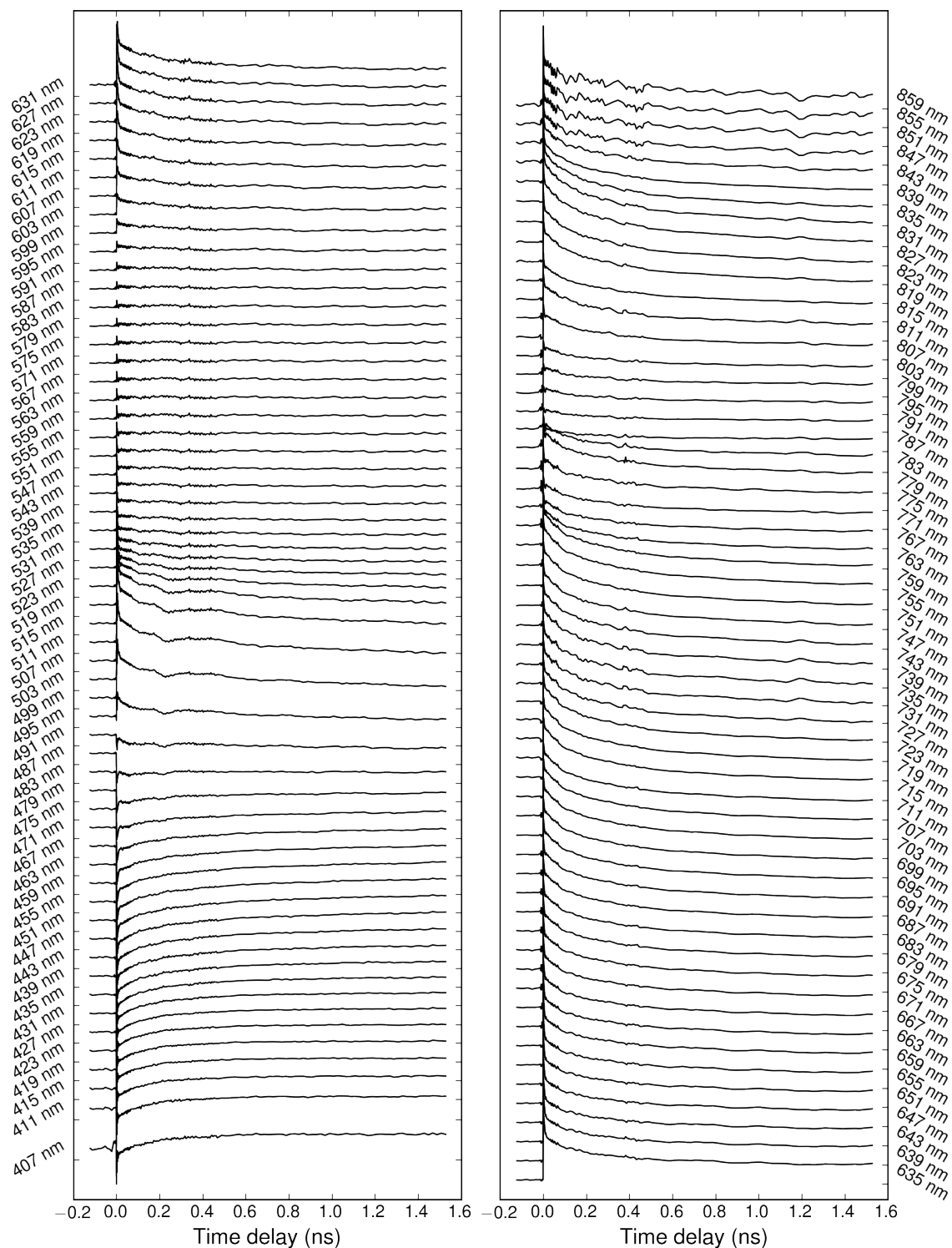
Figure A.6: Wavelength-binned line cuts of the dataset taken at 80 K with steps of 1 ps, 5 ps and 20 ps after photoexcitation. Each line spans a region of 4 nm, with the center wavelength shown next to each trace. A weak LOESS filter is applied to all traces.

delays is stronger at lower temperatures.

Similar to the previous section, the line cuts along the wavelength direction for the long-time scans at 245 K and at 80 K are presented for comparison in Fig. A.5 and Fig. A.6, respectively. The spectral region between 500-530 nm develops a very noticeable band shift between time delays of 200 and 600 ps, this feature is, however, absent in the 245 K data. In fact, this feature still exist in data taken at 107.5 K (not presented here) and 135 K, only with the exact turning point in time delayed further by a few hundred ps. It becomes barely noticeable at the next temperature with available data (190 K). This is another strong indication of temperature-dependent kinetics.

A.3   Temperature dependence of the DAS

Besides the four-component global fit to the TA spectra presented in section 3.2.5, a five-component fit using time constants obtained from single-trace fitting is found to better fit the 530-600 nm region than having only four components. Nevertheless, the general features of the emergence and decay of $I_4^{-\bullet}$ in the DAS between the four and five component fits are very similar. Using this set of time constants to fit the datasets at the four different temperatures, one obtains the DAS presented in Fig. A.7. The first component is omitted there since it has a time constant of ~ 90 fs, which is less than the temporal resolution of the system, and therefore should be attributed to Kerr effect or any unresolved fast dynamics. Based on the influence of the ground-state absorption of the $I_2^{-\bullet}$, I_3^- and $I_4^{-\bullet}$ species in different spectral ranges (labeled in Fig. A.7d), these timescales can be attributed to,

(a) $I_2^{-\bullet}$ formation from I_3^- dissociation

(b) first phase of $I_2^{-\bullet}$ recombination and onset of $I_4^{-\bullet}$ formation

(c) $I_4^{-\bullet}$ dissociation (forming I_3^- and $I^\bullet$)

(d) I_3^- recovery and second phase of $I_2^{-\bullet}$ recombination

Appendix A. Supplementary figures of solid state optical pump-probe spectroscopy

In this assignment, the (b)-(d) components are close match with the second, third and fourth components of the four-component fit (see Fig. 3.14). From these four DAS it is evident that while the $I_2^{-\bullet}$ dynamics in (a) and (d) is less affected by temperature, the $I_2^{-\bullet}$ formation and decay have a strong temperature dependence. This dependence probably comes from the change of lattice parameters such as the length of the unit cell a axis (see Table B.1), which in turn modifies the barrier and the shape of the PES where the $I_2^{-\bullet}\cdots I_4^{-\bullet}$ configuration resides in a local minimum (see Fig. 3.30).
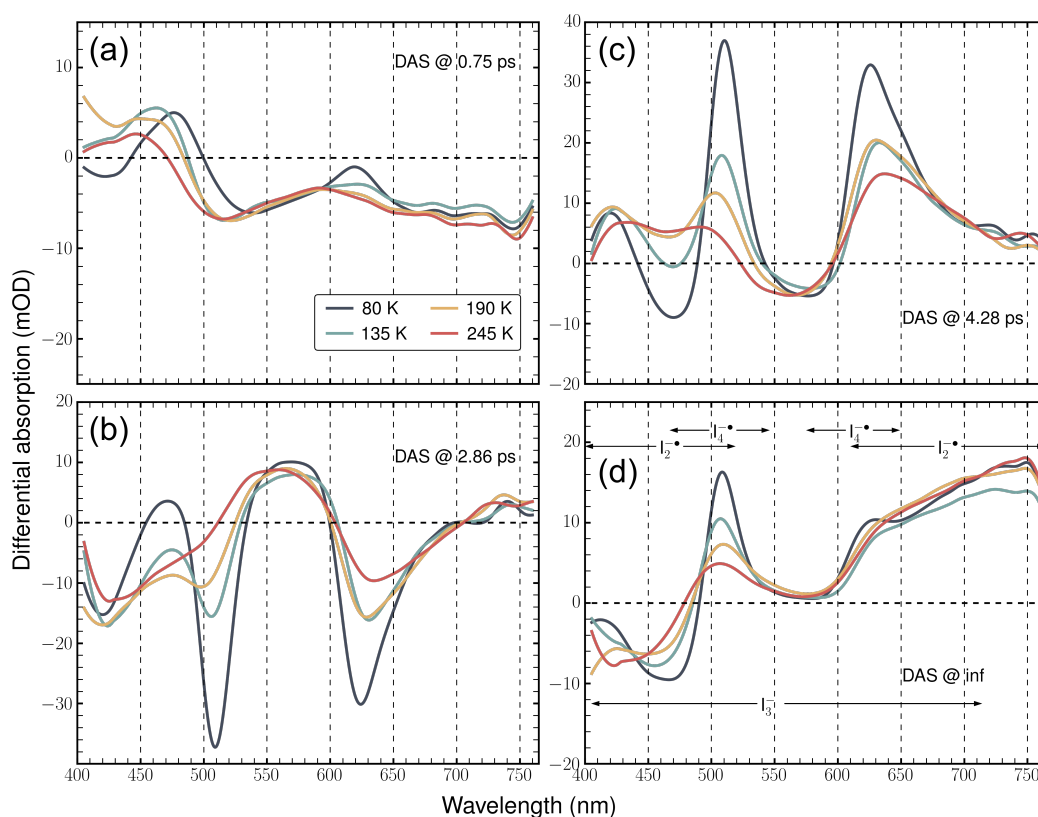
Figure A.7: DAS of the TA datasets obtained at different temperatures (from -1 ps to ~ 15 ps). They come from five-component fits to the TA time series alternative to those in Fig. 3.14. The four of the five components with a time constant longer than the system temporal resolution are shown in chronological order in (a)-(d). The legend in (a) shows the color coding of the temperatures and the spectral region influenced by the ground-state absorption of related polyiodide species are labeled in (d).

102

B Supplementary information on ultrafast electron diffraction

B.1 Comparison of deposited TBAT crystal structures

There are in total five static crystal structures available from the Cambridge Structural Database (CSD) collected from three independent groups. The main features of these structures are compared in Table B.1.

Except the structure from Herbstein et al [132], in which the triiodide axis was set to be c, all other structures assigned that axis a. The unit vectors a and c between these two kinds of assignments are therefore swapped accordingly. The temperatures at which the structures were determined vary from 123 K to 295 K. The temperature difference appear to only slightly affect the unit cell vector lengths and, therefore, the cell volume. No polymorphism nor phase transition was observed in the temperature range of these measurements. In every structure there are two types of I_3^- chains with different opening angles and they occupy crystallographically independent lattice sites. The dihedral angle in Table B.1 refers to the acute angle between these two independent triiodide chains in a unit cell.

Table B.1: Deposited crystal structures of TBAT in CSD

Name	NBAMTI10	NBAMTI11	NBAMTI12	NBAMTI13	NBAMTI14
Year	1981	2008	2008	2008	2012
T (K)	295	295	150	123	173
Space group	P-1	P-1	P-1	P-1	P-1
a (Å)	15.791(8)	9.5696(9)	9.5035(5)	9.4964(5)	9.5161(9)
b (Å)	15.993(8)	15.7420(11)	15.6467(8)	15.6142(7)	15.6549(15)
c (Å)	9.578(5)	15.9714(11)	15.8771(7)	15.8505(7)	15.8860(15)
α (°)	74.48(8)	83.429(6)	83.395(4)	83.387(4)	83.4610(10)
β (°)	101.52(9)	74.398(7)	74.164(4)	74.176(4)	74.2290(10)
γ (°)	96.63(9)	78.694(7)	78.444(4)	78.507(4)	78.5220(10)
V (Å^3)	2278.8	2267.5(3)	2220.69(19)	2211.27(18)	2227.5(4)
Z	4	4	4	4	4
R factor	N/A	0.1133	0.0439	0.065	0.031
I-I-I axis	c	a	a	a	a
r(I3-I1) (Å)	3.988	2.9383	2.9467	2.9485	3.875
r(I1-I2) (Å)	2.9513	2.9086	2.9166	2.9192	2.963
r(I2-I3) (Å)	2.887	3.784	3.6978	3.6852	2.8973
$\angle$(I1-I2-I3) (°)	178.46	174.78	174.73	174.74	178.42
r(I6-I4) (Å)	3.789	2.8897	2.9613	2.9644	3.7088
r(I4-I5) (Å)	2.911	2.9509	2.8959	2.8985	2.9478
r(I5-I6) (Å)	2.9404	3.9733	3.8617	3.8441	2.9179
$\angle$(I4-I5-I6) (°)	174.66	178.48	178.40	178.37	174.75
Dihedral angle (°)	15.44	15.29	14.307	15.481	15.782

B.2   Static rotation series

The sample holder can be rotated about the y direction perpendicular to the electron beam, thereby altering its incidence angle. Within a mere 5 degrees (rotation is limited by the available space and translation stage travel range for linear shift compensation), significant changes of the diffraction pattern appear (see Fig. B.2). The rotation series is crucial for the determination of sample orientation described in section 3.3.4.

Figure B.1: (a) Static diffraction pattern of a crystal cut along a different orientation. The image is put on log grey scale to expose the stripes. (c) Time-resolved dynamics of the integrated quadrilateral region shown with red outline in (b).

B.3 Stripe dynamics at a distinct orientation

Other interesting dynamics are seen from samples cut from a different crystal close to a natural cleavage plane. The static diffraction pattern shows very noticeable "stripes" that are most likely caused by closely spaced diffraction peaks with very similar Miller indices. The time-resolved dynamics of spots show similar low-frequency libration modes as well as high frequency modes identical to those discussed in Chapter 3.

(a)

87°

(b)

88°

(c)

89°

(d)

90°

(e)

91°

(f)

Figure B.2: (a-e) Diffraction patterns from 5 distinct electron incidence angles (the angle shown on each corner is the reading from the manipulator. In practice, it is very close to the incidence angle of the electron beam). (f) Angular dependence of the peak intensities extracted from a selecttion of peaks present in all five diffraction patterns.

Figure B.3: Difference images ($I_{on} - I_{off}$) of a time-resolved scan on the "stripy" sample described in section B.3. The region within each stripe appears to change altogether with the same sign. The red and blue colors denote positive and negative changes, respectively.

Appendix B. Supplementary information on ultrafast electron diffraction

Additionally, the region the stripes occupy appear to change synchronously with the same sign after time zero. A graphical representation is shown in Fig. B.1 and B.3. Since the orientation hasn't been determined for this sample, no conclusive information as to the origin of the stripes can be inferred at the moment.

C Time-frequency analysis

Time-frequency representation (TFR) offers a balanced view of the temporal and frequency behavior of nonstationary signals encountered in time-series measurements like the various pump-probe spectroscopic methods mentioned in this thesis. Generally, two types of representations are used and they are based on 2-dimensional transforms $R(\tau, f)$ of 1-dimensional time series $s(t)$. They are named accordingly as linear and quadratic time-frequency representations [133]. The linear representation has the unit of amplitude, whereas in the quadratic representation the values take on the unit of energy. This appendix first describes the two kinds of representations used in the frequency analysis of time-resolved signals — the short-time Fourier transform and the continuous wavelet transform, and their respective quadratic representations, the spectrogram and the scalogram. Their relative advantages and drawbacks are discussed along the way. Then the actual method for analyzing the solid state optical pump-probe data is presented.

It is important to note that a TFR of any form is always subject to Heisenberg's uncertainty principle and the choice of the most relevant TFR or frequency analysis technique is entirely dependent on the kind of signal and the level of noise present therein. The general purpose is to isolate the frequency components with a reasonable trade-off between temporal and frequency resolution. The available methods are not

limited to the ones presented in this appendix. Recent researches have demonstrated the potentials of other useful techniques [134, 135].

C.1   Short-time Fourier transform

Invented by Dennis Gabor in 1946 [136], the short-time Fourier transform (STFT) extends the continuous-time Fourier transform (CTFT) to extracting frequency components as a function of time. Though Gabor originally used a Gaussian window to filter the signal in time, various other windows [114] can be applied based on the type of frequencies present in the signal. With a generic window function $g(t)$, the STFT of a time-dependent signal $s(t)$ is defined as [137],

$$STFT(\tau, f) = \int s(t) g^*(t - \tau) e^{-2i\pi ft} dt \tag{C.1}$$

When $g(t - \tau) = 1$, that is to say if one applies an infinitely long window (or as long as the signal's duration) with unit amplitude to the signal, one recovers the CTFT of the signal $s(t)$. In other words, CTFT is the long-time limit of STFT. The absolute square of STFT is defined as the spectrogram $Sp(\tau, f)$ [133],

$$Sp(\tau, f) = |STFT(\tau, f)|^2 \tag{C.2}$$

The Heisenberg uncertainty relation stipulates that all simultaneous time and frequency measurement outcomes are subject to the inequality,

$$\Delta t \Delta f \geqslant \frac{1}{4\pi} \tag{C.3}$$

where Δt and Δf are, respectively, the standard deviation of the time and frequency, or the temporal and frequency resolution in the present context. In STFT, Δt and Δf

are defined as [137],

$$\Delta f = \sqrt{\frac{\int f^2 |G(f)|^2 df}{\int |G(f)|^2 df}} \tag{C.4}$$

$$\Delta t = \sqrt{\frac{\int t^2 |g(t)|^2 dt}{\int |g(t)|^2 dt}} \tag{C.5}$$

where $G(f) = \mathscr{F}(g(t))$. These equations demonstrate that Δt and Δf are only dependent on the chosen window function $g(t)$, which uniquely defines $G(f)$. Therefore the STFT representation divides the time-frequency plane into identical cells of sides Δt and Δf (see Fig. C.1a). Here each cell is called a *Heisenberg box* and has an area no smaller than $\frac{1}{4\pi}$ according to Eq. C.3. For a Gaussian window of the form $g(t) = e^{-\alpha t^2 \tau^2}$, one obtains $\Delta t = \frac{t}{2\sqrt{\alpha}}$ and $\Delta f = \frac{\sqrt{\alpha}}{2\pi t}$, and therefore $\Delta t \cdot \Delta f = \frac{1}{4\pi}$, the lower bound is satisfied [138]. This is analogous to the fact that the Gaussian wavefunction has the minimum uncertainty in quantum mechanics. The feature of constant temporal and frequency resolution of STFT in all time-frequency plane implies one of its significant drawbacks and is illustrated with an example in Fig. C.2.
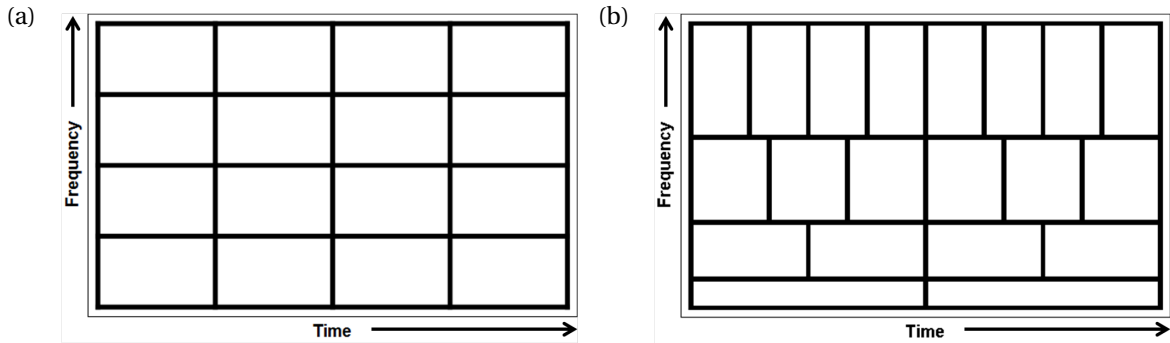
Figure C.1: Comparison of the time-frequency uncertainties of (a) STFT and (b) CWT. Each cell in these two diagrams is a Heisenberg box bounded by sides that correspond to the temporal and frequency resolution of a Gaussian window (as in STFT) or envelope (as in CWT). Only two frequency components separated well enough in time and frequency (i.e. in two distinct Heisenberg boxes) can be distinguished unambiguously in each diagram. STFT has the same temporal and frequency resolutions everywhere in the plane while CWT has frequency-dependent temporal and frequency resolution.

C.2   Continuous wavelet transform

Wavelet is the English translation of the French term *ondelette,* and the technique was for a large part developed in France. The advancement of wavelet analysis was prompted by real-world problems such as the ones petroleum engineer Jean Morlet faced in the 1970s when analyzing time-resolved signals using STFT, mainly due to its fixed time-frequency resolution [139, 140]. He devised a set of bases and, along with mathematical physicist Alexandre Grossmann, the mathematics to extract frequency components with varying resolution [141, 142]. These bases are still used today and bear Morlet's name. In this thesis, the complex Morlet wavelets are used for analyzing time-resolved signals. They have the form [143],

$$h_M(t) = \frac{1}{\sqrt{\pi f_b}} e^{2i\pi f_c t} e^{-\frac{t^2}{f_b}} \tag{C.6}$$

where f_b is the bandwidth and f_c is the center frequency of the wavelet. The continuous version of the transform, thus named the continuous wavelet transform (CWT) is constructed by the inner product of the analyzed signal with the mother wavelet[1] of choice (i.e. the complex Morlet wavelet) in its scaled (contraction and dilation) and time-shifted form. The CWT is written expressly as,

$$CWT(\tau, a) = \frac{1}{|a|} \int s(t) h^*(\frac{t - \tau}{a}) dt \tag{C.7}$$

Here $h^*(\frac{t-\tau}{a})$ denotes that the mother wavelet $h(t)$ is time-shifted by τ and scaled by $\frac{1}{a}$. Different types of bases can be chosen as the mother wavelet. Besides the (complex) Morlet wavelet defined before, Daubechies wavelet and the Meyer wavelet are also frequently used for practical applications. The choice of mother wavelets hinges on the type of oscillatory feature in the signal. The general principle is that the mother wavelet should bear some resemblance to the oscillatory feature. For

---

[1]The name mother wavelet was chosen because it generates other scaled and time-shifted wavelets when the transform is performed.

the pump-probe-type signal with sinusoidal decays, the complex Morlet wavelet is a natural choice, the Haar wavelet that resembles a step function would be a bad choice. For a 2-parameter wavelet like the Morlet wavelet, one also needs to determine the center frequency f_c and the bandwidth f_b. For the best resolution trade-off, these will be chosen based upon the frequencies to be resolved on a trial and error approach. One can also use initial sound guesses from frequencies obtained from FFT or STFT to determine f_b and f_c.

It's important to note here that strictly speaking, CWT transforms the 1D signal into the time-scale plane whereas the STFT works on the time-frequency plane. However, the scale can be converted into frequency using the formula,

$$f = \frac{f_c}{a \cdot \Delta t} \tag{C.8}$$

Even though f_b doesn't factor into the frequency conversion, it will affect the frequency resolution on a 2D time-frequency diagram. Analogous to STFT, the absolute square of CWT is defined as the wavelet spectrogram or scalogram $Sc(\tau, f)$ [133],

$$Sc(\tau, f) = |CWT(\tau, f)|^2 \tag{C.9}$$

A gallery of scalograms with different frequency features can be found in [144]. For the complex Morlet wavelet, one can obtain the frequency resolution $\Delta f = \frac{1}{a \cdot 2\pi \sqrt{f_b}}$, and the temporal resolution $\Delta t = \frac{a\sqrt{f_b}}{2}$. So even though the product $\Delta t \Delta f$ is still $\frac{1}{4\pi}$, the expressions of Δt and Δf are now dependent on the scale a, very different from the constant Δt and Δf of STFT. The time-frequency plane is, as a result, divided into Heisenberg boxes with unequal sides of varying lengths as shown in Fig. C.1b. From this diagram one can also find out the drawbacks of wavelet transform — a fixed mother wavelet has a poorer time resolution and a poorer frequency resolution for low and high frequency components, respectively. In real-world signals, however,
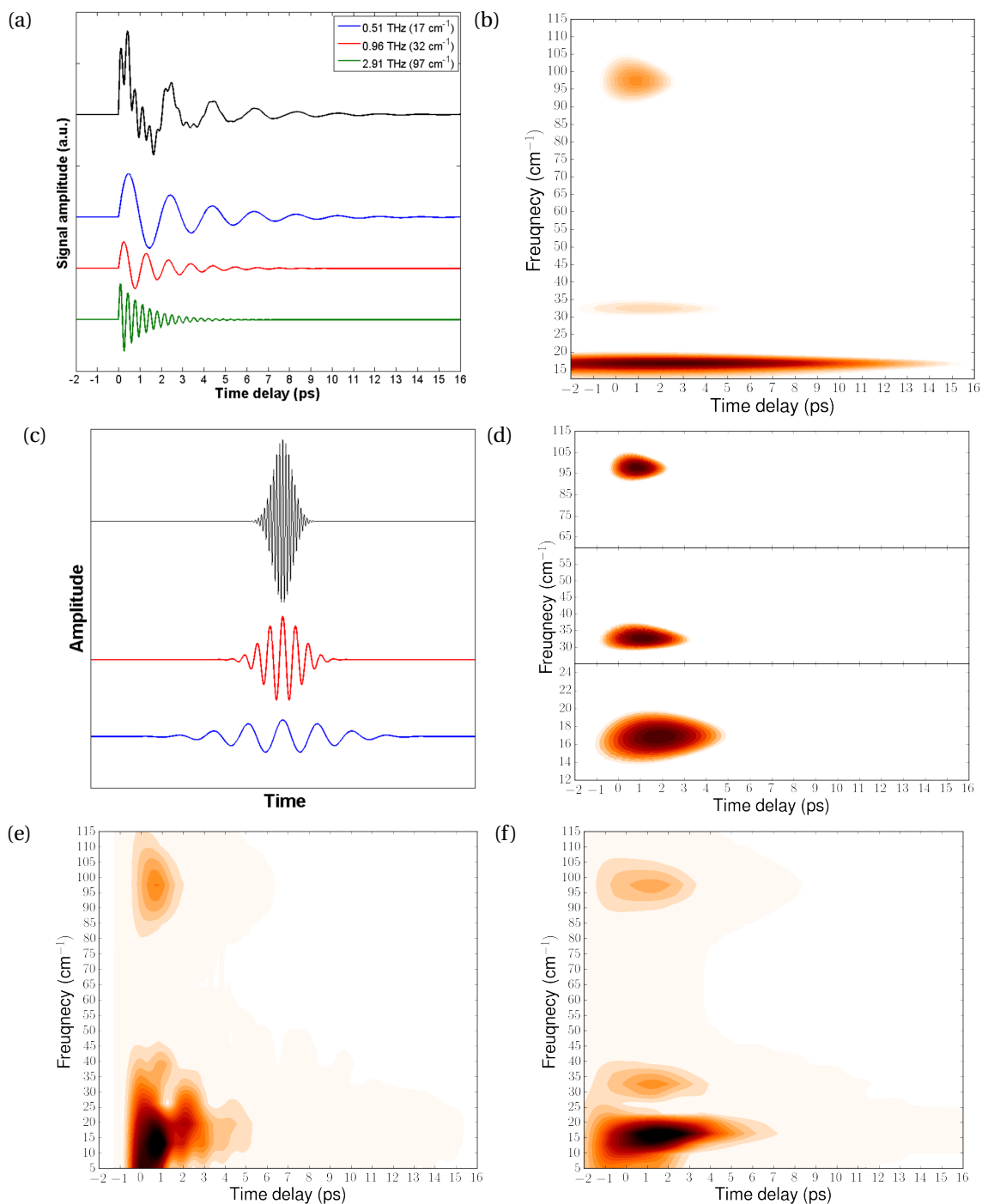
Figure C.2: (a) Test signal with three distinct frequency components as plotted separately for benchmarking frequency analysis methods. (b) Scalogram showing the full frequency range analyzed using a single complex Morlet wavelet. (c) Three distinct complex Morlet wavelets (only the real parts are plotted here) used in analyzing each frequency range in (d), where the scalograms for these regions are plotted separately. In addition, spectrogram generated from STFT of the signal in (a) using a short and long window is plotted in (e) and (f), respectively.

114

the low-frequency components usually last longer (so a relatively poor temporal resolution is tolerable) while the high frequency ones shorter (so one needs a better time resolution). Wavelets are, therefore, well-adapted for this type of signal [137].

C.3 Discussion and test analysis

In general ultrafast optical pump-probe signals are less oversampled than NMR or audio signals, which are generated at much lower frequencies. Oversampling is characterized by the ratio of sampling frequency over the Nyquist frequency of the oscillatory signal. This characteristic limits the frequency resolution of optical pump-probe experiments, so care needs to be taken in accounting for the frequencies observed in such experiments.

In the solid state pump-probe data presented in Chapter 3, a broad range of frequencies from 10 cm^{-1} to higher than 120 cm^{-1} were detected. This makes CWT the more favorable method for the analysis compared with STFT, which works better with a small frequency range. However, due to the great difference in the amplitudes associated with different frequencies and the level of noise in the signal, it's hard to visualize all frequency components in a single spectrogram or scalogram. For these reasons, in this thesis a hybrid approach has been adopted for presentation. In Fig. 3.10, 3.11 and 3.12 of section 3.2.5, three different complex Morlet wavelets and two Tukey windows of different widths are used to locate different regions of frequencies. This approach improves CWT's issue of frequency resolution at high frequencies, while taking full advantage of its nonlinear frequency scaling to discern the low frequency components, which is a main feature in the observed TA traces. For STFT, the onset of a frequency component is correlated with and affected by the chosen window size, in practice, each trace is padded with zeros of half the size of the window in the beginning and at the end of the detrended trace before the STFT procedure to reduce this effect.

D Computer program development and code snippets

D.1 Chopper noise removal algorithm

Measurements performed at low repetition rate are affected by various types of instrumental noise, one of such is the mechanical instability of the chopper, which occasionally causes the temporary blocking of laser beam or the misregistration of the pump-on and pump-off spectra/image frames. For samples with slow recovery, this scenario can be hard to avoid. The situation in shot-by-shot recorded optical pump-probe experiments and in electron diffraction experiments limited by a much slower 2D CCD camera are very different. Therefore two outlier rejection scheme were employed to remove such known error from experimental data.

D.1.1 In optical pump-probe spectroscopy

The optical pump-probe setup was designed to enable single-shot detection scheme that minimize the noise [145]. In the two-chopper detection scheme (see Fig. 3.4a) the pump chopper is triggered from an optically converted signal from the main chopper. Since the scans corrupted by the chopper errors can be immediately found by looking at the registered pump power at each shot. The mathematical problem boils down to identifying outliers in a bimodal distribution (pump power record contains in an alternating sequence of both pump-on and pump-off photodiode voltage readings).

116

The chopper noise doesn't change the mean of the voltage sequence, but modifies the distribution of the separate pump-on and pump-off readings, so one can use this parameter to identify the outliers. To pick out and eliminate the single-shot spectral data having abnormal pump power values from the data matrix *shotData*[1], the following algorithm (in pseudocode) can be used,

$mPower \leftarrow mean(pumpPower)$ ▷ Calculate the mean pump power

$n \leftarrow length(pumpPower)$ ▷ Calculate the number of shots

for $i \leftarrow 1, n$ **do** ▷ Collect the on and off pump power records

    if $pumpPower[i] \geqslant mPower$ **then**

       $highPower \leftarrow pumpPower[i]$

    else

       $lowPower \leftarrow pumpPower[i]$

    end if

end for

$poffPower \leftarrow winsorize(lowPower)$

$ponPower \leftarrow winsorize(highPower)$

$baseUpBnd \leftarrow basePower + baseThreshold * mPower$

$baseLoBnd \leftarrow basePower - baseThreshold * mPower$

$peakLoBnd \leftarrow peakPower - peakThreshold * mPower$

for $j \leftarrow 1, \frac{n}{2}$ **do** ▷ Pick out the corrupted shots by their pump powers

    if $currPower > mPower$ **and** $currPower < peakLoBnd$ **then**

       $shotData[2 * j, -1] \leftarrow -10$

       $shotData[2 * j + 1, -1] \leftarrow -10$

    else if $currPower > mPower$ **and** $currPower \geqslant peakLoBnd$ **then**

       $nextPower \leftarrow pumpPower[2 * j + 1]$

---

[1]The last column of the *shotData* matrix contains the voltage reading, the rest columns contain 1D spectra at different time delays.

```
    if nextPower < mPower and nextPower > baseUpBnd then
        shotData[2 * j, −1] ← −10
        shotData[2 * j + 1, −1] ← −10
    end if
  else if currPower < mPower and (currPower > baseUpBnd or currPower < baseLoBnd then
        shotData[2 * j, −1] ← −10
        shotData[2 * j + 1, −1] ← −10
  else if currPower < mPower and (baseLoBnd < currPower < baseUpBnd then
        nextPower ← pumpPower[2 * j + 1]
        if nextPower > mPower and nextPower < peakLoBnd then
            shotData[2 * j, −1] ← −10
            shotData[2 * j + 1, −1] ← −10
        end if
    end if
  end for
```

The value of -10 set for the pump power for each corrupted pump-probe pair is arbitrary. It's used here only to distinguish them from the uncorrupted data, so that after sieving through the for loop the cleaned data can be simply extracted by picking out those rows whose last entries are not -10. An example before and after cleaning the chopper error is shown in Fig. D.1. In practical experience, the way of setting the rejection threshold using a function of the mean has proven to have little or no effect on the uncorrupted data compared with using statistical significance (i.e. rejection of pump powers with less than 2σ significance). This is due to the limited number of data averaged for a single time delay as well as the not-very-uncommon slow drift[2] of pump power within the data collection time at one time point, which can cause

---

[2]This is affected by the temperature and humidity conditions in the lab, the air-conditioning system has been malfunctioning or non-functioning for some time during the limited weeks the data were recorded.

noticeable deviation from a normal distribution. The slow drift can be reduced by taking a smaller number of averages, usually 1000 shots of pump-on and pump-off sequence is chosen with a 250 Hz probe, this amounts to a recording time of ~ 5s.

(a)

(b)
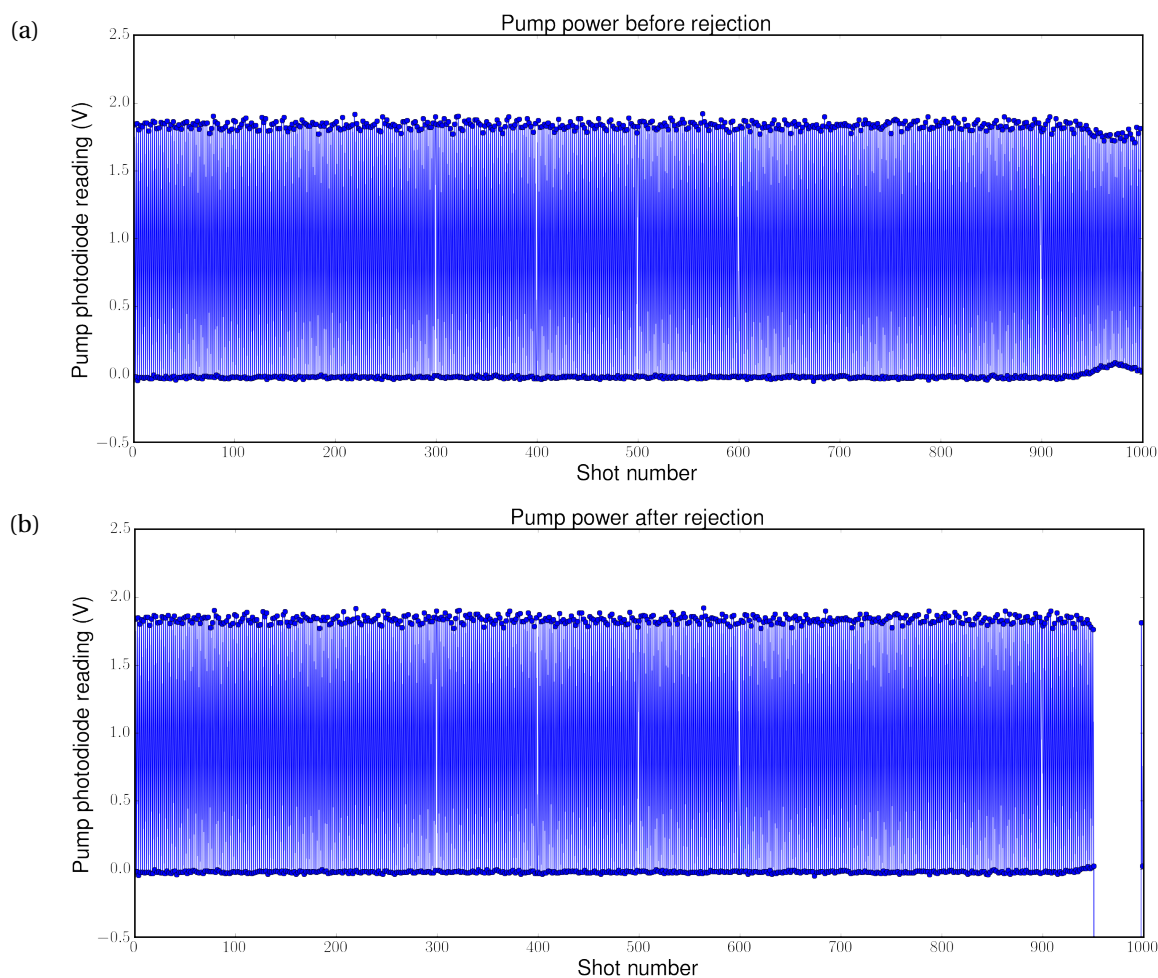
Figure D.1: The recorded pump power in a 1000-shot pump-on and pump-off sequence is cleaned of chopper error using the rejection and re-averaging algorithm described in D.1.1. The pump powers (a) before and (b) after cleaning of chopper error are compared.

D.1.2   In ultrafast electron diffraction

In electron diffraction experiment, the pump power was not monitored shot by shot. The slow Princeton Instruments CCD camera triggers the shutter to control the pump-on and pump-off cycle after the chopper. Regarding these issues, an outlier rejection

scheme using Chauvenet's criterion [146] was employed. It rejects a value x_i if,

$$N \cdot \text{erfc}(\frac{x_i - \mu}{\sigma}) < \frac{1}{2} \tag{D.1}$$

where N is the number of measurements and μ and σ are the mean and the standard deviation of the set of measurements, $\{x_i\}$.

D.2 Peak-finding in static electron diffraction patterns

Finding the precise center locations of a large number of diffraction peaks in the rotation series is crucial to indexing the diffraction patterns with very low symmetry. For TBAT the symmetry group is only P$\bar{1}$, therefore it has only one inversion center more than the lowest symmetry P1. This presents a challenge in finding a reasonably good starting point (somewhat close to the true orientation) for 2D pattern fitting described in section 3.3.4. The other requirement is that the peaks found need to be from all areas of the diffraction pattern. In fact, the higher the resolution of the peak (peaks further away from the beam center), the more it helps to precisely define the orientation. However, these peaks are usually much dimmer than those close to the center and are prone to be connected peaks. This requires to go much further than ranking the intensities as in identifying peaks in an X-ray diffraction pattern. Furthermore, in actuality, diffraction peaks rarely have a Gaussian profile due to physical limitations such as low detector counts, electron beam quality, sample quality, etc. In addition, the fiber edges imaged onto the detector and the occasional appearance of hot pixels can cause misidentification of the true peak positions. Therefore the more efficient way to locate the center of a peak is to smooth out a ROI before fitting to a 2D Gaussian function. The fitting procedure is summarized as follows,

(1) **Center blocking:** Pick out the beam center position by hand and replace the values of an elliptical or circular beam area by 0.

(2) **Image slicing:** Divide the diffraction pattern into n small rectangular or square

regions according to a grid. The size of each divided region should contain about one peak or no peak at all. This is not hard to decide and one can use a well-shaped peak for estimation.

(3) **Intensity ranking:** Calculate the sum of intensity counts within each block and pick the most intense m ($m \leq n$) blocks. Then record the row and column positions of the brightest pixel in the m brightest blocks.

(4) **Sieving by adjacency:** Calculate the closeness of the brightest pixel positions obtained from the last step with respect to each other. Discard the peaks that are too close to each other (always keep only the brighter one).
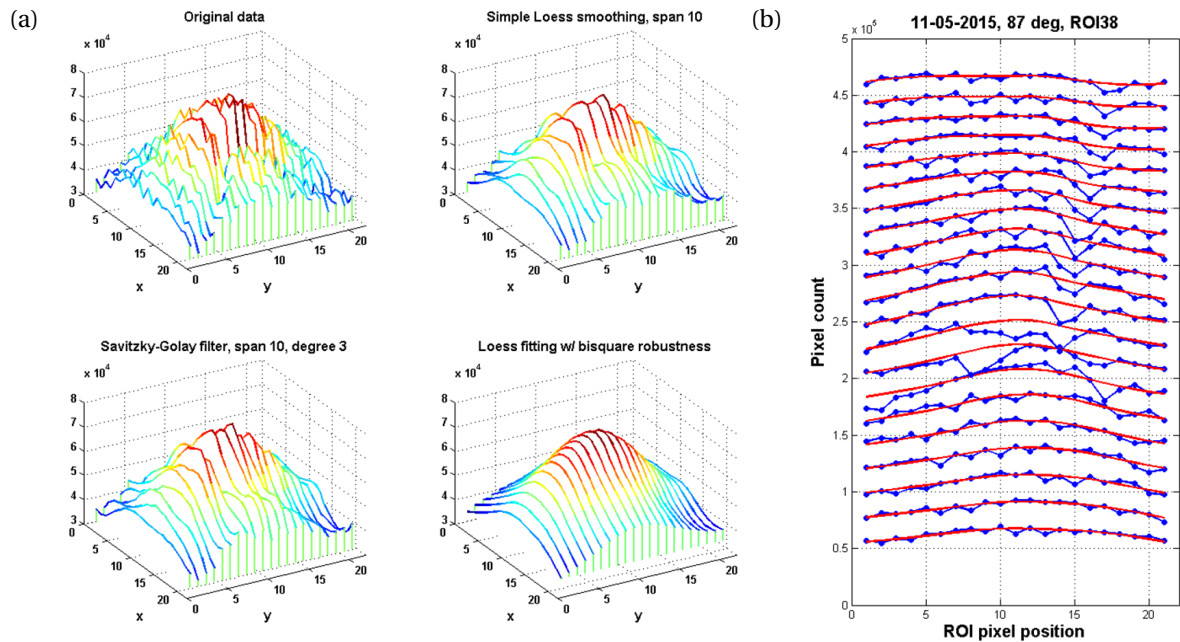
Figure D.2: Demonstration of the effectiveness of smoothing with LOESS and bisquare robustness to a diffraction peak region intercepted by three fiber edges of the fiber coupler. In (a) the results with a robust LOESS is compared with the those from a convolution-based Savitzky-Golay algorithm and from simple LOESS fitting without robustness setting. (b) Line cuts (blue) of the diffraction peak region of interest with overlaid smoothed curves (red) obtained from the robust LOESS procedure in (a).

(5) **Sieving by fitting and center position refinement:** Re-select every area centered around the peak position with similar size as one used in step 2 and use LOESS to smooth out the spatial noise. Then fit each diffraction peak matrix by a 2D Gaussian

121

of the form,

$$f(A, a, b, \sigma_x, \sigma_y) = A \exp\left[-\frac{(x-a)^2}{2\sigma_x^2} - \frac{(y-b)^2}{2\sigma_x^2}\right] + c \qquad (D.2)$$

Alternatively, a 2D Gaussian in the polar coordinates can also be used for fitting. The refined center positions and peak intensities are then readily obtained from the fitting parameters (a, b, and A).

The last step can be re-run one or two times to improve the center positions (mostly for the weak or partially overlapping peaks). Usually the success rate of finding the real peak center is above 95% after two rounds of fitting. The rest few peaks, if any, are usually highly overlapping ones that can easily be discarded by hand-picking. The LOESS fitting is very instrumental to the success of the peak-finding routine because of the erratic shape of the peaks. An example of the effect of smoothing can be found in Fig. D.2.

D.3   Standalone CCD graphic user interface (GUI)

A standalone program was developed for running the same Hamamatsu CCD and electronic board operational in the lab in Toronto (Dr. Ryan Field's setup) and in Hamburg. Fig. D.3 shows the later version used in Hamburg named *Whiteout*. It incorporates the basic functionalities of the commercial program provided by Hamamatsu (i.e. adjusting various settings for the CCD and recording spectra) with spectrum calibration, which includes a 1D peak finding algorithm and a polynomial fitting routine. The calibrated spectrum can be exported to other pump-probe programs (e.g. *Confetti*, developed for spectrally resolve pump-probe experiments) before measurement.
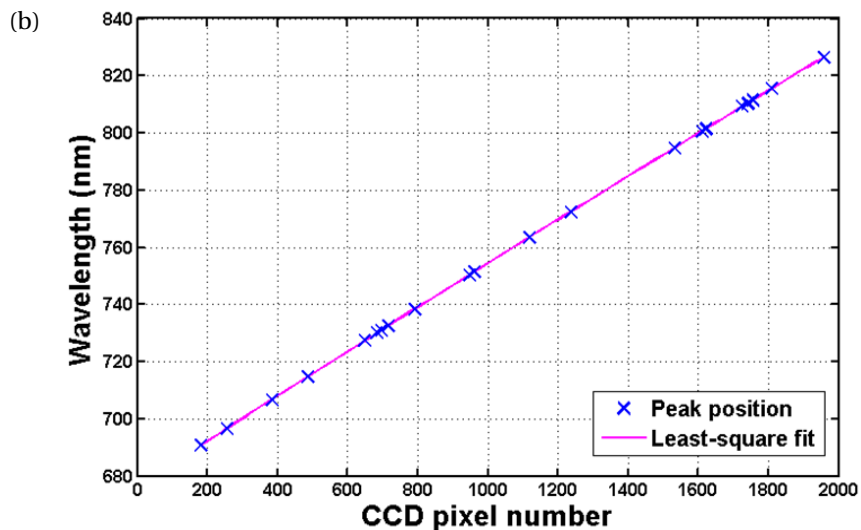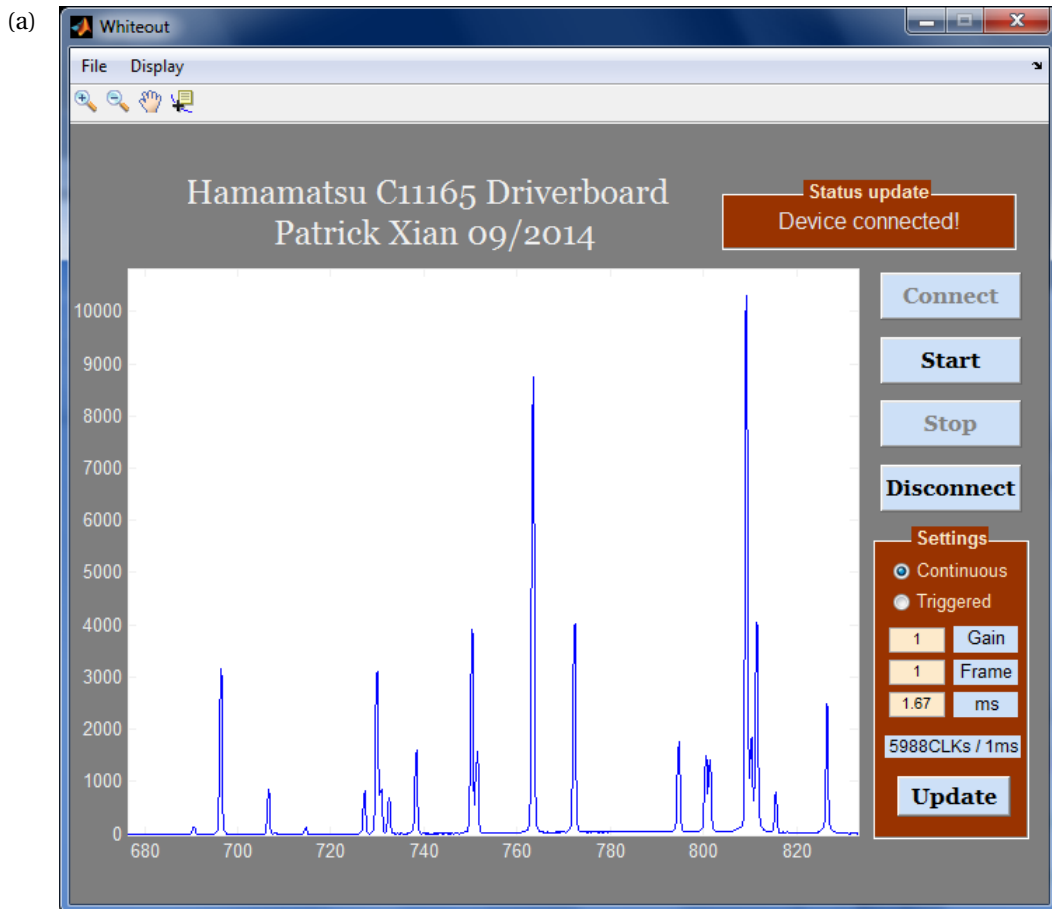
Figure D.3: (a) GUI of the spectrometer program *Whiteout*. Here shows a spectrum of the Hg/Ar light source (AvaLight-CAL) in the region 640-840 nm calibrated using the built-in functionality of the program. The horizontal axis represents wavelength, the vertical axis displays counts. (b) Spectral calibration curve in the near-IR region taking into account the second- and third-order lines of the Hg/Ar calibration source. The peak positions corresponds to the ones shown in (a).

E Quantum chemical calculations

The calculations in this section were performed by Prof. Carole Morrison and Dr. David Rogers, in solid state TBAT and in gas phase $I_2^{-\bullet}$, I_3^- and $I_4^{-\bullet}$. They are appended here to support and supplement discussions made in the main text of the thesis.

The gas-phase calculations of molecular normal modes employed density functional theory (DFT) in Gaussian and complete active space self-consistent field (CASSCF) method in GAMESS[1]. The DFT calculation (Table E.1) was carried out at the PBEPBE/SDB-aug-cc-pVTZ level, employing the PBE exchange and correlation functionals [147, 148], and the SDB-aug-cc-pVTZ as an effective core potential (ECP) [149]. The selected ECP is an augmented basis set of triple-zeta plus polarization quality with a 46-electron core ([Kr]$4d^{10}$) and seven valence electrons ($5s^2 5p^5$) for each iodine atom. The symmetry is D_{2h} for the optimized minimum energy structures. The CASSCF calculations used a SBKJC [150] ECP double-zeta basis set augmented with a set of Cartesian d-type polarization functions and a set of s- and p-type diffuse functions for each iodine atom. The SBKJC basis set for an iodine atom has a 46-electron core with the seven 5th-row valence electrons explicitly described by double-zeta quality s- and p-type functions. Following [15], C_{2h} symmetry was employed, where the ^1A_g, ^3B_u and ^1A_u states correspond, respectively, to the $^1\Sigma_g$, $^3\Pi_u$

---

[1]The Gaussian 09 Revision A.02 was used in the calculations; the GAMESS program was in version 1, May, 2012 (R2)

and $^1\Sigma_u$ states of I$^1\Sigma_u$. The $^1\Sigma_g \rightarrow^3 \Pi_u$ and $^1\Sigma_g \rightarrow^3 \Pi_u$ transitions form the C and D absorption bands of I$_3^-$ (see Fig. 2.1b). An active space of 16 electrons in nine orbitals was employed for the ground state, ^1A_g, and active spaces of two electrons in two orbitals were employed for the ^3B_u and ^1A_u excited states. For the ^3B_u state the two orbitals have irreducible representations b$_g$ (y-axis) and a$_u$ (z-axis); for ^1A_u the orbitals have irreducible representations a$_g$ (z-axis) and a$_u$ (z-axis). The CASSCF results are shown in Table E.2.

The solid state calculation was performed in CASTEP 8.0, using the PBE functionals [147, 148] and Tkatchenko-Scheffler dispersion correction scheme [151]. Norm-conserving "recpot" pseudopotentials were used for each element. Geometry optimization starting from the "Brotherton structure" [103] was carried out for the atomic positions and unit cell vectors simultaneously within the P$\overline{1}$ space group, using the Broyden–Fletcher–Goldfarb–Shanno (BFGS) method. The resulting structure was used to compute the density of states (DOS) and partial DOS for the I$_3^-$ moieties. To speed up the phonon mode calculation, the C, N, and H atoms (those that comprise the cation TBA$^+$) were fixed at equilibrium geometries. This approach also isolates the I$_3^-$ motions, which dominate the lattice response at low frequencies (i.e. < 150 cm^{-1}) upon photoexcitation. The modes calculated at the Γ-point were given assignments from visual inspection via Jmol. The results are presented in Table E.3.

Table E.1: Normal mode calculations for ground-state I_n^- (n = 2, 3, 4)
at the PBEPBE/SDB-aug-cc-pVTZ level of theory

Normal Mode	Symmetry	Wavenum. (cm^{-1})	IR Intensity
$I_2^{-\bullet}$ ($^2\Sigma_u$, E = -22.9791733 au, R = 3.2906 Å)			
1	Σ_g	91.9870	0.0
I_3^- ($^1\Sigma_g$, E = -34.4642322 au, R = 2.9778 Å, θ = 180.0°)			
1	Π_u	54.2924	0.0450
2	Π_u	54.2924	0.0450
3	Σ_g	106.6138	0.0
4	Σ_u	141.5514	87.7115
$I_4^{-\bullet}$ ($^2\Sigma_g$, E = -45.9028867 au, $R_{12} = R_{34}$ = 2.99 Å, R_{23} = 3.07 Å, θ = 180.0°)			
1	Π_g	70.4559i	0.0
2	Π_u	18.6568	0.0403
3	Σ_g	70.4581	0.0
4	Σ_u	103.5002	55.2295
5	Σ_g	133.0173	0.0

Table E.2: Normal mode calculations for ground- and excited-state I_3^- using CASSCF

Normal Mode	Symmetry	Wavenum. (cm^{-1})	IR Intensity (Debye^{2}amu·Å^2)
Ground state ^1A_g (E = -33.799170 au, R = 3.008 Å)			
1	b_u	58.346	0.0061
2	b_u	58.346	0.0061
3	a_g	106.101	0.0
4	a_u	121.998	6.2412
Excited state ^3B_u (E = -33.709513 au, R = 4.270 Å)			
5	b_u	8.253	0.0184
6	b_u	9.445	0.0176
7	a_g	16.491	0.0
8	a_u	20.560	0.5501
Excited state ^1A_u (E = -33.707366 au, R = 5.131 Å)			
9	a_u	14.899i	0.1412
10	b_u	5.180	0.0245
11	b_u	5.181	0.0245
12	a_g	9.200	0.0
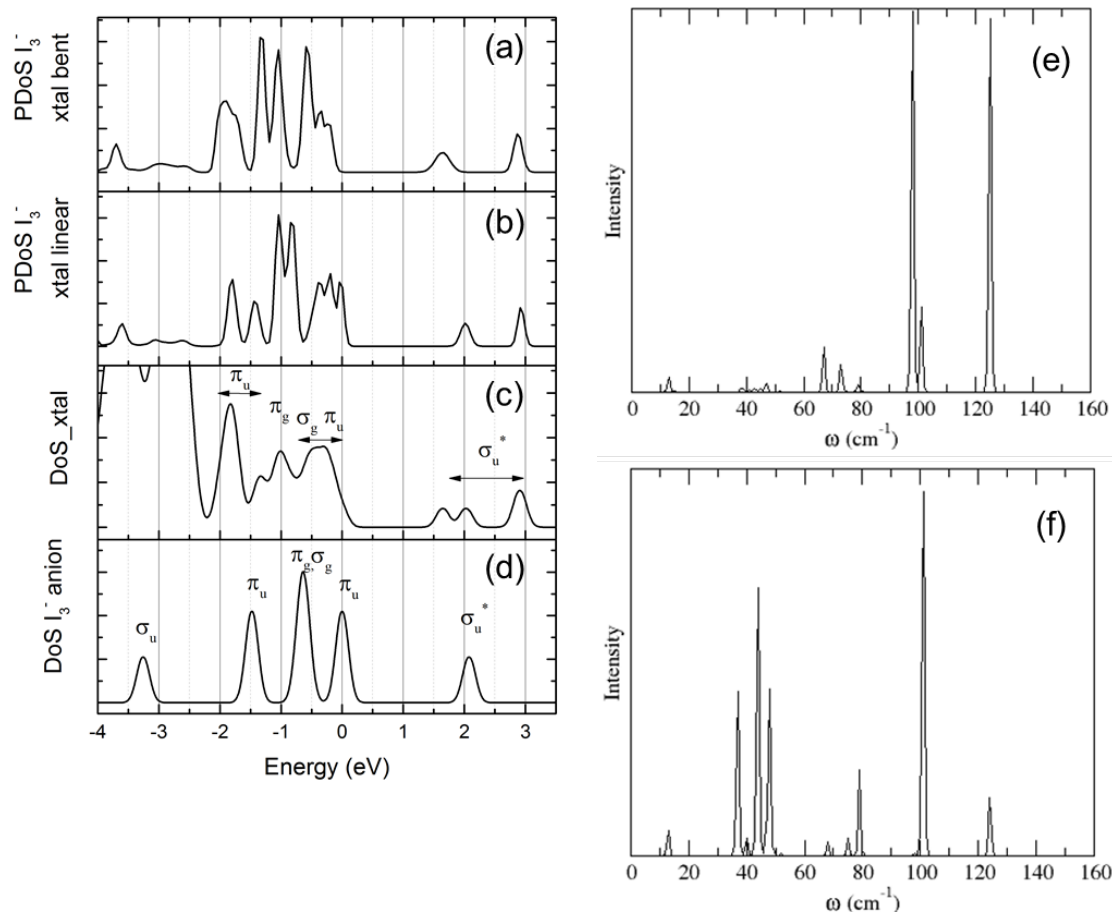
Figure E.1: Calculated partial density of states (PDOS) for (a) the bent and (b) the straight I_3^- moieties in the TBAT unit cell. The combined DOS of all atoms in the unit cell is shown in (c). The molecular orbital labels of (a) and (b) follow that in (c). The solid-state DOS exhibit energy shifts with respect to the gas-phase results in (d), in which the energy origin is aligned with the Fermi surface of the solid-state calculations. Phonon mode calculation yields the (e) IR-active and (f) Raman-active modes of I_3^- in TBAT unit cell. The intensities are scaled arbitrarily in each plot, and the frequencies and mode characters are tabulated in Table E.3.

Appendix E. Quantum chemical calculations

Table E.3: Γ-point phonon modes of I_3^- in TBAT

No.	Wavenum. (cm^{-1})*	Sym-metry	Mode type	Assignment	Chain type	Remark
1	13.38	A_g	External	Translation ∥ a	Bent	
2	13.63	A_u	External	Translation ∥ a	Bent	
3	15.24	A_g	External	Translation ∥ a	Straight	
4	15.32	A_u	External	Translation ∥ a	Straight	
5	37.87	A_g	External	Translation ∥ c	Bent	
6	38.27	A_u	External	Translation ∥ c	Bent	Coupled**
7	39.77	A_g	External	Libration	Straight	Coupled
8	40.15	A_u	External	Libration	Straight	Coupled
9	41.70	A_u	External	Translation ∥ b	Straight	Coupled
10	42.62	A_g	External	Translation ∥ b	Straight	Coupled
11	43.07	A_u	External	Translation ∥ b	Bent	Coupled
12	44.03	A_g	External	Translation ∥ b	Bent	Coupled
13	44.96	A_g	External	Translation ∥ c	Straight	Coupled
14	45.05	A_u	External	Translation ∥ c	Straight	Coupled
15	47.64	A_u	External	Libration	Straight	Coupled
16	47.90	A_u	External	Libration	Bent	Coupled
17	48.09	A_g	External	Libration	Straight	Coupled
18	48.84	A_g	External	Libration	Bent	Coupled
19	52.23	A_g	External	Libration	Bent	Coupled
20	52.31	A_u	External	Libration	Bent	Coupled
21	67.94	A_u	Internal	Bending	Straight	
22	68.25	A_g	Internal	Bending	Straight	
23	73.46	A_u	Internal	Bending	Bent	
24	73.53	A_g	Internal	Bending	Bent	
25	75.70	A_g	Internal	Bending	Bent	
26	75.74	A_u	Internal	Bending	Bent	
27	79.37	A_u	Internal	Sym. stretch.	Bent	
28	79.42	A_g	Internal	Sym. stretch.	Bent	
29	80.62	A_g	Internal	Bending	Straight	
30	80.63	A_u	Internal	Bending	Straight	
31	98.29	A_g	Internal	Asym. stretch.	Bent	
32	98.34	A_u	Internal	Asym. stretch.	Bent	
33	101.59	A_u	Internal	Sym. stretch.	Straight	
34	101.59	A_g	Internal	Sym. stretch.	Straight	
35	124.85	A_g	Internal	Asym. stretch.	Straight	
36	125.02	A_u	Internal	Asym. stretch.	Straight	

* No acoustic sum rule correction was applied to the frequencies obtained from CASTEP due to symmetry breaking in the constraint optimization of the TBAT unit cell.

** Coupled modes exhibit features of (at least) two types of atomic motion. Only the dominant component is shown in the assignment column.

128

Bibliography

[1] J. Franck and E. Rabinowitsch. Some remarks about free radicals and the photo-chemistry of solutions. *Transactions of the Faraday Society*, 30, 120 (1934).

[2] E. Rabinowitch and W. C. Wood. The collison mechanism and the primary photochemical process in solutions. *Transactions of the Faraday Society*, 32, 1381, 1936.

[3] E. Rabinowitch and H. L. Lehmann. Kinetics of recombination of bromine atoms. *Transactions of the Faraday Society*, 31, 689, 1935.

[4] E. Rabinowitch and W. C. Wood. Properties of illuminated iodine solutions. I. Photochemical dissociation of iodine molecules in solution. *Transactions of the Faraday Society*, 32, 547 (1936).

[5] Benjamin J. Schwartz, Jason C. King, and Charles B. Harris. The molecular basis of solvent caging. In *Ultrafast Dynamics of Chemical Systems*, pages 235–248. Springer Netherlands, Dordrecht, 1994.

[6] Michael J. Pilling and Paul W. Seakins. *Reaction Kinetics*. Oxford University Press, 2nd edition, 1996.

[7] Raphael D. Levine. *Molecular Reaction Dynamics*. Cambridge University Press, 2009.

Bibliography

[8]   B. J. Greenblatt, M. T. Zanni, and D. M. Neumark. Photodissociation of $I_2(Ar)_n$ Clusters Studied with Anion Femtosecond Photoelectron Spectroscopy. *Science*, 276, 1675–1678 (1997).

[9]   David F. Kelley, N. Alan Abul-Haj, and Du-Jeon Jang. Geminate recombination of molecular iodine. The role of A and A′ states. *The Journal of Chemical Physics*, 80, 4105 (1984).

[10] A L Harris, J K Brown, and C B Harris. The nature of simple photodissociation reactions in liquids on ultrafast time scales. *Annual Review of Physical Chemistry*, 39, 341–366 (1988).

[11] Zhaohui Wang, Thierry Wasserman, Erez Gershgoren, Jiri Vala, Ronnie Kosloff, and Sanford Ruhman. Geminate recombination of I_3^- in cooled liquid and glassy ethanol. *Chemical Physics Letters*, 313, 155–161 (1999).

[12] Markus Gühr. Coherent Dynamics of Halogen Molecules in Rare Gas Solids. In *Coherent Vibrational Dynamics*. CRC Press, 2007.

[13] Ph. Fornier de Violet. Polyhalide radical anions as intermediates in chemistry. *Reviews of Chemical Intermediates*, 4, 121–169 (1981).

[14] Per H Svensson and Lars Kloo. Synthesis, structure, and bonding in polyiodide and metal iodide-iodine systems. *Chemical Reviews*, 103, 1649–84 (2003).

[15] André Severo Pereira Gomes, Lucas Visscher, Hélène Bolvin, Trond Saue, Stefan Knecht, Timo Fleig, and Ephraim Eliav. The electronic structure of the triiodide ion from relativistic correlated calculations: A comparison of different methodologies. *The Journal of Chemical Physics*, 133, 064305, 2010.

[16] Thomas Kühne, Renate Küster, and Peter Vöhringer. Femtosecond photodissociation of triiodide in solution: Excitation energy dependence and transition state dynamics. *Chemical Physics*, 233, 161–178 (1998).

[17] Alexandra A Hoops, Jason R Gascooke, Ann Elise Faulhaber, Kathryn E Kautzman, and Daniel M Neumark. Two- and three-body photodissociation of gas phase I_3^-. *The Journal of Chemical Physics*, 120, 7901–9 (2004).

[18] Ryuzo Nakanishi, Naoya Saitou, Tomoyo Ohno, Satomi Kowashi, Satoshi Yabushita, and Takashi Nagata. Photodissociation of gas-phase I_3^-: comprehensive understanding of nonadiabatic dissociation dynamics. *The Journal of Chemical Physics*, 126, 204311 (2007).

[19] Uri Banin, Amir Waldman, and Sanford Ruhman. Ultrafast photodissociation of I_3^- in solution: Direct observation of coherent product vibrations. *The Journal of Chemical Physics*, 96, 2416, 1992.

[20] Martin T. Zanni, B. Jefferys Greenblatt, Alison V. Davis, and Daniel M. Neumark. Photodissociation of gas phase I_3^- using femtosecond photoelectron spectroscopy. *The Journal of Chemical Physics*, 111, 2991 (1999).

[21] Hyeon Choi, Ryan T. Bise, Alexandra A. Hoops, and Daniel M. Neumark. Photodissociation dynamics of the triiodide anion (I_3^-). *The Journal of Chemical Physics*, 113, 2255 (2000).

[22] Lei Zhu, Kazutaka Takahashi, Morihisa Saeki, Tatsuya Tsukuda, and Takashi Nagata. Photodissociation of gas-phase I_3^-: product branching in the visible and UV regions. *Chemical Physics Letters*, 350, 233–239 (2001).

[23] Alan E. Johnson and Anne B. Myers. Solvent Effects in the Raman Spectra of the Triiodide Ion: Observation of Dynamic Symmetry Breaking and Solvent Degrees of Freedom. *The Journal of Physical Chemistry*, 100, 7778–7788 (1996).

[24] F S Zhang and R M Lynden-Bell. Solvent-induced symmetry breaking. *Physical Review Letters*, 90, 185505 (2003).

[25] Peter Roland Poulin. *Coherent lattice and molecular dynamics in ultrafast single-shot spectroscopy.* PhD thesis, Massachusetts Institute of Technology, 2005.

[26] P. R. Poulin and Keith A Nelson. Irreversible Organic Crystalline Chemistry Monitored in Real Time. *Science*, 313, 1756–1760, 2006.

[27] Christopher G Elles and F Fleming Crim. Connecting chemical dynamics in gases and liquids. *Annual Review of Physical Chemistry*, 57, 273–302 (2006).

[28] Xiyi Chen and Stephen E. Bradforth. The Ultrafast Dynamics of Photodetachment. *Annual Review of Physical Chemistry*, 59, 203–231 (2008).

[29] NIST. Iodine, NIST Chemistry Web Book.

[30] Kyung Hwan Kim, Hosung Ki, Key Young Oang, Shunsuke Nozawa, Tokushi Sato, Joonghan Kim, Tae Kyu Kim, Jeongho Kim, Shin-ichi Adachi, and Hyotcherl Ihee. Global Reaction Pathways in the Photodissociation of I_3^- Ions in Solution at 267 and 400 nm Studied by Picosecond X-ray Liquidography. *ChemPhysChem*, 14, 3687–3697 (2013).

[31] Kyung Hwan Kim, Jae Hyuk Lee, Joonghan Kim, Shunsuke Nozawa, Tokushi Sato, Ayana Tomita, Kouhei Ichiyanagi, Hosung Ki, Jeongho Kim, Shin-ichi Adachi, and Hyotcherl Ihee. Solvent-Dependent Molecular Structure of Ionic Species Directly Measured by Ultrafast X-Ray Solution Scattering. *Physical Review Letters*, 110, 165505 (2013).

[32] Brian P Molesky, Paul G Giokas, Zhenkun Guo, and Andrew M Moran. Multidimensional resonance Raman spectroscopy by six-wave mixing in the deep UV. *The Journal of Chemical Physics*, 141, 114202 (2014).

[33] Zhenkun Guo, Brian P Molesky, Thomas P Cheshire, and Andrew M Moran. Elucidation of reactive wavepackets by two-dimensional resonance Raman spectroscopy. *The Journal of Chemical Physics*, 143, 124202 (2015).

[34] John N. Bradley. *Fast reactions.* Clarendon Press, 1975.

[35] Graham R. Fleming. *Chemical applications of ultrafast spectroscopy.* Oxford University Press, 1986.

[36] R. R. Alfano and S. L. Shapiro. Observation of Self-Phase Modulation and Small-Scale Filaments in Crystals and Glasses. *Physical Review Letters*, 24, 592–594 (1970).

[37] Robert R. Alfano. *The Supercontinuum Laser Source: The Ultimate White Light.* Springer, 2016.

[38] U. Megerle, I. Pugliesi, C. Schriever, C. F. Sailer, and E. Riedle. Sub-50 fs broadband absorption spectroscopy with tunable excitation: putting the analysis of ultrafast molecular dynamics on solid ground. *Applied Physics B*, 96, 215–231 (2009).

[39] S. A. Kovalenko, A. L. Dobryakov, J. Ruthmann, and N. P. Ernsting. Femtosecond spectroscopy of condensed phases with chirped supercontinuum probing. *Physical Review A*, 59, 2369–2384 (1999).

[40] W T Pollard and R A Mathies. Analysis of Femtosecond Dynamic Absorption Spectra of Nonstationary States. *Annual Review of Physical Chemistry*, 43, 497–523 (1992).

[41] Peter Hamm. Principles of Nonlinear Optical Spectroscopy : A Practical Approach or Mukamel for Dummies. *University of Zurich*, 2005.

[42] Lisa Dhar, John A. Rogers, and Keith A. Nelson. Time-resolved vibrational spectroscopy in the impulsive limit. *Chemical Reviews*, 94, 157–193 (1994).

[43] Ivo H.M. van Stokkum, Delmar S. Larsen, and Rienk van Grondelle. Global and target analysis of time-resolved spectra. *Biochimica et Biophysica Acta (BBA) - Bioenergetics*, 1657, 82–104 (2004).

[44] H. Rabitz, R de Vivie-Riedle, M Motzkus, and K Kompa. Whither the Future of Controlling Quantum Phenomena? *Science*, 288, 824–828 (2000).

[45] Constantin Brif, Raj Chakrabarti, and Herschel Rabitz. Control of quantum phenomena: past, present and future. *New Journal of Physics*, 12, 075008 (2010).

[46] Elmar Schreiber. *Femtosecond Real-Time Spectroscopy of Small Molecules and Clusters*. Springer, 1998.

[47] RS Judson and H Rabitz. Teaching lasers to control molecules. *Physical review letters*, 68, 1500–1503 (1992).

[48] T Brixner, N H Damrauer, P Niklaus, and G Gerber. Photoselective adaptive femtosecond quantum control in the liquid phase. *Nature*, 414, 57–60 (2001).

[49] Valentyn I Prokhorenko, Andrea M Nagy, Stephen A Waschuk, Leonid S Brown, Robert R Birge, and R J Dwayne Miller. Coherent control of retinal isomerization in bacteriorhodopsin. *Science*, 313, 1257–61 (2006).

[50] Tobias Brixner, Niels H. Damrauer, and Gustav Gerber. Femtosecond Quantum Control. In *Advances In Atomic, Molecular, and Optical Physics*, volume 46, pages 1–54. 2001.

[51] Marcos Dantus and Vadim V. Lozovoy. Experimental Coherent Laser Control of Physicochemical Processes. *Chemical Reviews*, 104, 1813–1860 (2004).

[52] G. Cerullo, C.J. Bardeen, Q. Wang, and C.V. Shank. High-power femtosecond chirped pulse excitation of molecules in solution. *Chemical Physics Letters*, 262, 362–368 (1996).

[53] A. M. Weiner. Femtosecond pulse shaping using spatial light modulators. *Review of Scientific Instruments*, 71, 1929 (2000).

[54] Andrew M. Weiner. Ultrafast optical pulse shaping: a tutorial review. *Optics Communications*, 284, 3669–3692 (2011).

[55] Jakob Juul Larsen, Ida Wendt-Larsen, and Henrik Stapelfeldt. Controlling the Branching Ratio of Photodissociation Using Aligned Molecules. *Physical Review Letters*, 83, 1123–1126 (1999).

[56] A Assion, T Baumert, M Bergt, T Brixner, B Kiefer, V Seyfried, M Strehle, and G Gerber. Control of Chemical Reactions by Feedback-Optimized Phase-Shaped Femtosecond Laser Pulses. *Science*, 282, 919–922 (1998).

[57] G. P. Thomson and A. Reid. Diffraction of cathode rays by a thin film. *Nature*, 119, 890–890 (1927).

[58] C. Davisson and L. H. Germer. The scattering of electrons by a single crystal of nickel. *Nature*, 119, 558–560 (1927).

[59] Richard K. Gehrenbeck. Electron diffraction: fifty years ago. *Physics Today*, 31, 34 (1978).

[60] Douglas L. Dorset. Electron crystal structure analysis of small organic molecules. *Journal of Electron Microscopy Technique*, 2, 89–128, 1985.

[61] D.L. Dorset. *Structural Electron Crystallography*. Springer, 1995.

[62] Zhong-lin Wang. *Elastic and Inelastic Scattering in Electron Diffraction and Imaging*. Springer, 1995.

[63] David B. Williams and C. Barry Carter. *Transmission Electron Microscopy: A Textbook for Materials Science*. Springer, 2009.

[64] Werner Massa. *Crystal Structure Determination*. Springer, 2004.

[65] Gerard Mourou and Steve Williamson. Picosecond electron diffraction. *Applied Physics Letters*, 41, 44 (1982).

[66] S. Williamson, G. Mourou, and J. C. M. Li. Time-Resolved Laser-Induced Phase Transformation in Aluminum. *Physical Review Letters*, 52, 2364–2367 (1984).

Bibliography

[67] Bradley J Siwick, Jason R Dwyer, Robert E Jordan, and R J Dwayne Miller. An atomic-level view of melting using femtosecond electron diffraction. *Science*, 302, 1382–5 (2003).

[68] Richard Henderson. The potential and limitations of neutrons, electrons and X-rays for atomic resolution microscopy of unstained biological molecules. *Quarterly Reviews of Biophysics*, 28, 171 (2009).

[69] Maximilian Eichberger, Hanjo Schäfer, Marina Krumova, Markus Beyer, Jure Demsar, Helmuth Berger, Gustavo Moriena, Germán Sciaini, and R J Dwayne Miller. Snapshots of cooperative atomic motions in the optical suppression of charge density waves. *Nature*, 468, 799–802 (2010).

[70] Meng Gao, Cheng Lu, Hubert Jean-Ruel, Lai Chung Liu, Alexander Marx, Ken Onda, Shin-ya Koshihara, Yoshiaki Nakano, Xiangfeng Shao, Takaaki Hiramatsu, Gunzi Saito, Hideki Yamochi, Ryan R. Cooney, Gustavo Moriena, Germán Sciaini, and R. J. Dwayne Miller. Mapping molecular motions leading to charge delocalization with ultrabright electrons. *Nature*, 496, 343–346 (2013).

[71] Tzong-Ru T Han, Faran Zhou, Christos D Malliakas, Phillip M Duxbury, Subhendra D Mahanti, Mercouri G Kanatzidis, and Chong-Yu Ruan. Exploration of metastability and hidden phases in correlated electron crystals visualized by femtosecond optical doping and electron crystallography. *Science Advances*, 1, e1400173 (2015).

[72] T. Ishikawa, S. A. Hayes, S. Keskin, G. Corthey, M. Hada, K. Pichugin, A. Marx, J. Hirscht, K. Shionuma, K. Onda, Y. Okimoto, S.-y. Koshihara, T. Yamamoto, H. Cui, M. Nomura, Y. Oshima, M. Abdel-Jawad, R. Kato, and R. J. D. Miller. Direct observation of collective modes coupled to molecular orbital-driven charge transfer. *Science*, 350, 1501–1505 (2015).

[73] C Mueller, A Marx, S W Epp, Y Zhong, A Kuo, A R Balo, J Soman, F Schotte, H T Lemke, R L Owen, E F Pai, A R Pearson, J S Olson, P A Anfinrud, O P Ernst, and

136

R J Dwayne Miller. Fixed target matrix for femtosecond time-resolved and in situ serial micro-crystallography. *Structural Dynamics*, 2, 054302 (2015).

[74] G H Kassier, K Haupt, N Erasmus, E G Rohwer, H M von Bergmann, H Schwoerer, S M M Coelho, and F D Auret. A compact streak camera for 150 fs time resolved measurement of bright pulses in ultrafast electron diffraction. *Review of Scientific Instruments*, 81, 105103 (2010).

[75] Hubert Jean-Ruel, Meng Gao, Michal A. Kochman, Cheng Lu, Lai Chung Liu, Ryan R. Cooney, Carole A. Morrison, and R. J. Dwayne Miller. Ring-Closing Reaction in Diarylethene Captured by Femtosecond Electron Crystallography. *The Journal of Physical Chemistry B*, 117, 15894–15902 (2013).

[76] Philip Coppens, Ivan I Vorontsov, Tim Graber, Milan Gembicky, and Andrey Yu Kovalevsky. The structure of short-lived excited states of molecular complexes by time-resolved X-ray diffraction. *Acta Crystallographica. Section A, Foundations of crystallography*, 61, 162–72 (2005).

[77] Brett J. Pearson and Thomas C. Weinacht. Shaped ultrafast laser pulses in the deep ultraviolet. *Optics Express*, 15, 4385 (2007).

[78] Christian Homann. *Optical parametric processes to the extreme.* PhD thesis, Ludwig-Maximilians-Universität München, 2013.

[79] Brian O'Regan and Michael Grätzel. A low-cost, high-efficiency solar cell based on dye-sensitized colloidal TiO_2 films. *Nature*, 353, 737–740 (1991).

[80] Gerrit Boschloo and Anders Hagfeldt. Characteristics of the iodide/triiodide redox mediator in dye-sensitized solar cells. *Accounts of Chemical Research*, 42, 1819–26 (2009).

[81] James M. Gardner, Maria Abrahamsson, Byron H. Farnum, and Gerald J. Meyer. Visible Light Generation of Iodine Atoms and I−I Bonds: Sensitized I^- Oxidation

and I_3^- Photodissociation. *Journal of the American Chemical Society*, 131, 16206–16214 (2009).

[82] Thomas Kühne and Peter Vöhringer. Transient Anisotropy and Fragment Rotational Excitation in the Femtosecond Photodissociation of Triiodide in Solution. *The Journal of Physical Chemistry A*, 102, 4177–4185 (1998).

[83] Erez Gershgoren, Uri Banin, and Sanford Ruhman. Caging and Geminate Recombination following Photolysis of Triiodide in Solution. *The Journal of Physical Chemistry A*, 102, 9–16 (1998).

[84] J.H. Baxendale, P. Sharpe, and M.D. Ward. Absorption in the far red by I_2^- and Br_2^-. *International Journal for Radiation Physics and Chemistry*, 7, 587–588 (1975).

[85] Uri Banin and Sanford Ruhman. Ultrafast photodissociation of I3. Coherent photochemistry in solution. *The Journal of Chemical Physics*, 98, 4391 (1993).

[86] Yoshio Nishiyama, Masahide Terazima, and Yoshifumi Kimura. Ultrafast relaxation and reaction of diiodide anion after photodissociation of triiodide in room-temperature ionic liquids. *The Journal of Physical Chemistry B*, 116, 9023–32 (2012).

[87] Erez Gershgoren, J. Vala, R. Kosloff, and S. Ruhman. Impulsive Control of Ground Surface Dynamics of I_3^- in Solution. *The Journal of Physical Chemistry A*, 105, 5081–5095 (2001).

[88] Uri Banin, Ronnie Kosloff, and Sanford Ruhman. Femtosecond Chemical Dynamics in Solution: Photodissociation of I_3^-. *Israel Journal of Chemistry*, 33, 141–156, 1993.

[89] Alan E. Johnson and Anne B. Myers. A comparison of time- and frequency-domain resonance Raman spectroscopy in triiodide. *The Journal of Chemical Physics*, 104, 2497 (1996).

[90] Adva Baratz and Sanford Ruhman. UV photolysis of I3- in solution – Multiple product channels detected by transient hyperspectral probing. *Chemical Physics Letters*, 461, 211–217 (2008).

[91] A Barkatt and M Ottolenghi. Laser flash-photolysis of aqueous triiodide solutions. *Molecular Photochemistry*, 6, 253–261, 1974.

[92] Rick Trebino, Kenneth W. DeLong, David N. Fittinghoff, John N. Sweetser, Marco A. Krumbügel, Bruce A. Richman, and Daniel J. Kane. Measuring ultrashort laser pulses in the time-frequency domain using frequency-resolved optical gating. *Review of Scientific Instruments*, 68, 3277 (1997).

[93] Rick Trebino. *Frequency-Resolved Optical Gating: The Measurement of Ultrashort Laser Pulses.* Springer, 2012.

[94] Valentyn I. Prokhorenko, Alessandra Picchiotti, Samansa Maneshi, and R. J. Dwayne Miller. Measurement and Characterization of Sub-5 fs Broadband UV Pulses in the 230–350 nm Range. In *Ultrafast Phenomena XIX*, pages 744–748. 2015.

[95] Valentyn I Prokhorenko, Alexei Halpin, Philip J M Johnson, R J Dwayne Miller, and Leonid S Brown. Coherent control of the isomerization of retinal in bacteriorhodopsin in the high intensity regime. *The Journal of Chemical Physics*, 134, 085105 (2011).

[96] Rui Xian, Valentyn I. Prokhorenko, Ryan L. Field, and R. J. Dwayne Miller. Coherent Control of the Photodissociation of Triiodide in Solution Reveals New Pathways. In *Ultrafast Phenomena XIX*, pages 382–385. 2015.

[97] B. Jefferys Greenblatt, Martin T. Zanni, and Daniel M. Neumark. Photodissociation dynamics of the I_2^- anion using femtosecond photoelectron spectroscopy. *Chemical Physics Letters*, 258, 523–529 (1996).

[98] Thomas Kühne and Peter Vöhringer. Vibrational relaxation and geminate recombination in the femtosecond-photodissociation of triiodide in solution. *The Journal of Chemical Physics*, 105, 10788 (1996).

[99] R. G. Newton. Inverse Problems in Physics. *SIAM Review*, 12, 346–356 (1970).

[100] Herschel Rabitz and Wusheng Zhu. Optimal Control of Molecular Motion: Design, Implementation, and Inversion. *Accounts of Chemical Research*, 33, 572–578 (2000).

[101] David Avisar and David J. Tannor. Complete Reconstruction of the Wave Function of a Reacting Molecule by Four-Wave Mixing Spectroscopy. *Physical Review Letters*, 106, 170405 (2011).

[102] W. Gabes and D.J. Stufkens. Electronic absorption spectra of symmetrical and asymmetrical trihalide ions. *Spectrochimica Acta Part A: Molecular Spectroscopy*, 30, 1835–1841 (1974).

[103] Wendy S Brotherton, Ronald J Clark, and Lei Zhu. Synthesis of 5-iodo-1,4-disubstituted-1,2,3-triazoles mediated by in situ generated copper(I) catalyst and electrophilic triiodide ion. *The Journal of Organic Chemistry*, 77, 6443–55 (2012).

[104] Koichi Momma and Fujio Izumi. VESTA 3 for three-dimensional visualization of crystal, volumetric and morphology data. *Journal of Applied Crystallography*, 44, 1272–1276 (2011).

[105] Philippe Fornier de Violet, Roland Bonneau, and Jacques Joussot-Dubien. Laser flash photolysis of iodine-iodide mixture in hydroxylic solvent. Evidence for the existence of the radical anion I_4^-. *Chemical Physics Letters*, 28, 569–572 (1974).

[106] Gregory P. Wakeham and Keith A. Nelson. Dual-echelon single-shot femtosecond spectroscopy. *Optics Letters*, 25, 505 (2000).

[107] Taeho Shin, Johanna W. Wolfson, Samuel W. Teitelbaum, Maria Kandyla, and Keith A. Nelson. Dual echelon femtosecond single-shot spectroscopy. *Review of Scientific Instruments*, 85, 083115 (2014).

[108] A. Brodeur and S. L. Chin. Band-Gap Dependence of the Ultrafast White-Light Continuum. *Physical Review Letters*, 80, 4406–4409 (1998).

[109] Philip J. M. Johnson, Valentyn I. Prokhorenko, and R. J. Dwayne Miller. Stable UV to IR supercontinuum generation in calcium fluoride with conserved circular polarization states. *Optics Express*, 17, 21488 (2009).

[110] Jörg Kohl-Landgraf, Jan-Eric Nimsch, and Josef Wachtveitl. LiF, an underestimated supercontinuum source in femtosecond transient absorption spectroscopy. *Optics Express*, 21, 17060 (2013).

[111] Valentyn I Prokhorenko. Global analysis of multi-dimensional experimental data. *European Photochemistry Association Newsletter*, page 21, 2012.

[112] S. Sugai and G. Saito. Resonant Raman scattering in organic conductors α and β-(BEDT-TTF)$_2$X (X=I$_3$ and IBr$_2$). *Solid State Communications*, 58, 759–763 (1986).

[113] J. S. Zambounis, E. I. Kamitsos, A. P. Patsis, and G. C. Papavassiliou. Resonance Raman and far-infrared studies of n-Bu$_4$NI$_3$ and n-Bu$_4$NBr$_3$. *Journal of Raman Spectroscopy*, 23, 81–85 (1992).

[114] F.J. Harris. On the use of windows for harmonic analysis with the discrete Fourier transform. *Proceedings of the IEEE*, 66, 51–83, 1978.

[115] Helmut Mehrer. *Diffusion in Solids: Fundamentals, Methods, Materials, Diffusion-Controlled Processes.* Springer, 2007.

[116] A. A. Lebedeff. A focusing method for producing electron diffraction patterns. *Nature*, 128, 491–491 (1931).

Bibliography

---

[117] Jeanne Ayache, Luc Beaunier, Jacqueline Boumendil, Gabrielle Ehret, and Danièle Laub. *Sample Preparation Handbook for Transmission Electron Microscopy*. Springer, New York, NY, 2010.

[118] P.E. Maslen, J. Faeder, and R. Parson. Ab initio calculations of the ground and excited states of I_2^- and ICl^-. *Chemical Physics Letters*, 263, 63–72 (1996).

[119] Alexander S. Eggeman, Steffen Illig, Alessandro Troisi, Henning Sirringhaus, and Paul A. Midgley. Measurement of molecular motion in organic semiconductors by thermal diffuse electron scattering. *Nature Materials*, 12, 1045–1049 (2013).

[120] P Beaud, A Caviezel, S O Mariager, L Rettig, G Ingold, C Dornes, S-W Huang, J A Johnson, M Radovic, T Huber, T Kubacka, A Ferrer, H T Lemke, M Chollet, D Zhu, J M Glownia, M Sikorski, A Robert, H Wadati, M Nakamura, M Kawasaki, Y Tokura, S L Johnson, and U Staub. A time-dependent order parameter for ultrafast photoinduced phase transitions. *Nature Materials*, 13, 923–7 (2014).

[121] Vance R Morrison, Robert P Chatelain, Kunal L Tiwari, Ali Hendaoui, Andrew Bruhács, Mohamed Chaker, and Bradley J Siwick. A photoinduced metal-like phase of monoclinic VO_2 revealed by ultrafast electron diffraction. *Science*, 346, 445–8 (2014).

[122] Ramesh Srinivasan, Jonathan S Feenstra, Sang Tae Park, Shoujun Xu, and Ahmed H Zewail. Dark structures in molecular radiationless transitions determined by ultrafast diffraction. *Science*, 307, 558–63 (2005).

[123] Peter Miles Anson Sherwood. *Vibrational spectroscopy of solids*. Cambridge University Press, 1972.

[124] Markus Schwoerer and Hans Christoph Wolf. *Organic Molecular Solids*. Wiley, 2007.

[125] M. Gühr, M. Bargheer, and N. Schwentner. Generation of Coherent Zone Boundary Phonons by Impulsive Excitation of Molecules. *Physical Review Letters*, 91, 085504 (2003).

[126] Matias Bargheer, Markus Gühr, and Nikolaus Schwentner. Collisions Transfer Coherence. *Israel Journal of Chemistry*, 44, 9–17 (2004).

[127] Julian Hirscht. *Femtosecond electron diffraction: next generation electron sources for atomically resolved dynamics.* Dr., Universität Hamburg, Hamburg, 2015.

[128] Federico Belli, Amir Abdolvand, Wonkeun Chang, John C. Travers, and Philip St.J. Russell. Vacuum-ultraviolet to infrared supercontinuum in hydrogen-filled photonic crystal fiber. *Optica*, 2, 292 (2015).

[129] Stephan Hess, Helge Bürsing, and Peter Vöhringer. Dynamics of fragment recoil in the femtosecond photodissociation of triiodide ions in liquid solution. *The Journal of Chemical Physics*, 111, 5461, 1999.

[130] Dominik Marx and Jürg Hutter. *Ab Initio Molecular Dynamics.* Cambridge University Press, 2009.

[131] Abu Md Asaduzzaman and Georg Schreckenbach. Computational study of the ground state properties of iodine and polyiodide ions. *Theoretical Chemistry Accounts*, 122, 119–125 (2009).

[132] F. H. Herbstein, M. Kaftory, M. Kapon, and W. Saenger. Structures of three crystals containing approximately — linear chains of triiodide ions. *Zeitschrift für Kristallographie - Crystalline Materials*, 154 (1981).

[133] F. Hlawatsch and G.F. Boudreaux-Bartels. Linear and quadratic time-frequency signal representations. *IEEE Signal Processing Magazine*, 9, 21–67 (1992).

[134] S. Mann and S. Haykin. The chirplet transform: physical considerations. *IEEE Transactions on Signal Processing*, 43, 2745–2761, 1995.

Bibliography

[135] Andrea Volpato and Elisabetta Collini. Time-frequency methods for coherent spectroscopy. *Optics Express*, 23, 20040 (2015).

[136] D. Gabor. Theory of communication. Part 1: The analysis of information. *Journal of the Institution of Electrical Engineers - Part III: Radio and Communication Engineering*, 93, 429–441 (1946).

[137] O. Rioul and M. Vetterli. Wavelets and signal processing. *IEEE Signal Processing Magazine*, 8, 14–38 (1991).

[138] Robert X Gao and Ruqiang Yan. *Wavelets: Theory and Applications for Manufacturing*. Springer, 2010.

[139] I. Daubechies. Where do wavelets come from? a personal point of view. *Proceedings of the IEEE*, 84, 510–513 (1996).

[140] Barbara Burke Hubbard. *The World According to Wavelets: The Story of a Mathematical Technique in the Making, Second Edition*. Taylor & Francis, 1998.

[141] P. Goupillaud, A. Grossmann, and J. Morlet. Cycle-octave and related transforms in seismic signal analysis. *Geoexploration*, 23, 85–102 (1984).

[142] A. Grossmann and J. Morlet. Decomposition of Hardy Functions into Square Integrable Wavelets of Constant Shape. *SIAM Journal on Mathematical Analysis*, 15, 723–736 (1984).

[143] Anthony Teolis. *Computational Signal Processing with Wavelets*. Springer, 1998.

[144] Paul S Addison. *The Illustrated Wavelet Transform Handbook: Introductory Theory and Applications in Science, Engineering, Medicine and Finance*. CRC Press, 2002.

[145] Dario Polli, Larry Lüer, and Giulio Cerullo. High-time-resolution pump-probe system with broadband detection for the study of time-domain vibrational dynamics. *The Review of scientific instruments*, 78, 103108 (2007).

[146] John Robert Taylor. *An Introduction to Error Analysis: The Study of Uncertainties in Physical Measurements.* University Science Books, 1997.

[147] John P. Perdew, Kieron Burke, and Matthias Ernzerhof. Generalized Gradient Approximation Made Simple. *Physical Review Letters,* 77, 3865–3868 (1996).

[148] John P. Perdew, Kieron Burke, and Matthias Ernzerhof. Generalized Gradient Approximation Made Simple [Phys. Rev. Lett. 77, 3865 (1996)]. *Physical Review Letters,* 78, 1396–1396 (1997).

[149] Jan M. L. Martin and Andreas Sundermann. Correlation consistent valence basis sets for use with the Stuttgart–Dresden–Bonn relativistic effective core potentials: The atoms Ga–Kr and In–Xe. *The Journal of Chemical Physics,* 114, 3408 (2001).

[150] Walter J. Stevens, Morris Krauss, Harold Basch, and Paul G. Jasien. Relativistic compact effective potentials and efficient, shared-exponent basis sets for the third-, fourth-, and fifth-row atoms. *Canadian Journal of Chemistry,* 70, 612–630 (1992).

[151] Alexandre Tkatchenko and Matthias Scheffler. Accurate Molecular Van Der Waals Interactions from Ground-State Electron Density and Free-Atom Reference Data. *Physical Review Letters,* 102, 073005 (2009).

Thesis-related publications:

Rui Xian, Stuart A. Hayes, Gastón Corthey, David M. Rogers, Carole A. Morrison, Valentyn I. Prokhorenko, C. Lu, R. J. Dwayne Miller, "*Atomistic monitoring of crystalline chemistry using femtosecond electron diffraction*," in preparation.

Rui Xian, Gastón Corthey, David M. Rogers, Carole A. Morrison, Valentyn I. Prokhorenko, Stuart A. Hayes, R. J. Dwayne Miller, "*Coherent ultrafast lattice-directed reaction dynamics*," under review, Nature Chemistry.

Rui Xian, Gastón Corthey, Stuart A. Hayes, Carole A. Morrison, David M. Rogers, Alexander Marx, Valentyn I. Prokhorenko, Cheng Lu, R. J. Dwayne Miller, "*Atomically-resolved structural changes during a solid state geminate recombination reaction*," Ultrafast Phenomena XX, OSA Technical Digest, paper UTh2B.1 (2016).

Rui Xian, Valentyn I. Prokhorenko, Ryan L. Field, R. J. Dwayne Miller, "*Coherent control of the photodissociation of triiodide in solution reveals new pathways*," Ultrafast Phenomena XIX, Springer Proceedings in Physics, Volume 162, 382-385 (2015).

Other publications:

Khalid M. Siddiqui, Gastón Corthey, Stuart A. Hayes, Andreas Rossos, Daniel S. Badali, **Rui Xian**, R. Scott Murphy, Benjamin J. Whitaker and R. J. Dwayne Miller, "*Synchronised photoreversion of spirooxazine ring opening in thin crystals to uncover ultrafast dynamics*," CrystEngComm, 18, 7212-7216 (2016).

Conference presentations:

20th International Conference on Ultrafast Phenomena,
Santa Fe, New Mexico, USA, 07/2016 (oral presentation)

45th IUPAC World Chemistry Congress,
Busan, South Korea, 08/2015 (oral presentation)

FEMTO 12, The Hamburg Conference on Femtochemistry,
Hamburg, Germany, 07/2015 (poster presentation)

19th International Conference on Ultrafast Phenomena,
Okinawa, Japan, 07/2014 (poster presentation)

Eidesstattliche Versicherung

Declaration on oath

Hiermit erkläre ich an Eides statt, dass ich die vorliegende Dissertationsschrift selbst verfasst und keine anderen als die angegebenen Quellen und Hilfsmittel benutzt habe.
I hereby declare, on oath, that I have written the present dissertation by my own and have not used other than the acknowledged resources and aids.

Hamburg, den *city and date*

Unterschrift *signature*